ANALYSIS OF SUPERNOVA SPECTRA

DAVID J. JEFFERY

AND

DAVID BRANCH

Department of Physics and Astronomy

University of Oklahoma

Norman, Oklahoma 73019, U.S.A.

Reference

Jeffery, D. J., & Branch, D. 1990, in *Jerusalem Winter School for Theoretical Physics,* Vol. **6,** *Supernovae,* ed. J.C. Wheeler, T. Piran, and S. Weinberg (Singapore: World Scientific), p. 149.

ANALYSIS OF SUPERNOVA SPECTRA

DAVID J. JEFFERY AND DAVID BRANCH
Department of Physics and Astronomy
University of Oklahoma, Norman, Oklahoma 73019, U.S.A.

ABSTRACT

A simple and fast analysis procedure for supernova spectra is presented. Included in the presentation is an introduction to the Sobolev method of radiative transfer, a description of a simple model of a supernova, a catalogue of line profiles illustrating line formation in the simple supernova model, and an example analysis of the SN 1987A photometry and optical spectra. The SN 1987A analysis is intended as a benchmark to which more advanced and detailed analyses can be compared. Synthetic spectra calculated in the SN 1987A analysis using solar-composition thermodynamic-equilibrium predicted line optical depths are in rough qualitative agreement with the observed spectra; the agreement becomes poorer after day 100 after the explosion. It is probable that for the period from day 16 to about day 100 after the explosion that the SAAO photometric radius is close to being the true photospheric radius: earlier than day 16 the photometric radius is too small.

I. INTRODUCTION

This article presents a simple and fast analysis procedure for supernova spectra. The procedure uses the Sobolev method of radiative transfer and a simple supernova model in order to calculate synthetic spectra. Comparisons and fits of the synthetic spectra to observed spectra allow determinations of supernova parameters. Because of the many simplifying assumptions made in the analysis procedure, the determinations the procedure makes will be mainly qualitative. More exact, but more difficult, determinations require a more advanced procedure (see, e.g., Höflich 1988; Eastman and Kirshner 1989).

In § II of this article, the Sobolev method is presented. The supernova model, here called the ES model, that is used in the analysis procedure is described in § III. In § IV, a catalogue of line profiles that illustrates line formation in the ES model is presented and discussed. As an example of the analysis procedure, an analysis of the photometry and optical spectra of SN 1987A is given in § V. This analysis is also intended to serve as benchmark to which the more advanced and detailed analyses of SN 1987A can be compared. The book *Stellar Atmospheres* (hereafter referred to as SA) by Mihalas (1978) is used throughout this article as a reference for the concepts and equations of radiative transfer and for well-known results of radiative transfer analysis.

II. THE SOBOLEV METHOD

The Sobolev method is an approximate technique that is used to calculate line radiative transfer in atmospheres in which there are macroscopic velocity fields with large velocity gradients. It originated with Sobolev (1947) and has been extended by others (e.g., Castor 1970; Rybicki 1970; Lucy 1971; Rybicki and

Hummer 1978; Olson 1982; Hummer and Rybicki 1985; Puls and Hummer 1988; Jeffery 1988, 1989, 1990; Mazzali 1988, 1989). It has been used to calculate synthetic line spectra for stars with strong winds (e.g., Castor and Nussbaumer 1972) and has also been used in radiation-driven wind calculations (e.g., Pauldrach, Puls, and Kudritzki 1986). For supernova spectrum analyses, the Sobolev method has been used by Branch and collaborators (Branch 1980; Branch et al. 1981, 1982, 1983, 1985). Radiative transfer techniques that are more accurate for moving atmospheres than the Sobolev method are the comoving-frame formalism (SA, p. 490) and Monte-Carlo simulations (see, e.g., Natta and Beckwith 1986). In this section, the basic Sobolev method expressions are derived and the procedure for Sobolev method calculations is outlined. The derivations and notation of this section largely follow those of Rybicki and Hummer (1978).

Consider an atmosphere with a macroscopic velocity field with large velocity gradients. In addition to the macroscopic velocity field, there will be the random thermal motions of atoms and there may be a microturbulent velocity field: i.e., a random motion of fluid elements. It is assumed that the characteristic velocities of the macroscopic velocity field are much larger than the thermal velocities or any microturbulent velocities. For the moment, the only source of opacity that will be considered is the opacity of a single atomic line transition with a line center wavelength of λ_0. The line opacity is described by a line absorption profile $\phi(\lambda)$ that is normalized to 1, that is a maximum at the line center wavelength, and that decays rapidly as wavelength decreases or increases from the line center wavelength. Now consider a specific intensity beam $I(\lambda, \hat{n}, s)$ where $\hat{n}$ points in the propagation direction and s is the beam path coordinate. The component of the macroscopic velocity in the $\hat{n}$ direction on the beam path is $v(s) = \hat{n} \cdot \vec{v}(\vec{r})$. The Doppler shift that the photons experience in a reference frame in which except for random motions the matter is at rest (hereafter called the comoving frame) causes a wavelength shift of the line center wavelength and the line absorption profile in an observer's reference frame. If it is now assumed that the velocity gradient is never zero, then the observer frame line center wavelength will equal the specific intensity beam wavelength only at isolated points. Provided that only the first order Doppler formula is required, these points, called resonance points, can be determined from the equation

$$\lambda_0 = \lambda \left[1 + v(s)/c\right] \ . \tag{1}$$

It is at the resonance points that the beam photons will interact most strongly with the line. However, since the line opacity is distributed over a range of wavelength according to the line absorption profile ϕ, the varying Doppler shift due to the varying macroscopic velocity will bring each part of the profile into resonance with the specific intensity beam at a different spatial point. Thus, there will be a spatial region where the specific intensity beam will interact significantly with the line. Such spatial regions are called resonance regions.

The confinement to resonance regions of the interaction of line transitions and specific intensity beams is a great simplification for a radiative transfer technique. However, even with this simplification, the general problem of radiative transfer in an atmosphere with macroscopic velocity fields is still difficult. The Sobolev method is a technique that exploits the confinement to resonance regions, but in its usual formulation obviates much of the difficulty of the general problem with the following assumptions. (1) The first order Doppler formula is sufficiently accurate. This means that the velocities in the atmosphere must be much less than the speed of light. In most astrophysical atmospheres of interest this condition should be met. (2) The integrated line opacity K, directional velocity derivative $(dv/ds) = \sum_{i,j} n_i n_j \left(\partial v_i / \partial x_j\right)$, and line source function S can be approximated for a whole resonance region by their resonance point values. Since K and, in general, S depend on the occupations numbers (i.e., the populations of atomic levels and ionization stages), the condition on K and S implies that the occupation numbers be approximately constant across the resonance regions. (3) Complete redistribution in wavelength and angle in the comoving frame, hereafter simply referred to as complete redistribution, is a valid approximation for line scattering. This assumption is valid for many but not all atmosphere calculations (see SA, p. 411, and references therein).

Before deriving the Sobolev method, it is useful to give some further information about the line absorption profile ϕ and the integrated line opacity K. The absorption profile that applies in most astrophysical cases is the Voigt profile which has Lorentzian wings due to natural and collisional damping and a Gaussian core due to thermal and, perhaps, microturbulent Doppler line broadening (SA, p. 279). The characteristic width associated with the line profile, called the linewidth, is usually $\sqrt{2}$ times the standard deviation of the Gaussian core. The Gaussian linewidth of convolved thermal and microturbulent Gaussian

distributions is

$$\Delta\lambda = \sqrt{\Delta\lambda_{\rm th}^2 + \Delta\lambda_{\rm turb}^2} \ . \tag{2}$$

The thermal Gaussian linewidth is given by

$$\Delta\lambda_{\rm th} = \frac{\lambda_0}{c}\sqrt{\frac{2kT}{m}} = 0.4286\left(\frac{\lambda_0}{10^4}\right)\sqrt{\frac{T}{10^4 A}} \ , \tag{3}$$

where A is the atomic mass and T is in Kelvins. If the integrated line opacity is very large, the Lorentzian wings of the line may have significant opacity. In such cases, the Gaussian core linewidth cannot be a completely adequate characteristic linewidth. The integrated line opacity is given by

$$K = \left(\frac{\pi e^2}{m_e c}\right) f_0 n_l \left(1 - \frac{g_l n_u}{g_u n_l}\right)\left(\lambda_0^2/c\right) \ , \tag{4}$$

where l designates the lower level of the transition, u the upper level, f_0 is the oscillator strength of the line, n_l and n_u are the occupation numbers of the levels, g_l and g_u are the statistical weights or degeneracies of the levels, and

$$\left(\frac{\pi e^2}{m_e c}\right) = 2.654 \times 10^{-2}\,{\rm cm}^2\,{\rm s}^{-1}.$$

The $\left(\lambda_0^2/c\right)$ factor is needed for the wavelength description form of the integrated line opacity; it is absent in the frequency description form. A derivation of equation (4), without the $\left(\lambda_0^2/c\right)$ factor, is given in SA (p. 79–84). The product of ϕ and K is, of course, the monochromatic line opacity,

$$\kappa(\lambda) = K\phi(\lambda) \ . \tag{5}$$

In order to derive the basic Sobolev method results, consider again the system consisting of a specific intensity beam propagating along a beam path in the $\hat{n}$ direction through an atmosphere that has a macroscopic velocity field and large velocity gradients. Let $s_* = s(\vec{r}\,)$ be a resonance point for wavelength λ_*; from an alternative point of view, λ_* is thought of as the resonance wavelength for point s_*. Using the first order Doppler formula and the assumption that (dv/ds) is constant in the resonance region that centers on s_*, the line absorption profile in the observer frame in the neighborhood of s_* is

$$\phi\left\{\lambda + \lambda_0\left[v_* + (dv/ds)\,(s - s_*)\right]/c\right\} \ , \tag{6}$$

where $v_* = v\,(s_*)$. Note that in writing the argument of equation (6), λ_0 has been used instead of λ as the coefficient of the second term. The consequence of this substitution is that one or more factors of $(1 + v_*/c)$ are neglected in the definitions of τ, β, and J_β introduced below. Given the assumption that the velocities in the atmosphere are much less than the speed of light, the neglect of the $(1 + v_*/c)$ factor is only a small error.

Both the λ and s parameters occur linearly in the argument of equation (6), and thus both the line absorption profile and what can be called the spatial line profile will have the same shape. Moreover, with the assumption that the integrated line opacity is constant across the resonance region, the monochromatic line opacity profile in both wavelength and spatial coordinate spaces will have the same shape. This wavelength-spatial symmetry implies that there is a resonance region width

$$\Delta s = \frac{\Delta\lambda c}{\lambda_0 |(dv/ds)|} = \frac{\Delta v}{|(dv/ds)|} \ , \tag{7}$$

where Δv is the velocity width of the convolved thermal and microturbulent Gaussian velocity distributions. Now Δs is not the actual size of the resonance region. If the optical depth in the spatial line profile Lorentzian wings can be considered negligible, then about 55 % and about 85 % of the total resonance region optical depth (see definition below) are contained in regions centering on the resonance point of sizes Δs and $2\Delta s$, respectively. It is shown below that if the Lorentzian wings are negligible, then it is reasonable to say that

$\sim 2\Delta s$ is the size of the resonance region provided that the resonance region optical depth is less than or of order 10.

The optical depth for wavelength λ_* to a point s in the resonance region is given by

$$t(s) = \int_{-\infty}^{s} ds' \, \kappa(\lambda_*, s') \; , \tag{8}$$

where the lower integration limit has been set to negative infinity since ϕ is negligibly small outside of the resonance region. Since it is assumed that the integrated line opacity can be approximated for the whole resonance region by its resonance point value $K(\vec{r})$, equation (8) can be approximated by

$$t(s) = K(\vec{r}) \int_{-\infty}^{s} ds' \, \phi \left\{ \lambda_* + \lambda_0 \left[v_* + (dv/ds) \left(s' - s_* \right) \right] / c \right\} \; . \tag{9}$$

Defining

$$x(\lambda_*, s - s_*) = \frac{\lambda_* + \lambda_0 \left[v_* + (dv/ds) \left(s - s_* \right) \right] / c}{\Delta\lambda} \; , \tag{10}$$

$$\varphi(x) = \Delta\lambda \phi(x \Delta\lambda) \; , \tag{11}$$

$$H_{\pm}(x) = \pm \int_{\mp\infty}^{x} dx' \, \varphi(x') \; , \tag{12}$$

and

$$\tau = \frac{K(\vec{r}) c}{\lambda_0 |(dv/ds)|} \tag{13}$$

allows equation (9) to be transformed to

$$t(s) = \tau H_{\pm} \left[x \left(\lambda_*, s - s_* \right) \right] \; , \tag{14}$$

where the "+" and "−" cases are for $(dv/ds) > 0$ and $(dv/ds) < 0$, respectively. Note that

$$t(-\infty) = 0 \qquad \text{and} \qquad t(\infty) = \tau \; , \tag{15}$$

and that s values that are outside the resonance region are effectively positive or negative infinity. The τ quantity is the total resonance region optical depth. Note also that

$$\frac{dH_{\pm}}{dx} = \pm \varphi(x) \; . \tag{16}$$

The derivation of the Sobolev method solution begins with the radiative transfer equation for time-independent systems:

$$\frac{dI}{ds} = -\kappa(\lambda, s) \left[I(\lambda, \hat{n}, s) - S(\lambda, \hat{n}, s) \right] \tag{17}$$

(SA, p. 31–32). The atmospheres to which the Sobolev method is applied may not be time-independent. However, it is assumed that the time-dependent term will be negligible. Since equation (17) is a first order linear differential equation, a formal solution can be written immediately with the use of an integrating factor,

$$\exp \left[\int_{-\infty}^{s} ds' \, \kappa(\lambda, s') \right] \; . \tag{18}$$

With the Sobolev method assumptions, the argument of the exponential in equation (18) is just $\tau H_{\pm} \left[x(\lambda, s - s_*) \right]$. Thus, the formal solution to equation (17) for a resonance region centered on s_* is

$$\begin{aligned} I(\lambda, \hat{n}, s) = {} & \exp \left\{ -\tau H_{\pm} \left[x(\lambda, s - s_*) \right] \right\} \\ & \int_{-\infty}^{s} ds' \, \exp \left\{ \tau H_{\pm} \left[x(\lambda, s' - s_*) \right] \right\} \kappa(\lambda, s') S(\lambda, \hat{n}, s') \\ & + \exp \left\{ -\tau H_{\pm} \left[x(\lambda, s - s_*) \right] \right\} I(\lambda, \hat{n}, -\infty) \; . \end{aligned} \tag{19}$$

Making the Sobolev method assumption that $S(\lambda, \hat{n}, s)$ can be approximated by $S(\lambda, \hat{n}, s_*)$ and using the same transformations that led to equation (14) gives

$$\begin{aligned} I(\lambda, \hat{n}, s) &= \exp\left\{-\tau H_{\pm}\left[x(\lambda, s - s_*)\right]\right\} S(\lambda, \hat{n}, s_*) \\ &\qquad \int_{\mp\infty}^{x(\lambda, s-s_*)} dx' \, \exp\left[\tau H_{\pm}(x')\right] \tau \frac{dH_{\pm}}{dx'} \\ &\quad + I(\lambda, \hat{n}, -\infty) \exp\left\{-\tau H_{\pm}\left[x(\lambda, s - s_*)\right]\right\} \\ &= S(\lambda, \hat{n}, s_*) \left[\!\left[1 - \exp\left\{-\tau H_{\pm}\left[x(\lambda, s - s_*)\right]\right\}\right]\!\right] \\ &\quad + I(\lambda, \hat{n}, -\infty) \exp\left\{-\tau H_{\pm}\left[x(\lambda, s - s_*)\right]\right\} \ . \end{aligned} \tag{20}$$

Equation (20) is the formal Sobolev method general expression for radiative transfer through a resonance region centered on s_*. Given the Sobolev method assumptions, equation (20) will in general be most accurate for λ equal to the resonance wavelength λ_* and will in general decrease in accuracy as λ departs from λ_* since this causes the resonance point for λ to move away from s_* where S and τ have been evaluated. However, again given the Sobolev method assumptions, equation (20) will in general have some reasonable accuracy for all wavelengths λ that have resonance points that are inside the resonance region centered on s_*.

In most calculations, the spatial width of the resonance region is considered to be negligible. Therefore, what is needed is the expression for the specific intensity of wavelength λ_* at points well past the resonance point for λ_*: i.e., at points where s is effectively positive infinity. From equation (20) with s set to positive infinity, one obtains

$$I\left(\lambda_*, \hat{n}, \infty\right) = S\left(\lambda_*, \hat{n}, s_*\right)\left[1 - \exp\left(-\tau\right)\right] + I\left(\lambda_*, \hat{n}, -\infty\right) \exp\left(-\tau\right) \ . \tag{21}$$

Equation (21) for the specific intensity emergent from a resonance region is one of the main results of the Sobolev method.

Hitherto, only a single resonance region has been considered. However, if the velocity component along the beam path is nonmonotonic or if there are multiple line transitions, then a specific intensity beam can be in resonance at multiple points. Equation (1) can be used to determine these resonance points. The Sobolev method assumes that the resonance regions are effectively at infinity relative to each other. Thus, the expression for the specific intensity of a beam that has traversed N resonance regions is a simple generalization of equation (21):

$$\begin{aligned} I\left(\lambda_*, \hat{n}, \infty\right) = &\sum_{i=1}^{N} S_i\left(\lambda_*, \hat{n}, s_i\right)\left[1 - \exp\left(-\tau_i\right)\right] \exp\left(-\sum_{j=1}^{i-1} \tau_j\right) \\ &+ I\left(\lambda_*, \hat{n}, -\infty\right) \exp\left(-\sum_{i=1}^{N} \tau_i\right) \ , \end{aligned} \tag{22}$$

where the subscripts i and j, counting in the $-\hat{n}$ direction, number the resonance regions the specific intensity beam has traversed, where each s_i is a resonance point for λ_*, and where the source functions are subscripted since they will in general be due to different line transitions.

Equation (22) can be used to determine the emergent specific intensity of a model atmosphere. However, usually one wants to know the net emergent flux directed toward a distant observer. This is obtained by integrating the observer-directed emergent specific intensity over the projected surface of the atmosphere. It is for this integration that the concept of CD (common-direction) velocity surfaces becomes useful. In an atmosphere with a macroscopic velocity field where the velocity gradient is never zero, the matter with a given velocity component in the observer's direction will lie on geometrical surfaces. It is these surfaces that are called CD velocity surfaces. It is clear that atoms lying on a CD velocity surface will have a common observer frame line center wavelength for a given line transition. Thus, the CD velocity surface is a surface

made up of resonance points for a given line transition, direction, and observer frame wavelength λ. The explicitly three-dimensional form of equation (1),

$$\lambda_0 = \lambda\left[1 + \hat{n}\cdot\vec{v}(\vec{r})/c\right] , \tag{23}$$

can be used to determine the $\hat{n}$-direction CD velocity surfaces for a line transition with line center wavelength λ_0. Exploiting the geometry of the CD velocity surfaces is usually helpful in integrating for the net emergent flux. To carry out the integrations the line source functions must be known. One of the Sobolev method's most useful features is that it provides relatively simple expressions for the line source functions.

A general expression for the line source function (Hummer 1969), adapted to atmospheres with macroscopic velocity fields, is

$$\begin{aligned} S(\vec{r},\lambda,\hat{n}) = {} & \frac{(1-\epsilon)}{\psi\Big\{\lambda + (\lambda_0/c)\left[\hat{n}\cdot\vec{v}(\vec{r})\right]\Big\}} \\ & \oint \frac{d\Omega'}{4\pi}\int_0^\infty d\lambda' R(\lambda,\hat{n};\lambda',\hat{n}')I(\vec{r},\lambda',\hat{n}') \\ & + G(\vec{r}) , \end{aligned} \tag{24}$$

where a different parameterization than that used before has been introduced for the source function and the specific intensity, the ψ-function is the normalized line emission profile in the observer frame, $R(\lambda,\hat{n};\lambda',\hat{n}')$ is the photon redistribution function, $I(\vec{r},\lambda',\hat{n}')$ is the specific intensity beam incident on $\vec{r}$, ϵ is the probability per scattering that a photon leaves the line, and G is the non-scattering source of line photons. The evaluation of ϵ and G in general is a difficult task involving the solution of the rate equations (SA, p. 137 and 374).

The photon redistribution function depends on the nature of the line transition and can be quite complicated (SA, p. 411). However, the Sobolev method assumption of complete redistribution provides a greatly simplified redistribution function: angular complete redistribution means that the scattering is isotropic; wavelength complete redistribution means that the incident and scattered photon wavelengths are uncorrelated. Here, as is usually done, wavelength complete redistribution is also taken to mean that the line emission and absorption profiles are the same function: i.e., $\psi(\lambda) = \phi(\lambda)$. In the observer frame, the assumed redistribution function takes the form

$$R(\lambda,\hat{n};\lambda',\hat{n}') = \phi\Big\{\lambda + (\lambda_0/c)\left[\hat{n}\cdot\vec{v}(\vec{r})\right]\Big\}\phi\Big\{\lambda' + (\lambda_0/c)\left[\hat{n}'\cdot\vec{v}(\vec{r})\right]\Big\} , \tag{25}$$

where the first ϕ-function is exactly the observer frame line emission profile. Substituting the complete redistribution function into equation (24) gives

$$\begin{aligned} S(\vec{r}) = {} & (1-\epsilon)\oint\frac{d\Omega}{4\pi}\int_0^\infty d\lambda\phi\Big\{\lambda + (\lambda_0/c)\left[\hat{n}\cdot\vec{v}(\vec{r})\right]\Big\}I(\vec{r},\lambda,\hat{n}) \\ & + G(\vec{r}) , \end{aligned} \tag{26}$$

where the primes on the dummy variables have been dispensed with. The cancellation of the line emission profile from equation (26) leaves the line source function with no dependence on angle or wavelength. Note that the Sobolev method assumption that S be approximately constant inside resonance regions requires the assumption that ϵ and G are also approximately constant inside resonance regions.

The Sobolev method general expression for the specific intensity given by equation (20) can be substituted into equation (26) to obtain the line source function for a point $\vec{r}$ which is also from the Sobolev method assumptions the approximate line source function for the resonance region centered on $\vec{r}$. The expression for this line source function is

$$\begin{aligned} S(\vec{r}) = {} & (1-\epsilon)\oint\frac{d\Omega}{4\pi}\int_0^\infty d\lambda\phi\Big\{\lambda + (\lambda_0/c)\left[\hat{n}\cdot\vec{v}(\vec{r})\right]\Big\} \\ & \Bigg(S(\vec{r})\Big[\Big[1-\exp\left\{-\tau H_\pm\left[x(\lambda,0)\right]\right\}\Big] \\ & + I_{\rm ext}(\vec{r},\lambda,\hat{n})\exp\left\{-\tau H_\pm\left[x(\lambda,0)\right]\right\}\Bigg) \\ & + G(\vec{r}) , \end{aligned} \tag{27}$$

where the parameterization of the source function and the specific intensity have been changed from equation (20): the source function to $S(\vec{r})$ in order to conform to the complete redistribution assumption and the specific intensity to $I_{\rm ext}(\vec{r},\lambda',\hat{n}',)$ where the subscript "ext" for external is meant to explicitly indicate that this is the specific intensity incident on the resonance region centered on $\vec{r}$ due to sources external to the resonance region. Recall that the general expression for the specific intensity decreases in accuracy as λ departs from the resonance wavelength, but that it is guaranteed by the Sobolev method assumptions to have some reasonable accuracy for all wavelengths λ that have resonance points that are inside the resonance region centered on $\vec{r}$. Since the ϕ-function in the integrand of equation (27) is a decreasing weighting function for the general expression as λ departs from the resonance wavelength and is small for wavelengths λ that have resonance points outside of the resonance region centered on $\vec{r}$, it is clear that equation (27) is an accurate expression given the Sobolev method assumptions. Note that the resonance wavelength for $\vec{r}$ is a function of direction in general.

To obtain the Sobolev method line source function from equation (27), the further assumption is required that the wavelength variation of $I_{\rm ext}(\vec{r},\lambda,\hat{n})$ is negligible across the wavelength region where the ϕ-function is significantly different from zero. This new assumption is not a significant new limitation for the Sobolev method. If $I_{\rm ext}(\vec{r},\lambda,\hat{n})$ arises from line transitions in other resonance regions, then the Sobolev assumption of slow spatial and hence slow wavelength variation of line source functions implies that $I_{\rm ext}(\vec{r},\lambda,\hat{n})$ will be sufficiently slowly varying with wavelength. If $I_{\rm ext}(\vec{r},\lambda,\hat{n})$ originates from a continuum radiation emitting source, then, in general, $I_{\rm ext}(\vec{r},\lambda,\hat{n})$ will again be sufficiently slowly varying with wavelength. It is most accurate to approximate $I_{\rm ext}(\vec{r},\lambda,\hat{n})$ by its value at the wavelength for which the ϕ-function in equation (27) is a maximum: i.e., at the resonance wavelength for point $\vec{r}$ and the $\hat{n}$ direction. Again let λ_* be the resonance wavelength; λ_* can be determined from equation (23). Substituting λ_* for λ gives $I_{\rm ext}(\vec{r},\lambda_*,\hat{n},)$. Note that the assumption about the slow wavelength variation of $I_{\rm ext}(\vec{r},\lambda,\hat{n})$ implies that $I_{\rm ext}(\vec{r},\lambda_*,\hat{n})$ will also vary slowly as a function of $\vec{r}$ across resonance regions: i.e., will vary much more slowly than the spatial variation of ϕ displayed by equation (6).

In order to evaluate the integral in equation (27), replace $I_{\rm ext}(\vec{r},\lambda,\hat{n})$ by $I_{\rm ext}(\vec{r},\lambda_*,\hat{n})$, set the lower integration limit to negative infinity, transform the integration variable from λ to x using equation (10), and make substitutions using equations (11), and (16). The resulting expression is

$$S(\vec{r}) = (1-\epsilon)\left[(1-\beta)S(\vec{r}) + J_\beta\right] + G(\vec{r}) \ , \tag{28}$$

where

$$\beta = \oint \frac{d\Omega}{4\pi}\left(\frac{1-e^{-\tau}}{\tau}\right) \ , \tag{29}$$

and

$$J_\beta = \oint \frac{d\Omega}{4\pi}\left(\frac{1-e^{-\tau}}{\tau}\right) I_{\rm ext}\left(\vec{r},\lambda_*,\hat{n}\right) \ . \tag{30}$$

Note that τ depends on angle due to the factor (dv/ds) in equation (13). The β is called the escape probability since it is the probability that a photon emitted by the line at $\vec{r}$ will escape the resonance region and go to infinity without being scattered again by the line. Equation (28) is immediately solved to give the Sobolev method line source function,

$$S(\vec{r}) = \frac{(1-\epsilon)J_\beta + G(\vec{r})}{\epsilon + (1-\epsilon)\beta} \ . \tag{31}$$

Note that this expression for S has no dependence on $\vec{v}(\vec{r})$ or ϕ, but depends only on the quantities, ϵ, G, K, (dv/ds), and $I_{\rm ext}\left(\vec{r},\lambda_*,\hat{n}\right)$, that have been assumed to be slowly varying across the resonance region. Thus, equation (31) is consistent with the assumption that S is slowly varying across the resonance region.

In general, equation (31) will not be an explicit solution for the line source function $S(\vec{r})$ even if ϵ and G are given. This is because the J_β depends on $I_{\rm ext}\left(\vec{r},\lambda_*,\hat{n},\right)$ which may in turn depend on $S(\vec{r})$ if the velocity field is nonmonotonic in some directions. Rybicki and Hummer (1978) discuss the means of solving for $S(\vec{r})$ in such cases. If the atmosphere is in general expansion or contraction, the $I_{\rm ext}\left(\vec{r},\lambda_*,\hat{n}\right)$ quantities needed to evaluate the line source function for a line transition cannot depend on that line source function. This is easy to understand. In a general expansion (contraction) case, a photon emitted by a line transition that escapes the resonance region of emission will always be progressively redshifted (blueshifted) away from the

comoving-frame line center wavelength of the emitting line transition as it propagates through the atmosphere and will therefore never interact with the emitting line transition again. Therefore, for atmospheres in general expansion or contraction equation (31) will be an explicit solution for the line source function. As shown by Olson (1982), one can build up the line source functions in general expansion (contraction) cases by starting with the bluest (reddest) line transition being considered and then evaluating the line source functions successively in the redward (blueward) direction.

It is in the evaluation of the line source functions that CP (common-point) velocity surfaces are used. For a point $\vec{r}$ and a specified relative velocity, δv, the CP velocity surface is solved for from

$$\delta v = \frac{(\vec{r} - \vec{r}')}{|\vec{r} - \vec{r}'|} \cdot [\vec{v}(\vec{r}) - \vec{v}(\vec{r}')] \ , \tag{32}$$

where $\vec{r}'$ traces out the CP velocity surface. If $\delta v = 0$, then there will be a two-way radiative coupling of the atoms at $\vec{r}$ and on the CP velocity surface by any line transition. This situation, of course, can only arise in atmospheres where the velocity field is nonmonotonic in some directions. Equation (31) will be an implicit solution for the line source functions in such atmospheres. If the wavelength Doppler shift due to δv equals the wavelength separation between two different line transitions, then there will be a one-way radiative coupling between the atoms at $\vec{r}$ and on the CP velocity surface. When $\delta v > 0$ ($\delta v < 0$), then the redder (bluer) line transition will absorb photons at $\vec{r}$ that were emitted on the CP velocity surface by the bluer (redder) line transition. For an atmosphere in general expansion (contraction) the direction of the line transition radiative coupling is, of course, always blue-to-red (red-to-blue). Knowledge of the geometry of the CP velocity surfaces facilitates the integrations needed to evaluate the line source functions.

A system for which there is a simple explicit expression for the line source function consists of a spherical photosphere (see § III for a physical definition of the photosphere) of radius R that produces a wavelength-independent, angle-of-emission-independent specific intensity, $I_{\rm ph}$, and an atmosphere in which the only opacity is due to a single line transition, where τ is direction-independent, and where ϵ and G are zero. For this system, equation (31) becomes

$$S(r) = W(r) I_{\rm ph} \ , \tag{33}$$

where

$$W(r) = \frac{1}{2} \left[1 - \sqrt{1 - (R/r)^2} \ \right] \tag{34}$$

is called the dilution factor. The dilution factor is just the solid angle subtended by the photosphere at radius r divided by 4π. Equation (33) shows that the line source function has a strong radial dependence in this case. Since many astrophysical systems have strong central sources of continuum radiation, the line source functions in these systems will often approximate the behavior of equation (33).

The accuracy of the Sobolev method often depends on how accurate is the assumption that S and K are constant across the resonance region. In assessing the accuracy of this assumption, it is necessary to determine the size of the resonance region. To do this, weak and strong line cases are examined with the assumption that there is negligible optical depth in the Lorentzian wings of the spatial line profile. Consider a specific intensity beam that emerges from a resonance region in the case where there is no incident specific intensity beam in the emergent beam's direction. The exact expression for the emergent specific intensity (SA, p. 38) is

$$I = \int_0^\tau dt \, e^{-t} S(t) \ , \tag{35}$$

where S is expressed as a function of the optical depth t and t increases backward along the beam path (i.e., in the direction opposite to the photon flow). For a weak line, one has $\tau << 1$. Therefore, e^{-t} can be approximated by 1, and

$$I \approx \int_0^\tau dt \, S(t) \ . \tag{36}$$

Now of order 85 % of the optical depth of the resonance region will correspond to the spatial region of $2\Delta s$ centered on the resonance point. If S and K are approximately constant or have a not too strong linear dependence on s across distances of $2\Delta s$ or larger, equation (36) can be approximated by

$$I = \tau S(t_*) \ , \tag{37}$$

where t_* is the optical depth to the resonance point. Equation (37) is exactly the Sobolev method result for a weak line (see eq. [21]). Clearly, for the weak line case, the Sobolev method approximation of using the resonance point value of S will to be tend to be valid even if S and K vary linearly with s over distances of order $2\Delta s$.

In the weak line case, as can be seen from equation (36), all source function contributions to the emergent specific intensity are weighted equally per interval dt. However, when τ is significant, it is clear that the exponential factor in equation (35) is a monotonically decreasing weighting factor with optical depth. Physically, this simply means that the greater the optical depth of flux emission, the greater is the absorption of that flux in traversing the resonance region. Thus, there is a strong tendency for the emergent specific intensity to be determined by the source function at the smaller optical depths. To understand the limiting behavior as τ becomes much greater than 1 (i.e., the strong line case), let the approximations

$$S(t) = S_1 + \Delta S_1(t-1) \qquad \text{and} \qquad \tau = \infty \tag{38}$$

be made. Equation (35) can now be evaluated to give

$$I = S_1 = S\left[t(s) = 1\right] , \tag{39}$$

where s, in contrast to the earlier usage, is now thought of as increasing backward along the beam path. Equation (39) is a very crude result since in general S will not vary linearly with t over a significant fraction of the resonance region. However, since S will often vary more slowly than an exponential of t, the result shows that for strong lines there is a tendency for the emergent specific intensity to be equal to the line source function at of order optical depth 1. The Sobolev method result for a strong line has $I = S\left(t_*\right)$. If S is not sufficiently constant over the distances of order $|s(t=1) - s\left(t_*\right)|$, then the Sobolev method will tend to give results that are systematically in error for all but weak lines.

To find out roughly over how large a spatial region S must be constant for the Sobolev method to be adequate for strong lines, one can solve $\tau\left(s_1\right) = 1$ for s_1. An analytic solution is not possible. However, if λ_0 is replaced by the more correct λ in equation (9) and it is assumed that K is sufficiently constant, then it is easy to show that

$$|s_1/\Delta s| \approx \sqrt{\ln(\tau) - \ln\left(2\sqrt{\pi}\right)} \qquad \text{for} \qquad \tau > 10 , \tag{40a}$$

where

$$|s_1/\Delta s| \approx 1 \qquad \text{for} \qquad \tau = 10 . \tag{40b}$$

From the investigation of the weak and strong line cases, it is reasonable to say for $\tau < 10$ that the resonance region size is of order $2\Delta s$ and for $\tau > 10$ that the resonance region size is of order $2|s_1|$. These size estimates are probably not valid if there is nonnegligible optical depth in the Lorentzian wings of the spatial line profile. The Lorentzian profile decays much more slowly than the Gaussian profile with distance from the resonance point. The variation of $|s_1/\Delta s|$ with τ tends to be linear if τ is large enough that s_1 corresponds to a point in the Lorentzian wing. Clearly, with nonnegligible optical depths in the wings, the resonance region can become very much broader than $2\Delta s$. Usually, the Lorentzian wings will become important only for extremely strong lines. For a further discussion of line profiles see SA (p. 273).

Since $|s_1/\Delta s|$ when greater than 1 grows approximately only as the square root of the logarithm of τ provided the Lorentzian wings are negligible, the Sobolev method's accuracy for a given atmosphere for all but extremely strong lines can be roughly measured by the parameter

$$\mathcal{R} = \langle \Delta s \rangle / s_{\text{ch}} , \tag{41}$$

where $\langle \Delta s \rangle$ is some sort of average of Δs over a whole atmosphere and s_{ch} is a characteristic distance over which K and S vary significantly. Since $\mathcal{R}$ is only a rough measure of accuracy, an equally valid definition of $\mathcal{R}$ is

$$\mathcal{R} = \langle \Delta v \rangle / v_{\text{ch}} , \tag{42}$$

where v_{ch} is a characteristic macroscopic velocity and where equation (7) can be used to relate equation (42) to equation (41). This definition of $\mathcal{R}$ is often more convenient since random velocity distribution velocity

width is a more commonly thought of parameter than Δs and since characteristic macroscopic velocities can usually be estimated more directly from observational data than characteristic distances.

The appropriate choice of the s_{ch} or v_{ch} parameter is a matter of judgement. Since K and S depend strongly on occupation numbers, either the density scale height or the temperature scale height may be an appropriate choice for s_{ch}. As can be seen from equations (33) and (34), the scale of variation of S will often tend to be set by the radius of a continuum radiation producing photosphere. For supernovae, as is discussed in § III, the photospheric velocity (i.e., the velocity of matter at the photosphere) can be estimated from a study of the emergent line spectrum and the photospheric velocity is directly proportional to the photospheric radius. Thus, for supernovae the photospheric velocity may often be an appropriate choice for v_{ch}. For stars with winds, v_{ch} can be chosen to be the final velocity the escaping wind matter reaches as it flows away from the star.

Since $\mathcal{R}$ is only crudely defined, no exact calibration of $\mathcal{R}$ with accuracy is possible. Nevertheless, $\mathcal{R}$ is useful in judging the applicability of the Sobolev method. Hamann (1981) has done a study which compares Sobolev method results for varied $\mathcal{R}$ to more accurate comoving-frame formalism results for lines with complete redistribution and Gaussian absorption and emission profiles. The Sobolev method results for $\mathcal{R} = 0.1$, which was the smallest $\mathcal{R}$ value studied, were qualitatively in agreement with the comoving-frame formalism results. However, there were systematic differences due primarily to the radial variation of the line source functions. It should be noted that Hamann's conclusion that the Sobolev method's treatment of radiatively coupled lines is less accurate than its treatment of isolated lines is obsolete. Hamann used an older, less accurate prescription for Sobolev method line radiative coupling than the prescription introduced by Olson (1982). Olson reports that with his prescription Sobolev method calculations with radiatively coupled lines are as accurate as Sobolev method calculations with isolated lines.

An estimate of $\mathcal{R}$ for supernovae can be made. Characteristic velocities for supernova ejecta have been found to be $11000\,\mathrm{km\,s^{-1}}$ for SNe I (Branch 1977) and $7000\,\mathrm{km\,s^{-1}}$ for SNe II (Patchett and Branch 1972). Note that these characteristic supernova velocities satisfy the condition that velocities be much less than the speed of light that is required by the usual formulation of the Sobolev method. Both SNe I and SNe II have estimated atmospheric temperatures of order $10^4\,\mathrm{K}$ (Branch et al. 1983; Wagoner 1982). Thus, the thermal velocities of atoms in supernova atmospheres will be of order $10\,\mathrm{km\,s^{-1}}$ or smaller. Accepting these velocity estimates, one obtains at most

$$\mathcal{R} \sim 10^{-3} \,. \tag{43}$$

If microturbulent velocites of order $100\,\mathrm{km\,s^{-1}}$ occur in supernova ejecta, $\mathcal{R}$ would be of order 10^{-2}. These estimates for $\mathcal{R}$ are much smaller than the $\mathcal{R}$ values for which Hamann (1981) found that the Sobolev method was systematically in error. Hamann's figures strongly suggest that the difference between Sobolev method and comoving-frame formalism calculated line spectra will be either much less than 10% of the continuum flux level in the vertical direction and/or much less than $0.1\lambda_0(\Delta v/c)$ in the horizontal direction for $\mathcal{R} \lesssim 10^{-2}$. Such a difference will usually be considered insignificant. Therefore, supernovae are expected to be excellent systems for the application of the Sobolev method except perhaps for cases where there are lines with significant Lorentzian wings.

III. THE ELEMENTARY SUPERNOVA MODEL

The calculation of synthetic supernova spectra requires the application of a radiative transfer technique to a model supernova. In this section, what shall be called the elementary supernova model (hereafter usually the ES model) is introduced and its features and limitations are discussed. The line profiles and synthetic spectra discussed in §§ IV and V were all calculated with versions of the ES model.

The most well-founded feature of the ES model is uniform motion homologous expansion. In homologous expansion, the velocity between any two matter elements is proportional to the distance between the elements. The expanding universe models are well-known examples of homologous expansion without uniform motion. In the case of supernovae, uniform motion is established after very early times (minutes or hours, depending on the radius of the progenitor) because the forces between the matter elements become negligibly small except in the deep interior of the ejecta. Since supernova velocities are of order $10^9\,\mathrm{cm\,s^{-1}}$ and initial supernova radii are at most of order $10^{14}\,\mathrm{cm}$, it is clear, except for exceptional cases, that the initial radial positions of mass elements will be insignificant at observable epochs which are usually at least several days

after the explosion. Thus, the radial position of a mass element that has radial velocity v is approximated to a high accuracy by

$$r = vt \ , \tag{44}$$

where t is the time since the explosion. Note that equation (44) implies that radius and matter velocity will be equivalent coordinates for a given time. From equation (44), it follows that the velocity between any two matter elements separated by a distance s will be given by

$$v(s) = s/t \tag{45}$$

which is the required condition for homologous expansion. In all but very exceptional cases, the early nonhomologous epochs of supernovae will be unobservable, and therefore not amenable to analysis. The only exceptional case so far is SN 1987A. The first optical observations for SN 1987A were made at ~ 6500 s (Jones 1987), 11000 s (McNaught 1987a, 1987b), and 26000 s (Zoltowski 1987) after the explosion. Understanding SN 1987A's radiative transfer behavior at such early epochs requires time-dependent radiative transfer calculations and a full dynamical treatment of the matter flow (Harkness and Wheeler 1989).

In the deep interior of the ejecta, uniform motion homologous expansion probably does not obtain during the first 200 days or so after the explosion. The reason for this is that radioactive reheating of the deep ejecta may cause an acceleration of the overlying mass (Woosley 1988; see also § V*a*). By the time the photosphere (see definition below) of a supernova has receded into the deeper ejecta this acceleration epoch may be largely over and so uniform motion homologous expansion may have have been established. Even if significant acceleration is still occurring when the photosphere is in the deeper ejecta, uniform motion homologous expansion would be a useful simplifying assumption since the radioactive acceleration probably leads to turbulent motions that would be difficult to account for in the ES model.

Equation (45) implies that the directional velocity derivative for all points and directions in the supernova ejecta is given by

$$(dv/ds) = t^{-1} \ . \tag{46}$$

Equations (45) and (46) allow great simplification in the radiative transfer calculation. Equation (45) implies that the CD and CP velocity surfaces (see § II) for supernovae are just planes and spheres, respectively. Equation (46) implies that the Sobolev resonance region optical depths are direction-independent, and thus equation (29) for the escape probability simplifies to

$$\beta = \frac{1 - e^{-\tau}}{\tau} \ . \tag{47}$$

All these simplifying features of uniform motion homologous expansion are included in the ES model.

It has long been considered that supernovae are adequately described as spherically symmetric events, and thus the spherically symmetric ES models are usually employed. However, there are theoretical studies (e.g., LeBlanc and Wilson 1970; Chevalier and Klein 1978; Bodenheimer and Woosley 1983; Symbalisty 1984, 1985; Chevalier and Soker 1989) and observations (McCall et al. 1984; McCall 1985; Schwarz and Mundt 1987; Schwarz 1987; Jeffery 1987; Cropper et al. 1988; Bailey 1988; Méndez et al. 1988; Karovska et al. 1988, 1989) that suggest that some supernovae exhibit significant asymmetries. Thus, aspherical versions of the ES model have been considered (Jeffery 1987, 1988, 1989). In § IV, a calculation with an oblate axisymmetric ellipsoidal ES model is discussed.

The ES model consists of two main components: a photosphere that produces a continuum radiation field and a surrounding outer atmosphere in which line formation occurs. The only energy source for the outer atmosphere is the photospheric continuum radiation field. Now a real photosphere, which the model photosphere is intended to represent, is the atmosphere layer where the emergent line profiles start to form. This real photosphere is located at continuum optical depth of order 1 into a supernova (see, e.g., Eastman and Kirshner 1989). The photosphere can be defined to be the atmosphere layer at a specific optical depth, but since line profile formation probably starts to occur over some range for lines of different strength such a precise definition is a convenience. The continuum optical depth value often used in photosphere definitions is 2/3. The 2/3 value is the optical depth to the layer where the local atmosphere temperature equals the effective temperature in the LTE (local thermodynamic equilibrium) Eddington approximation

plane-parallel grey atmosphere (SA, p. 61). The effective temperature $T_{\rm eff}$ for a plane-parallel atmosphere is the temperature that satisfies

$$F_{\rm emergent} = \sigma_S T_{\rm eff}^4 \ , \tag{48}$$

where $F_{\rm emergent}$ is the emergent flux from the atmosphere and $\sigma_S = 5.670 \times 10^{-5}\,{\rm erg\,s^{-1}\,cm^{-2}\,K^{-4}}$ is the Stefan-Boltzmann constant. By an LTE atmosphere, one means in this context an atmosphere where the mean specific intensity (i.e., angle-averaged specific intensity) at any point equals the Planck function evaluated at the local matter temperature; of course, the specific intensity itself has an angular variation which becomes large near the atmosphere surface. The exact significance that the 2/3 value has in a special case makes it a meaningful choice for the photosphere definition. Note also that a photon emitted in the outward direction from layer at continuum optical depth 2/3 has a probability of $\exp(-2/3) \approx 0.5$ of escaping the atmosphere if line opacities are neglected. Ordinarily, no continuous opacity is included in the ES model. Continuous opacity can be included in an *ad hoc* manner using a discretized continuous opacity approximation (Jeffery 1989).

Since a photosphere is assumed to exist and to be the source of all the outer atmosphere energy, the ES model, at least as formulated in this article, is suited for analyzing supernova spectra from earlier times. A supernova photosphere recedes into the ejecta with time and so eventually there will be radioactive decay energy deposited above the photosphere (see § V); later still the photosphere will vanish altogether when the continuum optical depth to the center of the ejecta has fallen to of order 1. The epoch when a photosphere is the source for all significant energy in the outer atmosphere can be called the photospheric phase. The postphotospheric phase is called the nebular phase. The ES model can probably be modified to treat the nebular phase.

The photosphere is not the atmosphere layer where the coupling of radiation and matter is strong enough to establish TE (i.e., thermodynamic equilibrium). The layer where TE is established is usually deeper and is called the thermalization layer. From analytical considerations, the thermalization layer is found to be located at a continuum optical depth of order $1/\sqrt{3\zeta}$, where ζ is the ratio of absorption opacity to the sum of absorption and scattering opacities (SA, p. 149). Absorption opacity destroys photons and converts their energy into internal energy of matter at the point of interaction; scattering opacity merely redirects photons without substantially altering their energy. The line opacity of atoms and ions in non-TE states can be either absorption or scattering opacity, or can have some complex redistribution behavior. Electron opacity is always scattering opacity. In supernova atmospheres scattering opacity is thought to be dominant (i.e., is thought to be much larger than absorption opacity) and thus ζ is small and the optical depth to the thermalization layer is large (Wagoner 1981; Höflich 1988; Eastman and Kirshner 1989). Note that if absorption opacity is dominant, then the continuum optical depth to the thermalization layer is of order $1/\sqrt{3} \approx 2/3$ and thus the thermalization layer and photosphere are roughly coincident. An atmosphere where absorption opacity is dominant is approximately an LTE atmosphere.

Since in customary usage the ES model does not include continuous opacity above the photosphere or treat radiative transfer beneath the photosphere, true continuum formation is not treated and consequently the absolute sizes of line optical depths obtained from fits of synthetic to observed spectra will be somewhat uncertain. Numerical experiments suggest that such fitted optical depths may be underestimates by a factor of order half an order of magnitude. However, the relative sizes of the fitted optical depths should be more accurate. Moreover, line identifications can be made with considerable certainty just by the observation of similarities in line features between the synthetic and observed spectra. An additional limitation of not having continuous opacity above the photosphere is that the relative sizes of the flux emergent from the atmosphere and the outward-going and inward-going photospheric fluxes will not be accurate. Because it scatters photons back to the photosphere, continuous opacity above the photosphere would make the emergent flux smaller and the inward-going photospheric flux larger relative to the outward-going photospheric flux.

The continuum radiation field that emerges from the ES model photosphere is usually chosen to be a blackbody distribution at a temperature obtained by fitting a blackbody function to the observed continuum spectrum of a supernova; the fitted temperature is called a color temperature. Since the photosphere is moving, the emergent continuum radiation is given a Doppler shift in the observer frame that depends on the angle of emission. It is usually found that is is not possible to fit an entire observed spectrum with a single blackbody function (e.g., Panagia 1985). This clearly results from the fact that in real supernovae the continuum radiation field is formed differently in different wavelength bands. However, usually a single temperature blackbody photospheric radiation field has been adequate for the purposes of

ES model calculations for the optical. Since true continuum formation is not included in the ES model, more elaborate prescriptions would probably be cosmetic.

The physical significance of the color temperature is not clear-cut. If the atmospheric continuous opacity above the thermalization layer were pure scattering wavelength-independent opacity, then the color temperature would be approximately the thermalization layer temperature. However, the thermalization layer temperature would not be the thermalization layer effective temperature. For a spherically-symmetric atmosphere, the effective temperature for a given radius r satisfies

$$L = 4\pi r^2 \sigma_S T_{\rm eff}^4 \ , \tag{49}$$

where L is the total luminosity. The reason that the thermalization layer temperature and effective temperature would not be the same is that the scattering opacity in the atmosphere would scatter some of the photons coming from the thermalization layer back to the thermalization layer where they would be absorbed and would help to establish the thermal state. The backscattering causes the flux emergent from the thermalization layer to be reduced below what a bare spherical blackbody radiator with the thermalization layer radius and temperature would produce. Thus, the thermalization layer effective temperature would fall below the thermalization layer temperature. The larger the optical depth of the scattering atmosphere, the more photons would be backscattered; in the limit of an infinitely thick scattering atmosphere there would be no flux emergent from the atmosphere. The color and thermalization layer temperatures tend to be equal because wavelength-independent scattering opacity does not redistribute flux in wavelength in the comoving frame. The color temperature cannot be exactly the thermalization layer temperature because, among other things, the thermalization layer physical depth and therefore temperature varies in general with wavelength, some flux emergent from the thermalization layer originates from below the thermalization layer where temperatures are different from the thermalization layer temperature, and macroscopic velocity fields in the atmosphere will cause some wavelength redistribution of flux in the observer frame during scattering. If the scattering opacity is wavelength-dependent, then a greater difference between thermalization layer and color temperatures is to be expected. In supernova atmospheres an important source of opacity is the wavelength-independent electron scattering opacity. Thus, some wavelength-independent flux reduction effect is to be expected. This flux reduction effect for supernovae has been investigated by Wagoner (1981).

The flux reduction effect, however, is not the only process determining the emergent supernova flux. There will be some absorption opacity and some thermal emission in the atmosphere. Therefore, since the atmosphere is expected from, e.g., grey atmosphere results (SA, p. 246) to have an outwardly decreasing temperature, the emergent flux will be a convolution of radiation fields at different temperatures. The result is that the color temperature will be lower than the thermalization layer temperature. This atmospheric emission effect becomes greater the greater the atmospheric extension. Atmospheric extension measures how the opacity responsible for the optical depth to the thermalization layer is distributed. The more of this opacity that is distributed to radii large compared to the thermalization layer radius, the greater the atmospheric extension. The greater the atmospheric extension, the more the spherical geometry of the system is important for radiative transfer in the atmosphere. To understand the increase of the atmospheric emission effect with atmospheric extension note that the effective emitting surface for emergent flux occurs at of order optical depth 1 (SA, p. 39) into the atmosphere along the line of sight. This surface is closest to the thermalization layer and is roughly coincident with the photosphere at an impact parameter of zero. As the effective emitting surface impact parameter increases from zero, the surface moves farther from the thermalization layer. The effective emitting surface can depart quite far from the thermalization layer in the limbs of the atmosphere: i.e., at impact parameters greater than the photospheric radius. The greater the variation in the radial distance between the effective emitting surface and the thermalization layer, the greater the mixture of radiation fields with temperatures lower than the thermalization layer temperature in the emergent flux. In spherically-symmetric LTE grey atmosphere calculations (Branch 1979), it has been shown that the atmospheric emission effect can lead to the color temperature being lower than the thermalization layer effective temperature. Since the atmosphere considered was an LTE atmosphere, the thermalization layer and photosphere were roughly coincident and therefore the effective temperatures for thermalization layer and photosphere were roughly the same.

In supernovae, both the flux reduction effect and the atmospheric emission effect will be occurring, and so it is not clear *a priori* which will dominate. Thus, the color temperature could be higher (flux reduction dominates) or lower (atmospheric emission dominates) than the thermalization layer effective temperature.

The color temperature may even be low enough that it could equal or be lower than the photospheric effective temperature; the photospheric effective temperature is, of course, lower than the thermalization effective temperature when, as usual, the photospheric radius is larger than the thermalization layer radius (see eq. [49]).

The radial velocity of matter at the photosphere, hereafter called the photospheric velocity, is a free parameter of the ES model. Using the condition of uniform motion homologous expansion, one finds that the directional velocity derivative for the entire atmosphere is given by

$$(dv/ds) = \left(v_{\rm ph}/R\right) \ , \tag{50}$$

where $v_{\rm ph}$ is the photospheric velocity and R is the photospheric radius. From equations (45), (46), and (50), one can see that specifying the photospheric velocity determines the entire velocity field. An actual physical size scale is not needed for synthetic spectrum calculations. However, for numerical calculations R can be chosen to have some convenient value: e.g., $R = 1$. The photospheric velocity sets the width of the P Cygni line profiles (see § IV) that appear in the synthetic spectra. From fits of synthetic spectra to observed line features and, in particular, to the observed P Cygni line profile troughs, a value for the photospheric velocity can be obtained. Experience in fitting to optical supernova spectra (Branch 1980; Branch et al. 1981, 1982, 1983, 1985) shows that a single value of the photospheric velocity for all optical lines is a reasonable approximation. The fitted photospheric velocities can be used to help estimate the kinetic energy of supernova ejecta. Comparisons of photospheric velocities for different supernovae can be used to detect similar or distinctly different supernova behaviors (see e.g., Branch 1987a). With further assumptions, the time evolution of photospheric velocity can be used in determinations of the Hubble constant (e.g., Branch and Patchett 1973; Kirshner and Kwan 1974; Branch 1987b).

Density profiles (i.e., density distributions as functions of radius, velocity, or mass coordinate) that result from explosion calculations can easily be implemented in the ES model and this has been done (see, e.g., Branch et al. 1985). However, considering the uncertainties in the explosion models and the fact that they are calculated only for particular cases, it is often preferable to have a simple analytic function for the density profile. Colgate and McKee (1969) give an analytic expression for the velocity produced by a shock wave in the outer layers of an exploded near-Chandrasekhar-mass white dwarf:

$$v(r) \propto M(r)^{(-1/4)} \ , \tag{51}$$

where $M(r)$ is the ejecta mass above radius r. An exploded white dwarf that is near the Chandrasekhar mass is a model for SNe Ia. If it is assumed that

$$\rho(r) \propto r^{-n} \ , \tag{52}$$

then equations (51) and (52) imply

$$M(r) \propto r^{-n+3} \ , \tag{53}$$

and

$$v(r) \propto r^{(n-3)/4} \ . \tag{54}$$

Consistency with equation (44) requires that $n = 7$. Thus, an inverse power-law density profile with index 7 is a plausible analytic approximation for SN Ia density profiles. More modern detailed explosion calculations give more complicated density profiles; however, the inverse power-law density profile with index 7 still seems to be a useful rough characteristic density profile for SNe Ia (see, e.g., Branch et al. 1985). For SNe II, the outer ejecta is probably not really describable by a single inverse power-law density profile: see, e.g., Woosley's model 10H density profile (1988) reproduced here in Figure 18b. However, the inverse power-law density profile can still be used as an approximation for limited ranges of supernova ejecta velocity. Since SNe Ib events are not yet well understood, the inverse power-law density profile seems a reasonable assumption for analysis of their spectra. For the ES model, an inverse power-law density profile with $n = 7$ has been the usual choice for the outer ejecta; less steep inverse power laws can be used for calculations of line formation from deeper layers of a supernova. For numerical calculations an outer cutoff radius needs to be assumed. The cutoff radius is usually set sufficiently large that it has no effect on line formation; a cutoff radius that does effect the line formation can be used if desired for some reason.

It is also possible, with simplifying assumptions, to construct an empirical density profile for an observed supernova. For matter in uniform motion homologous expansion, the density profile as a function of radial velocity is given by

$$\rho(v,t) = \rho_0(v)\,(t_0/t)^3 \ , \tag{55}$$

where t_0 is some characteristic time in the uniform motion homologous expansion epoch and $\rho_0(v)$ is the density profile at that time. Now the greatly simplifying assumption is made that the continuous opacity is given by

$$\kappa_{\rm con}(v,t) = \chi\rho(v,t) \ , \tag{56}$$

where χ, the opacity per unit density, is a constant. Using equations (55) and (56), the expression for the continuum optical depth to the photosphere is

$$\tau_{\rm con} = t\,(t_0/t)^3\,\chi \int_{R/t}^{\infty} dv\,\rho_0(v) \ . \tag{57}$$

where R/t is, of course, the photospheric velocity. Assuming $\tau_{\rm con}$ is a constant, which is roughly valid since $\tau_{\rm con}$ is always of order 1, and differentiating and re-arranging equation (57), the photospheric density is found be

$$\rho(R/t,t) = \frac{-2\tau_{\rm con}}{\chi\left[\dfrac{\partial(R/t)}{\partial t}\right] t^2} \ . \tag{58}$$

With the assumptions made, equation (58) can be used to obtain the time evolution of the photospheric density and thus an empirical density profile (i.e., $\rho_0[v]$) from the evolution of the photospheric radius. The photospheric radii are obtained from photospheric velocity values and estimates of the time since the explosion of the supernova. Noise in the photospheric radius values will often lead to a great amount of noise in density values obtained from equation (58) due to the necessity of evaluating the derivative numerically. Therefore, it will usually be better to make the further assumption that

$$R(t) \propto t^m \ . \tag{59}$$

From equations (58) and (59), it follows that

$$\rho[R(t)] = \frac{\tau_{\rm con}(n-1)}{\chi R} \tag{60}$$

and that

$$\rho_0(v) \propto v^{-n} \ , \tag{61}$$

where

$$n = \frac{m-3}{m-1} \ . \tag{62}$$

A fit of equation (59) to the photospheric radii immediately gives a relative empirical density profile by providing a value for n. Since a relative density profile is needed for synthetic spectrum fitting (see below), a value for n is in itself useful information. Clearly, it may not be possible to fit all the photospheric radius data for a supernova with a single power law of time. However, piecewise fitting of equation (59) for intervals of the supernova evolution can be done. Equations (60), (61), and (62) remain valid for piecewise fitting. In § V*a* a piecewise fitting procedure is done for SN 1987A data.

To obtain density values from equation (60), values for χ are needed as well as R and n values; $\tau_{\rm con}$, of course, can be assumed to be 1 or 2/3. Without detailed calculations for χ, only crude estimates of its value are possible. The most important contributions to the continuous opacity are probably electron scattering opacity and the quasi-continuous opacity of hundreds of thousands of weak overlapping lines. The latter opacity is called expansion opacity for brevity. The electron opacity per unit density is given by

$$\chi_e = \frac{0.4006}{\mu_e}\ {\rm cm^2\,g^{-1}} \ , \tag{63}$$

where μ_e is the mean atomic mass per electron (see, e.g., Clayton 1983, p. 84). It may be possible to estimate μ_e from an assumed composition, the color temperature, an estimate of the electron density (see below), and the assumption of TE. The expansion opacity, as has been shown by Karp et al. (1977), can be of the same order as or even larger than the electron opacity. The weak lines causing the expansion opacity are weak in the sense that they leave no obvious signature in a supernova spectrum. In a static atmosphere many of these lines could be saturated. The velocity gradient in a supernova atmosphere spreads the line opacity of the saturated lines over a wavelength band due to the continuously varying Doppler shift; this spreading of opacity in wavelength tends to desaturate these lines, and thus increases the effective opacity that they contribute. The contribution of the expansion opacity to χ can be roughly estimated from the tables in the paper of Karp et al. Given all the assumptions made in deriving equation (60), it is probably reasonable to neglect the expansion opacity and estimate density just from electron density as discussed below. Another procedure for obtaining densities is to use a global criterion to estimate a global average value for χ; this procedure is followed in § V*a*.

If it is assumed that χ_e is also a constant, then it immediately follows from equations (58) and (60) that the photospheric electron density is given by

$$n_e = \frac{-2\tau_e}{\sigma_e \left[\dfrac{\partial(R/t)}{\partial t}\right] t^2} \qquad \text{or} \qquad n_e = \frac{\tau_e (n-1)}{\sigma_e R} \ , \tag{64}$$

where τ_e is the photospheric electron opacity optical depth and

$$\sigma_e = 0.665 \times 10^{-24} \ \text{cm}^2 \tag{65}$$

is the Thomson cross-section. Since expansion opacity makes a significant contribution to the photospheric continuum optical depth, τ_e is actually somewhat smaller than τ_{con}. However, since τ_e will usually be of the same order as τ_{con}, it is probably best to set τ_e to 1 or 2/3. Given all the uncertainties due to the simplifying assumptions, rough estimates for τ_e are satisfactory. Approximate photospheric matter densities can be obtained using the approximate photospheric electron densities given by equation (64), an assumed composition, the color temperature, and the assumption of TE.

The treatment of the line opacity in the ES model is quite simple. The relative values of the Sobolev optical depths for a given ion are fixed by assuming TE and using the Boltzmann law. Thus, using equations (4) and (13), the relative optical depths of two lines designated by i and j are given by

$$(\tau_j/\tau_i) = \exp\left[-(E_j - E_i)\Big/kT\right] \left\{ \frac{(gf)_j \, \lambda_j \left[1 - \exp\left(-hc/kT\lambda_j\right)\right]}{(gf)_i \, \lambda_i \left[1 - \exp\left(-hc/kT\lambda_i\right)\right]} \right\} \ , \tag{66}$$

where

$$(gf)_i = g_i f_i \qquad \text{and} \qquad (gf)_j = g_j f_j \ . \tag{67}$$

The gf values are the often tabulated weighted oscillator strengths. The quantity $\exp(-hc/kT\lambda)$ is the TE correction for stimulated emission. The argument

$$\frac{hc}{kT\lambda} = \frac{1.439}{T_4 \lambda_\mu} \ , \tag{68}$$

where T_4 is temperature in units of 10^4 K and λ_μ is wavelength in microns. For the optical and shorter wavelength ranges, the TE correction for stimulated emission will be small when $T_4 \lesssim 1$. The excitation temperature used in equation (66) is usually chosen to be the color temperature. If the color temperature TE occupation numbers seem inadequate for fitting synthetic spectra, one can always use a free-parameter excitation temperature.

The line optical depths above the photosphere are usually determined simply by scaling the photospheric optical depths with the assumed radial density variation of the ES model. Thus, the effects of variation in abundances, ionization, and excitation are being ignored. Attempting to determine abundance variation

from an empirical analysis with the ES model is probably too difficult except in cases where composition stratification is obvious from the observed line profiles. However, if an abundance distribution is supplied (e.g., the abundance distribution given by an explosion calculation), then this distribution can easily be incorporated in an ES model calculation (see below).

The neglect of ionization variation in the atmosphere is a consequence of ignorance. In LTE, a decreasing temperature at a constant density would lead to decreasing ionization; however, decreasing density tends to increase ionization. In a supernova atmosphere, one expects both the density and, as discussed above, the temperature to decrease with radius. Thus, *a priori* it is not clear even in an LTE picture, how ionization will vary with radius. Moreover, due to low density and the nonisotropic radiation field, the occupation numbers in the atmosphere must depart from the LTE values at some point above the thermalization layer. Note by LTE occupation numbers, one means those occupation numbers calculated using the Saha equation (SA, p. 113), and local electron density, electron temperature, and sometimes local ion density. In this situation, one needs detailed NLTE (non-[local thermodynamic equilibrium]) calculations to determine the occupation numbers. The ES model's assumption of constant ionization avoids the difficulties and, of course, the insights of LTE or NLTE calculations. In practice, the constant ionization assumption has not led to any obvious overwhelming deficiencies in fitting synthetic to observed spectra; deficiencies, of course, could well be masked by the very parameterized nature of ES model calculations. If ionization stage occupation numbers are needed for an ES model calculation, they can be obtained from a TE calculation with an assumed composition and using the color temperature and an estimated photospheric electron density calculated as described above.

The occupation numbers of nonmetastable excited atomic levels for the atmosphere above the photosphere will tend to fall below the color temperature TE occupation numbers since the atoms are receiving only a diluted photospheric radiation field (i.e., a radiation field reduced roughly by a factor of the dilution factor; see eq. [34]) and since the local electron temperature is probably lower than the color temperature. However, ground levels will tend to be overpopulated relative to their color temperature TE occupation numbers for the same reasons that nonmetastable excited levels are underpopulated. For characteristic supernova color temperatures of order 10^4 K, the TE occupation numbers of the ground levels of most atoms and ions will be much larger than the sums of the occupation numbers of all their other levels. Thus, using the color temperature TE occupation numbers for the ground levels throughout the atmosphere is usually a small error.

Metastable levels are de-excited by second order radiative processes and collisions. Since second order radiative processes are always much weaker than first order processes and since collisional de-excitation rates are expected to be slow in the atmosphere due to low density, the occupation numbers of metastable states could well be higher than the LTE occupation numbers due to excitation—indirect excitation of course—by the diluted photospheric radiation field. In the absence of a detailed NLTE calculation of occupation numbers, it is reasonable to assume that metastable levels have color temperature TE occupation numbers throughout the atmosphere.

The foregoing arguments show why the ES model's assumption of no variation in ionization stage, ground level, or metastable level occupation numbers is reasonable. For nonmetastable excited levels the assumption of no variation is less justifiable since it seems clear that in general their occupation numbers should fall below the color temperature TE occupation numbers as one moves outward in the atmosphere from the photosphere. However, lacking a simple prescription for how these occupation numbers should vary, expediency allows them to be held constant also. It should be noted that many important lines in supernova spectra do arise from ground or metastable levels.

The ES model assumes the line source function given by equation (31) with with $\epsilon = 0$ and $G = 0$. The photon-line interaction required for this sort of source function is here called pure scattering; pure scattering is often called resonance scattering or pure two-level atom scattering. With pure scattering the upper level of a transition is isolated: i.e., the upper level is coupled only to the lower level and only by line photon absorption and emission. Assuming pure scattering means that all the complex interlocking of lines and continuum transitions are being ignored. It has been shown, however, in a limited NLTE study of supernova atmospheres that the pure scattering source function will often be much better than order of magnitude accurate (Feldt 1980). Given all the other accuracy limitations of the ES model, it does not seem *a priori* that the use of pure scattering will cause any further large decrease in accuracy. However, it certainly seems inconsistent to assume optical depths determined from color temperature TE occupation numbers and then

to assume that the line source functions behave as if the upper levels of lines acted as if they were isolated. The resolution of this paradox is that it is hoped that the color temperature TE occupation numbers are the better approximations for the important lower levels and the occupation numbers implied by the pure scattering picture are the better approximations for the important upper levels. It is argued above why for ground and metastable levels the color temperature TE occupation numbers are good *a priori* estimates. It was also argued why the populations of nonmetastable excited levels should fall below the color temperature TE photospheric occupation numbers. Since this is the case, it is plausible that these occupation numbers should be established mainly by line photons. The assumption that each upper level acts as if it were isolated is then a simplifying assumption. To improve on the pure scattering assumption requires in general NLTE calculations that account for all the interlocking of lines and continuum transitions by solving the rate equations (SA, p. 137 and 374).

From the arguments given above, it is expected that the ES model treatment of a line is better the more isolated the line is from other lines. On the other hand, lines which are strongly coupled to other lines might be expected to be poorly handled by the ES model treatment. One particular case where the ES model treatment fails very noticably is for the Hα line profile that appears in SN II spectra. This line profile often shows a strong emission excess over what the ES model line treatment predicts (see, e.g., Branch et al. 1981 and § V*c*). This is understandable since the lower level of the Hα line is neither a ground level nor metastable and since both its lower and upper line levels are strongly coupled to other levels and the continuum. Because the Hα is an extremely strong line in SN II spectra, the limited fitting ability of the ES model line treatment is particularly unfortunate. Of course, one can introduce an *ad hoc* net line emission (i.e., a nonscattering emission contribution in the source function that causes line emission to exceed line absorption) by setting the G and ϵ to nonzero values in equation (31). By adjusting the G and ϵ values, one can fit line profile emission excesses. However, without a prescription for interpreting these fitted G and ϵ values, the fitting exercise is cosmetic.

The absolute size of the photospheric line optical depths for an ion for an ES model calculation can be determined in at least two ways. The optical depths for strong ion lines can be used as fitting parameters for a given spectrum. This procedure can be used for quite accurate line identification. Using the color temperature or a free-parameter excitation temperature, an estimated photospheric electron density, and assuming TE, the elemental abundances can be estimated from the fitted line optical depths. It is often convenient to begin such a fitting procedure by calculating TE-predicted optical depths from an an assumed composition (e.g., solar composition), the color temperature, and an estimated photospheric electron density; this approach is followed for the analysis of SN 1987A optical spectra given in § V. Because of the many assumptions required, TE abundance estimates made from a fitting procedure will be of only very qualitative accuracy. However, radical departures from an assumed composition may be detectable.

A second procedure for determining TE photospheric line optical depths for an ES model calculation would be to calculate their values and an electron density using an explosion calculation density and composition, and an observed color temperature or a free-parameter excitation temperature. This procedure could be used in evaluating the physical plausibility of an explosion calculation. While using this procedure Branch et al. (1985) found for SNe Ia that stratified compositions are less satisfactory than more homogenous compositions. In these ES model calculations a stratified explosion calculation composition yielded line features that were generally too narrow. An *ad hoc* mixing of the composition resulted in improved fits. Mixed compositions are physically plausible. Stratified compositions are the usual result of one-dimensional explosion calculations. However, turbulent mixing of layers, an intrinsically three-dimensional process, is thought to occur in supernovae (e.g., Nomoto, Thielemann, and Yokoi 1984; Benz and Thielemann 1990). The *ad hoc* mixing of the compositions for the calculation of supernova spectra has also been done by others for both SNe Ia (e.g., Wheeler et al. 1986) and SNe II (e.g., Swartz, Harkness, and Wheeler 1989).

The ES model of a photospheric phase supernova outlined in this section is a naive model with many free parameters and uncertainties. However, calculations with the ES model are very useful in line identification and in determining photospheric velocities. With other assumptions qualitative TE elemental abundances can be estimated. It is easy to think of simple variations on the ES model in order to treat particular cases. The analysis of SN 1987A data given in § V is an example of ES model analysis. More advanced analyses of supernova atmospheres have been done and are needed for more quantitative determinations and for better understanding of the conditions in supernova atmospheres. In particular, NLTE calculations are necessary. Supernova calculations with NLTE have been done by, e.g., Feldt (1979, 1980), Höflich (1988), Swartz,

Harkness, and Wheeler (1989), and Eastman and Kirshner (1989). It should be emphasized that since the explosion mechanisms and progenitors of supernovae are uncertain, quantitative understanding of the supernova atmosphere is essential in order to distinguish between proposed supernova models. However, such advanced calculations will always be much more computer intensive than ES model calculations. Therefore, ES model calculations will remain useful for quick analyses, preliminary analyses, and analyses where detailed results are not needed.

IV. LINE FORMATION WITH THE SOBOLEV METHOD AND THE ELEMENTARY SUPERNOVA MODEL

In this section, line formation is examined with calculations that use the Sobolev method (see § II) and the ES model (see § III). A catalogue of line profiles for various special choices of the ES model's parameters is presented and discussed. This catalogue shows some of the range of behaviors possible for line profiles and demonstrates how such behaviors can arise.

Figure 1 shows a schematic representation of the ES model with line radiative transfer. The z-axis is aligned with the line of sight to an observer with z increasing toward the observer and $z = 0$ at the center of the photosphere. Consider a line with line center wavelength λ_0. Photons that are emitted by the line toward the observer from material that lies on the plane perpendicular to the z-axis at the point z will have an observer frame wavelength given by

$$\lambda = \lambda_0 \left[1 - \left(v_{\rm ph}/R\right) z/c\right] \ , \tag{69}$$

where the first order Doppler formula has been used and where, recalling from § III, $v_{\rm ph}$ is the photospheric velocity, R is the photospheric radius, and $\left(v_{\rm ph}/R\right)$ is equal to the directional velocity derivative at all points in the atmosphere. Equation (69) shows that the z coordinate defines the location of the CD velocity surfaces. In Figure 1, a CD velocity surface is displayed for $z > 0$. Line photons emitted toward the observer from CD velocity surfaces with $z > 0$ are blueshifted from the line center wavelength. Those CD velocity surfaces with $z < 0$ emit redshifted line photons toward the observer. The photons that are emitted toward the observer from the occulted region strike the photosphere and are absorbed. Additionally, there can be no line emission from points inside the photosphere. Since no observable line photons can originate from the occulted region and from the interior of the photosphere, these regions will collectively be called the excluded region. Of course, outside of the outer cutoff boundary of the atmosphere there is no line emission or line scattering.

A technicality that should be mentioned is that the computer program used to calculate the line profiles in this section and the synthetic spectra in § V actually uses the first order Doppler formula for frequency rather than for wavelength. Whether the frequency or wavelength first order formula is used makes no difference in physical accuracy. However, the flux from a CD velocity surface located at z and assigned a wavelength according to the frequency formula will have a wavelength shift of about

$$\lambda_0 \left[\left(v_{\rm ph}/R\right) z/c\right]^2 \tag{70}$$

from the wavelength that would have been assigned using the wavelength formula provided that the velocities are sufficiently low that the third order term in (v/c) is unimportant. Thus, there will be an overall wavelength-dependent shift between profiles calculated with the two formulae. There will be other subtle distinctions between the results of two formulae in multiple line cases and cases with wavelength-dependent photospheric flux.

The simplest case of line formation is when there is only a single line transition to consider. Figure 2 shows the line profile that results in this case for a line with line center wavelength $\lambda_0 = 5000$ Å. Recalling that the ES model assumes pure scattering (see § III), it is easy to understand how the profile in Figure 2 arises. Far from the line center wavelength, all the photospheric flux propagates without scattering since the CD velocity surfaces that correspond to these wavelengths are so far from the photosphere that they have negligible opacity. Since there is also negligible emission at these wavelengths, the emergent flux is just a continuum formed by the photospheric flux. The absorption feature or trough of the line profile is due to

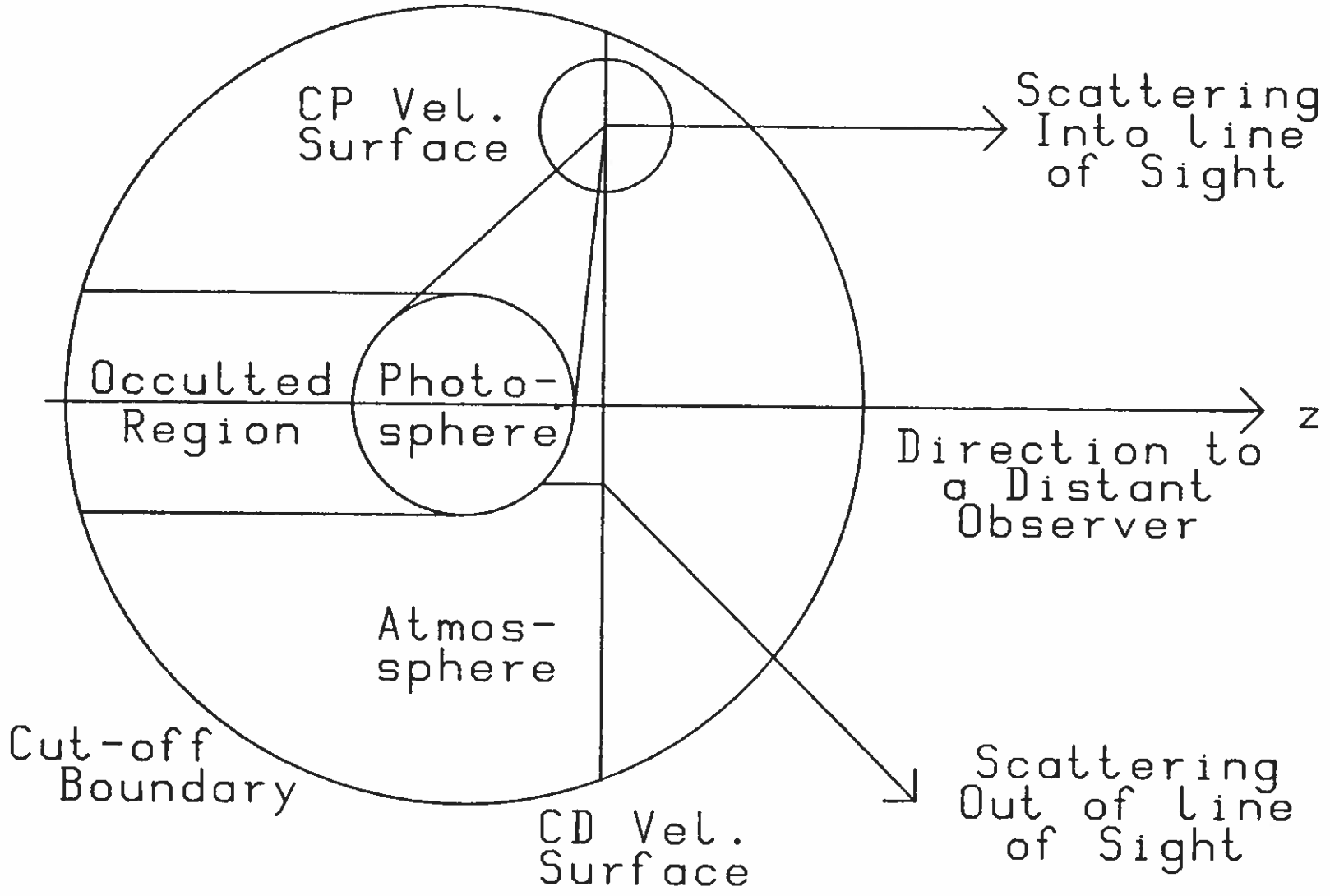

Fig. 1: *Schematic representation of the ES model of a supernova.*

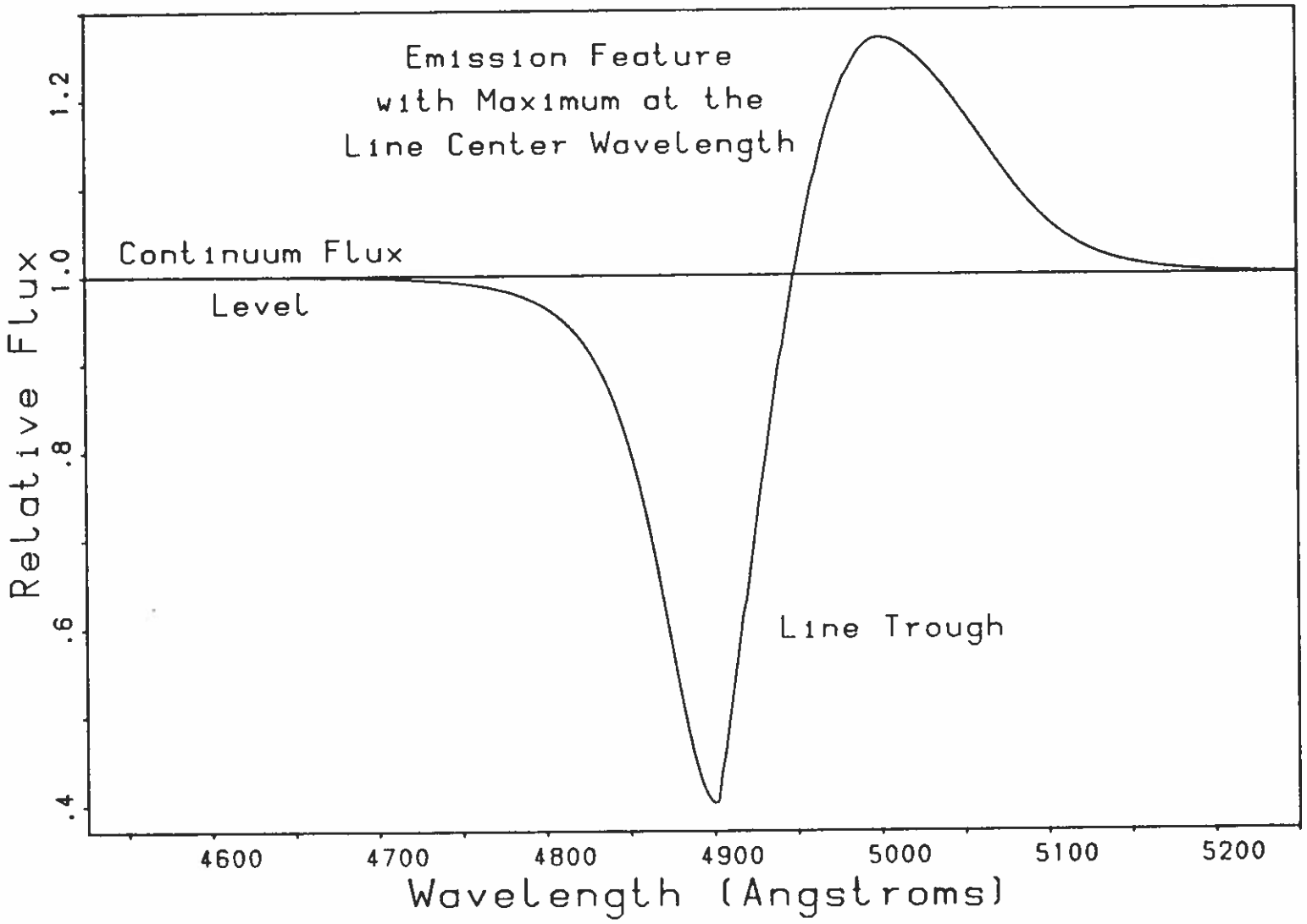

Fig. 2: *Typical P Cygni line profile.*

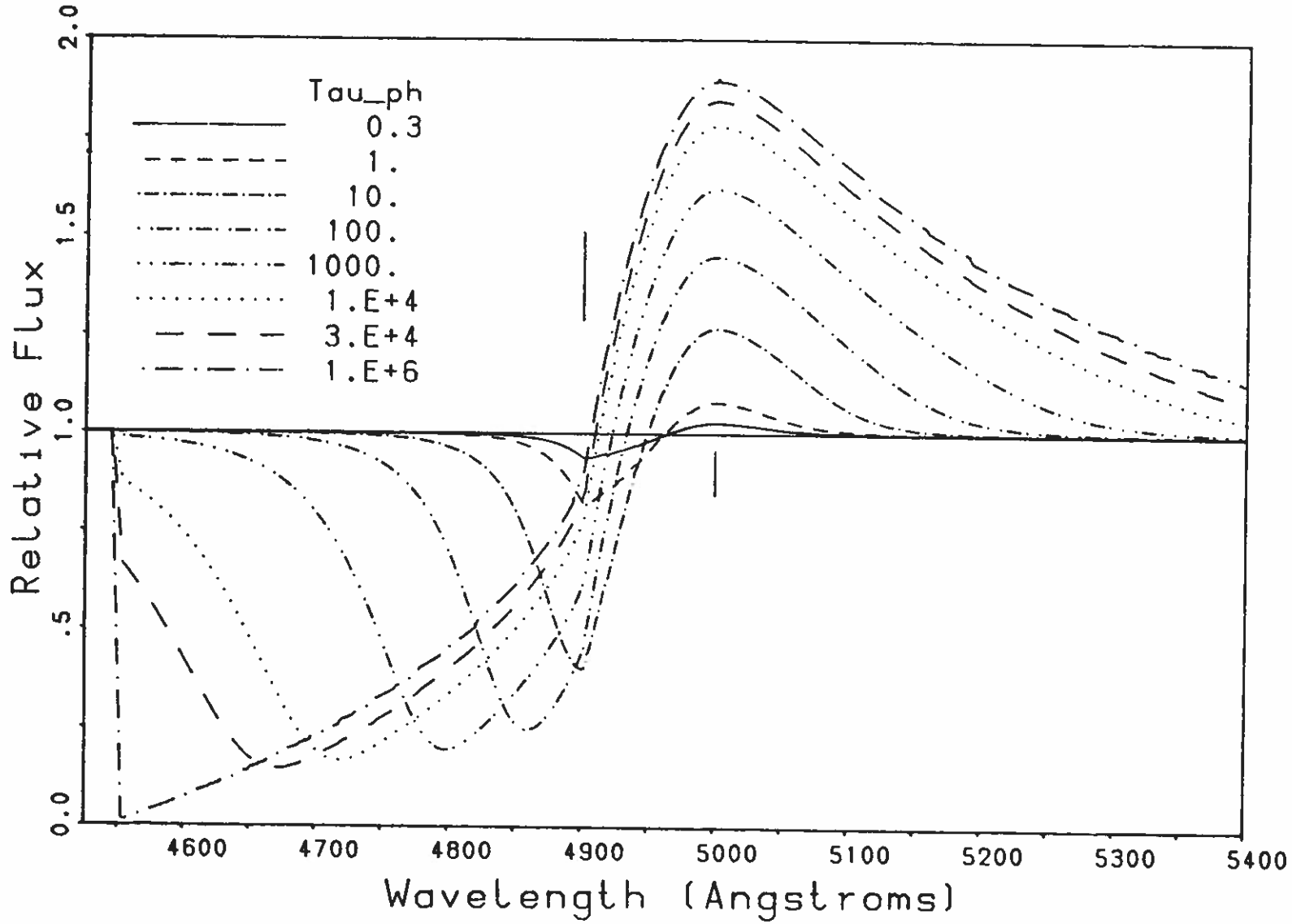

Fig. 3: *Line profiles for varied photospheric optical depth* $\tau_{\rm ph}$.

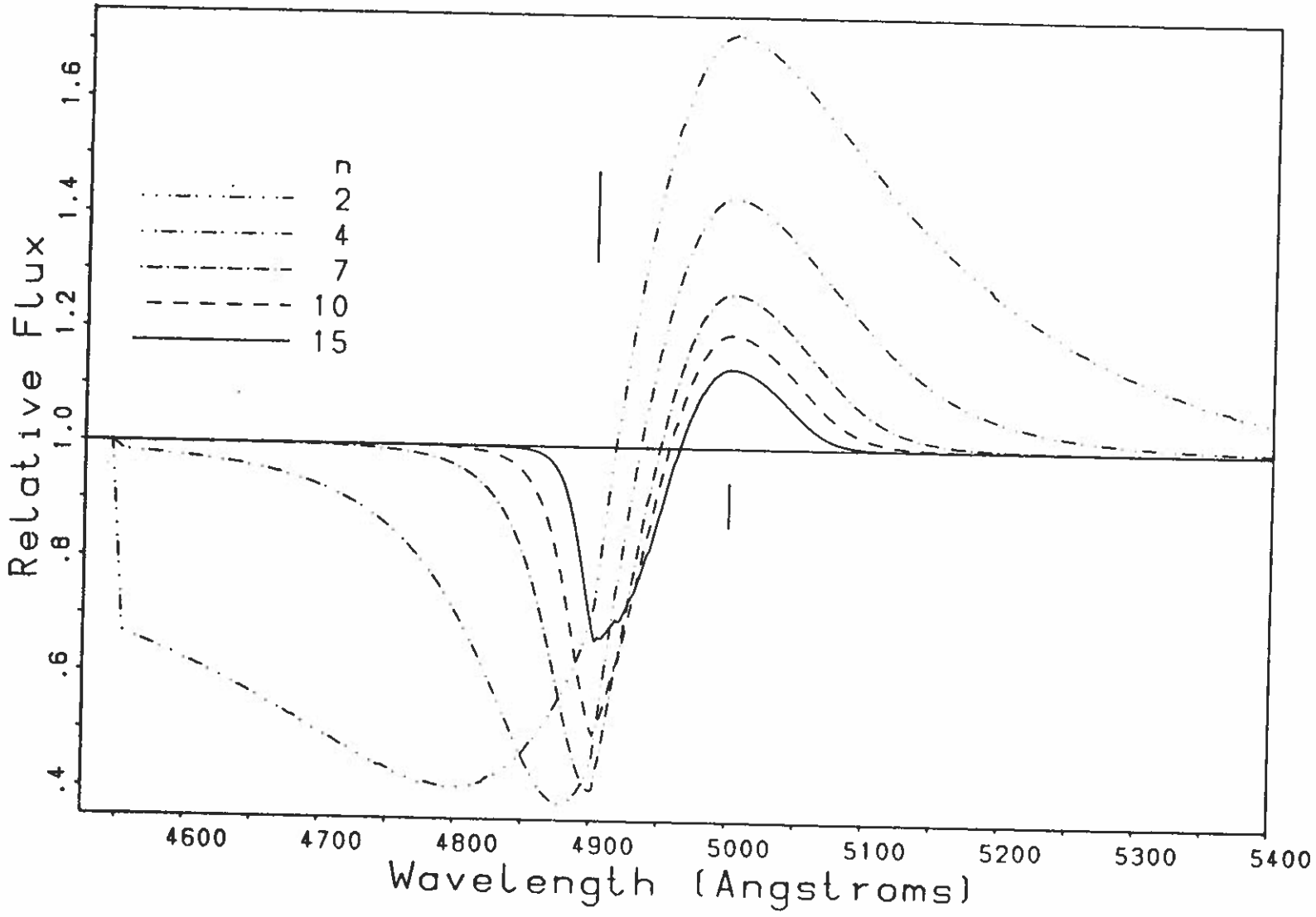

Fig. 4: *Line profiles for varied inverse power-law index n.*

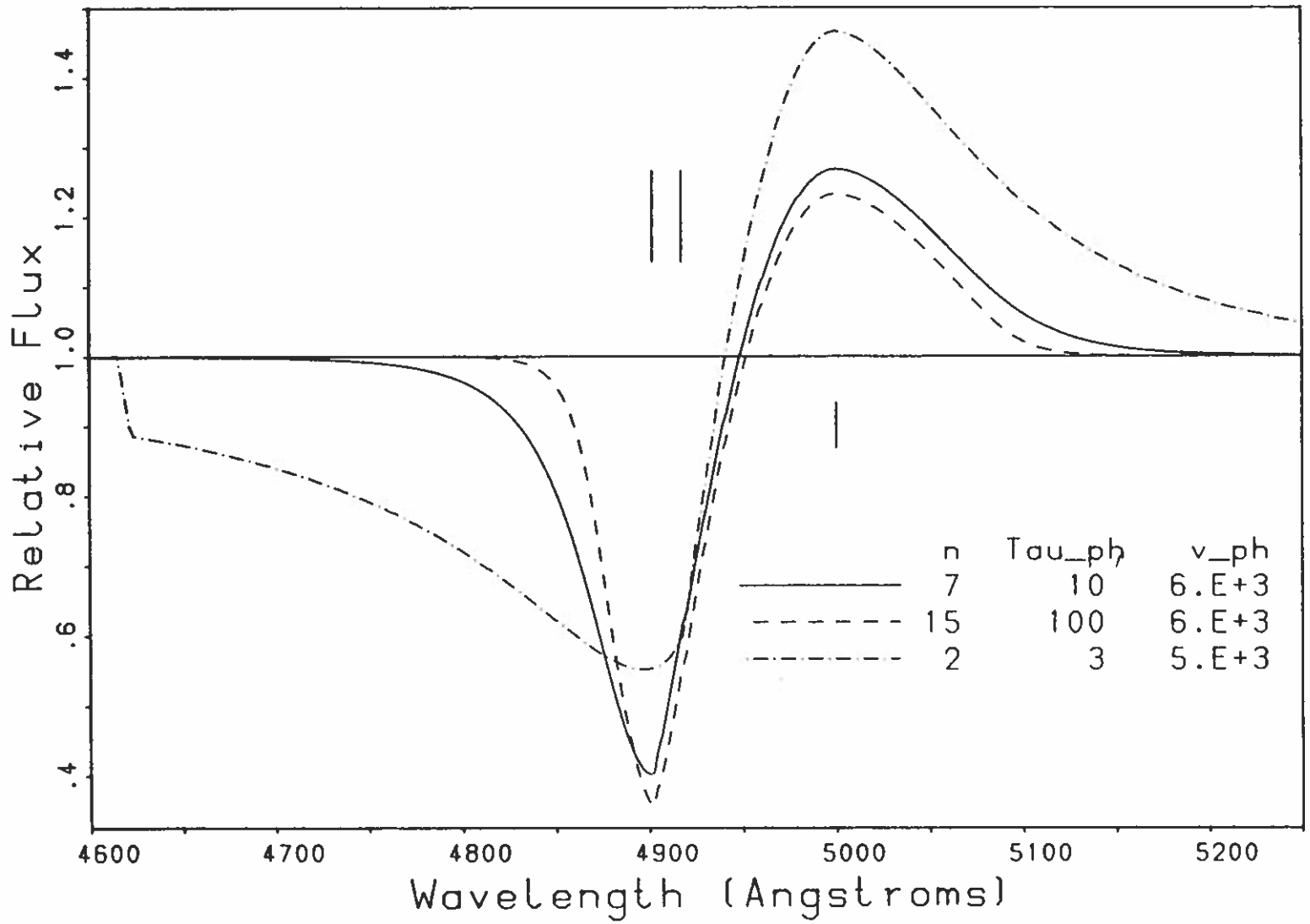

Fig. 5: *Line profiles for various combinations of ES model parameters.*

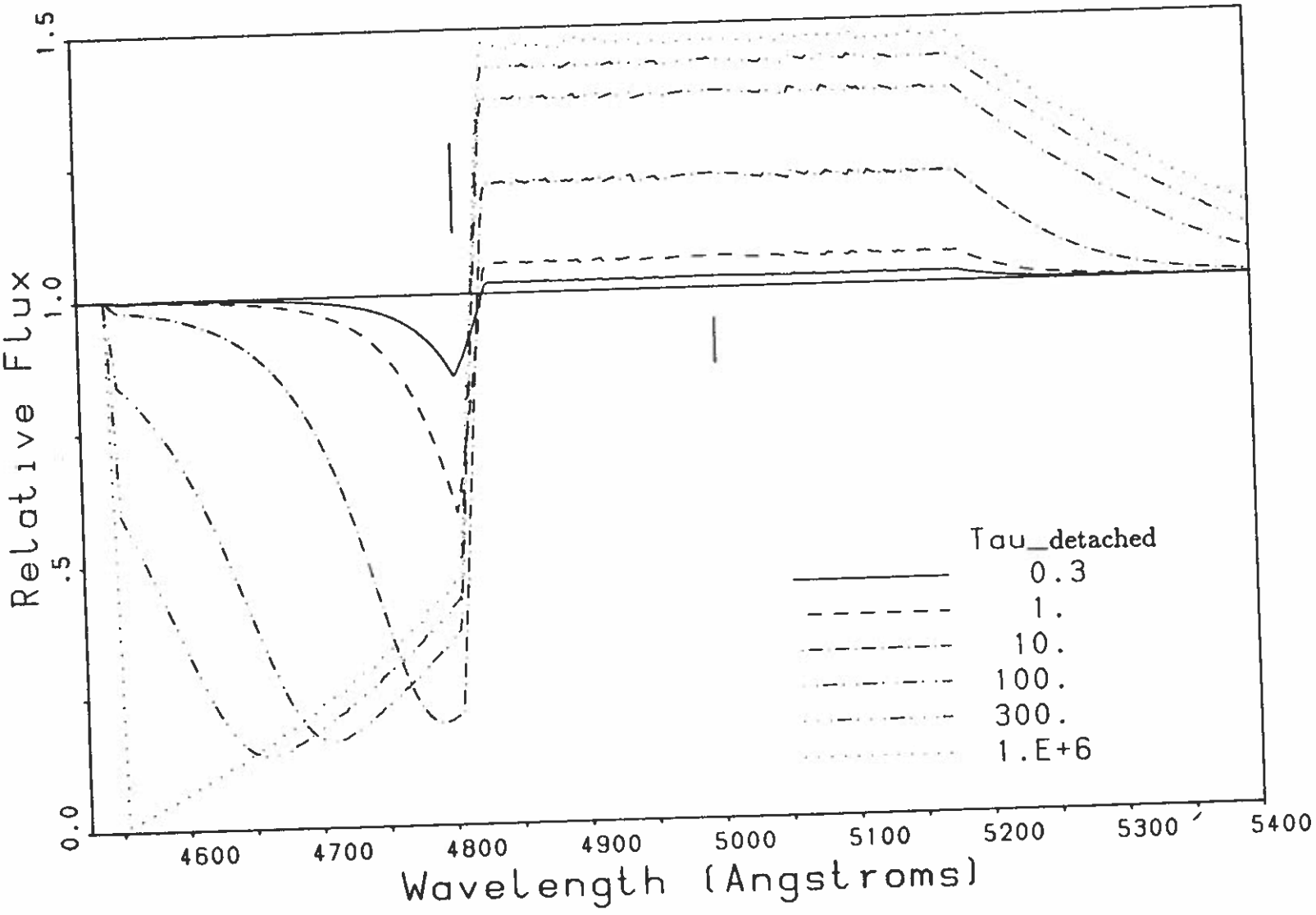

Fig. 6: *Line profiles for a detached atmosphere.*

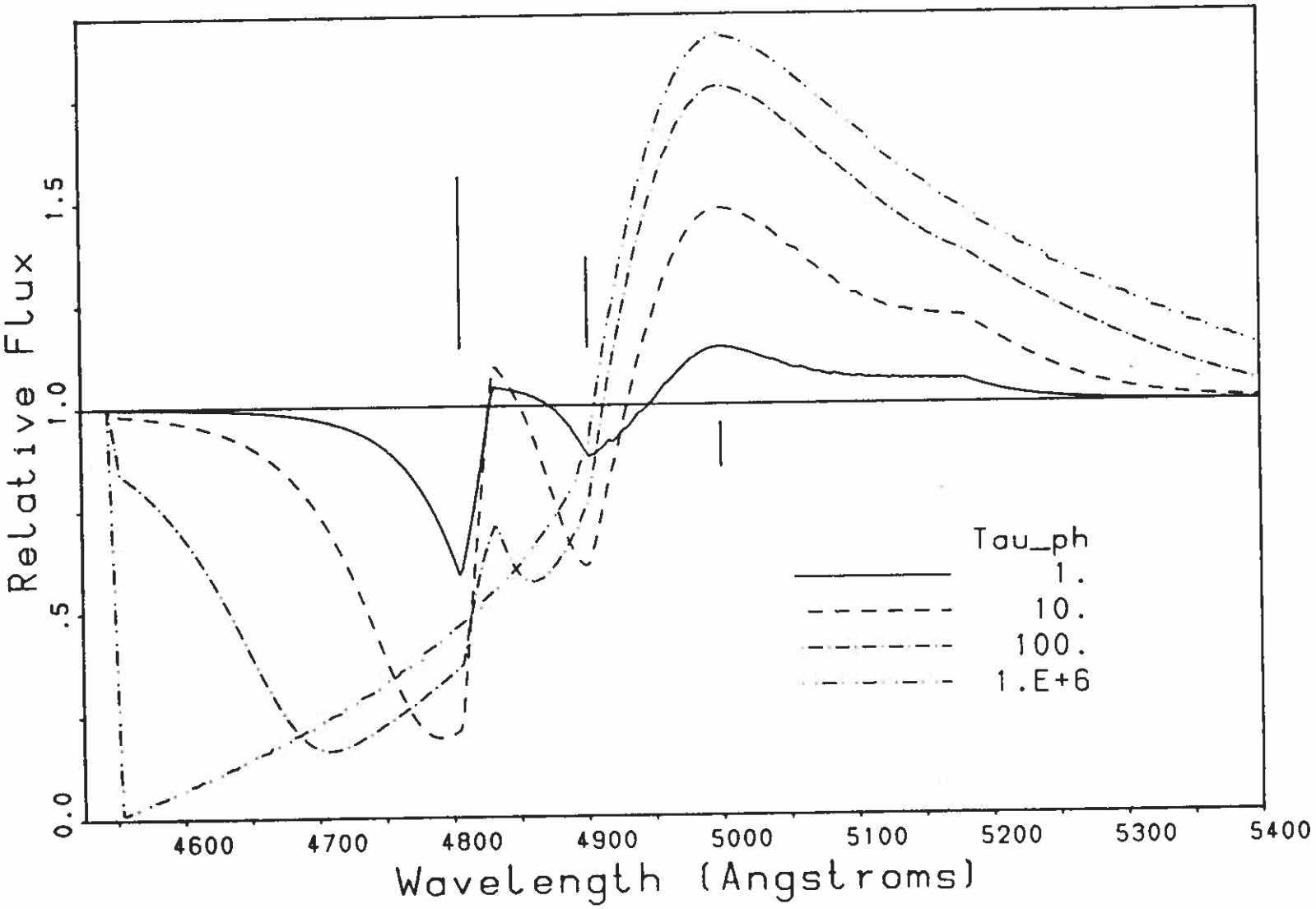

Fig. 7: *Line profiles for an atmosphere with a density peak.*

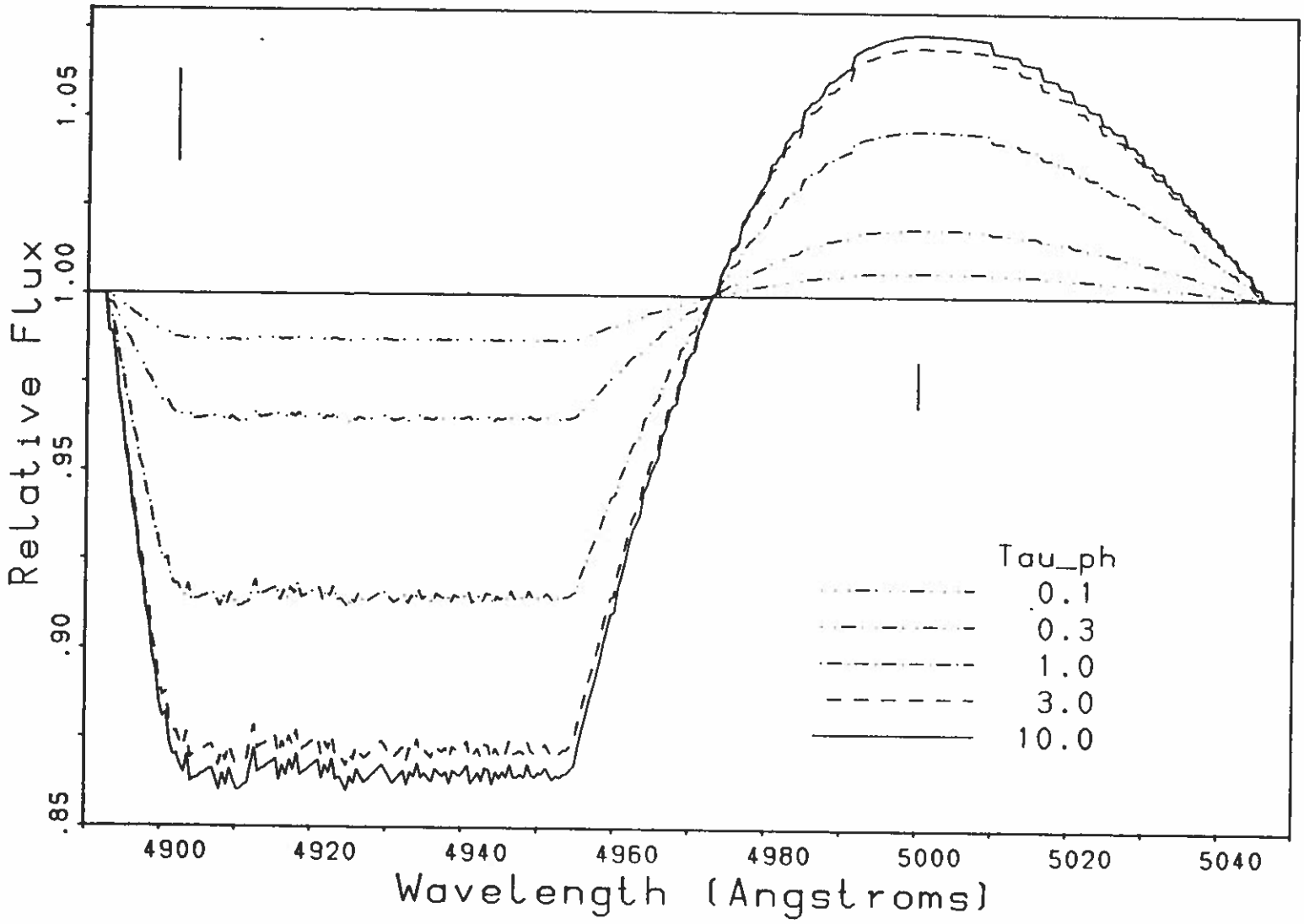

Fig. 8: *Line profiles for a geometrically thin atmosphere.*

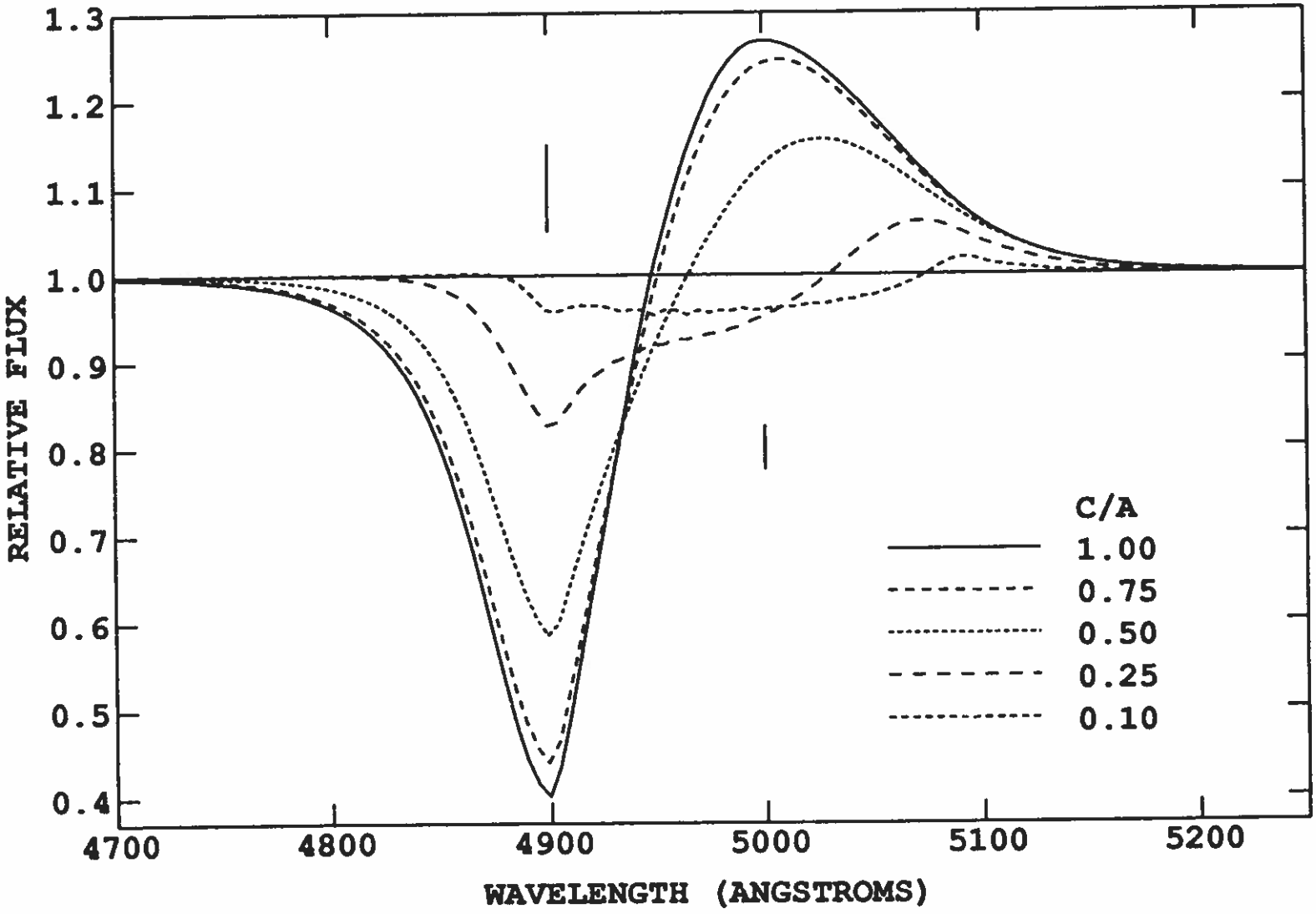

Fig. 9: *Line profiles for an oblate axisymmetric ellipsoidal ES model with varied c/a : i.e., varied ratio of the symmetry semiaxis to the perpendicular semiaxis.*

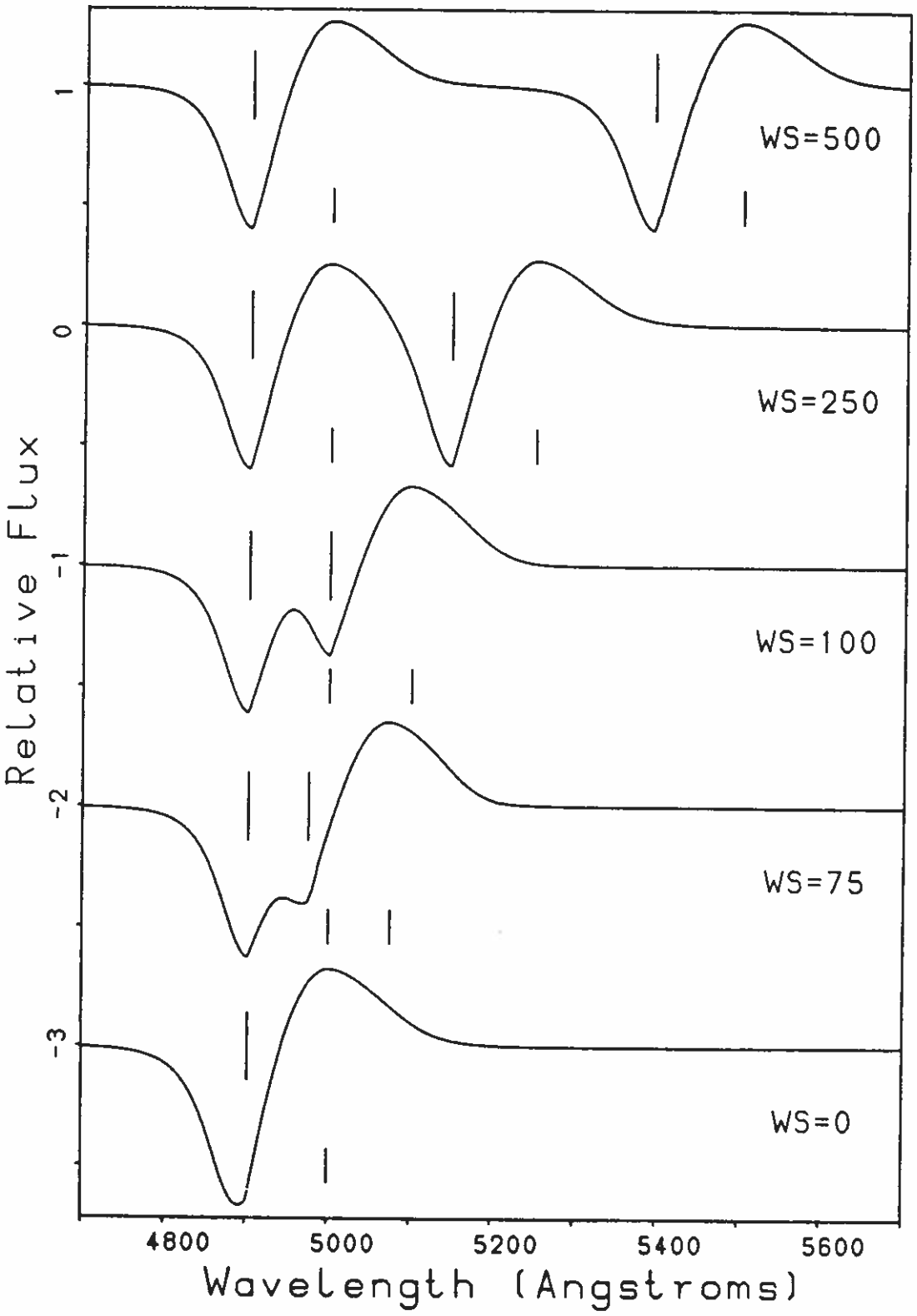

Fig. 10: *Synthetic spectra with two lines both with photospheric optical depth 10 and with varied line center wavelength separation* WS.

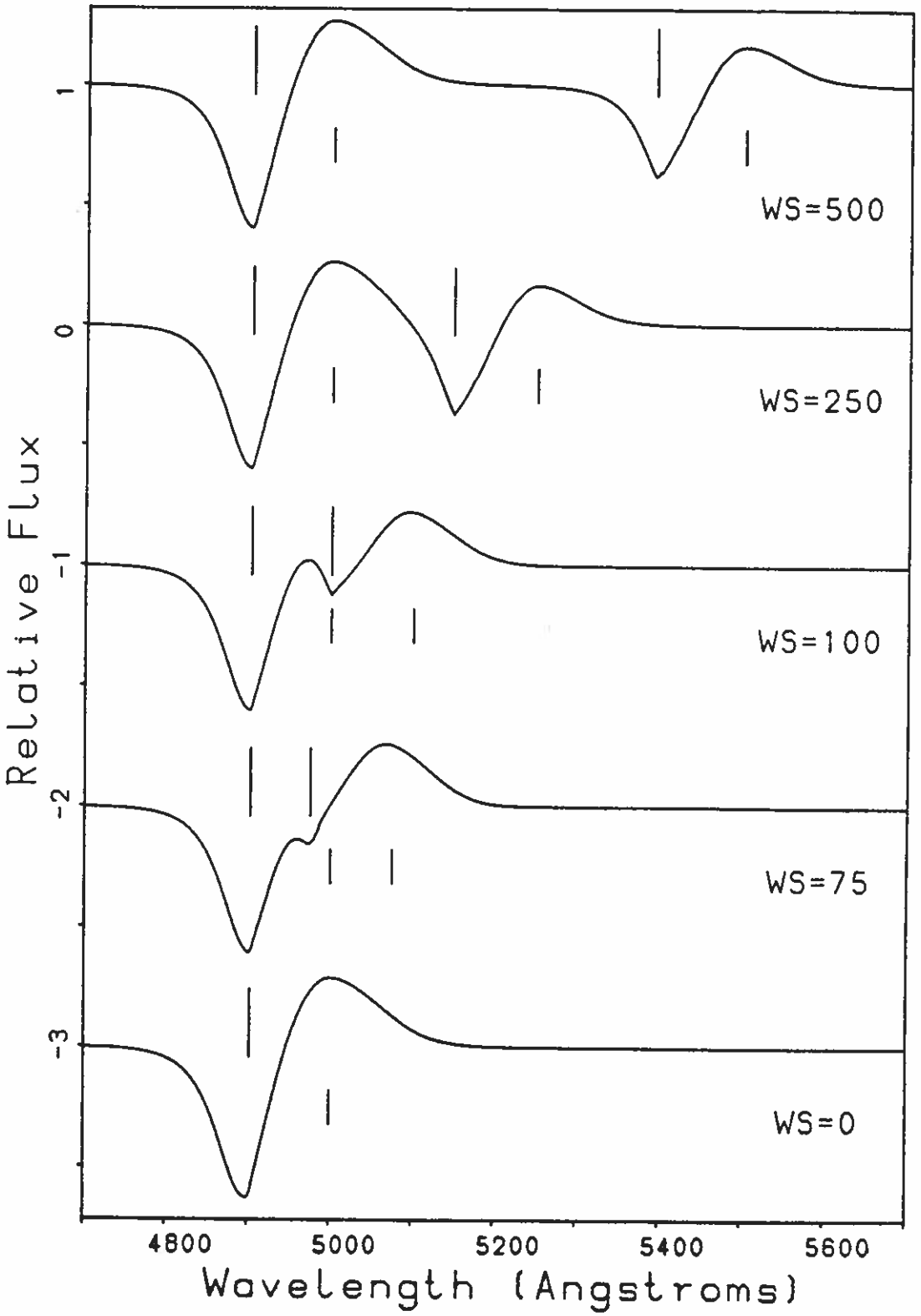

Fig. 11: *Synthetic spectra with two lines with photospheric optical depths 10 and 9 and with varied line center wavelength separation* WS.

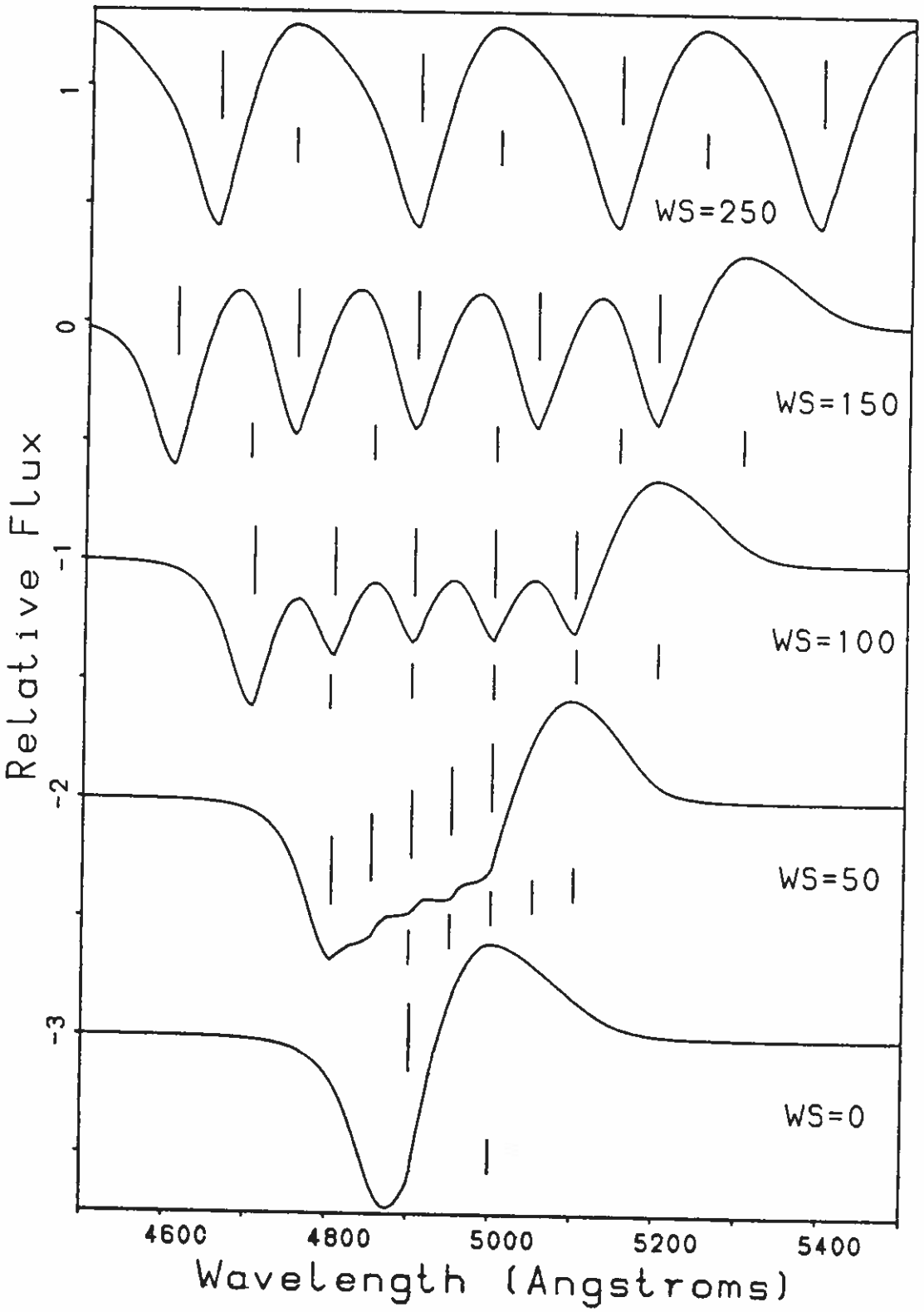

Fig. 12: *Synthetic spectra with five lines all with photospheric optical depth 10 and with varied line center wavelength separation* WS.

scattering out of the line of sight of photospheric flux emitted toward the observer. The regions of CD velocity surfaces that scatter the photospheric flux out of the line of sight have projections that are exactly coincident with the projection of the photosphere. Here the projection of the photosphere will be called the photodisk and the regions of the CD velocity surfaces that coincide with the photodisk will be called the photodisk regions of the CD velocity surfaces. Since only photodisk regions of CD velocity surfaces that lie at least partially outside of the excluded region can scatter photospheric flux out of the line of sight, the trough is a feature on the blue side of the line profile. At the wavelengths that correspond to $z \leq 0$, photodisk regions of the CD velocity surfaces lie entirely in the excluded region, and thus the photospheric flux suffers no line scattering while propagating through the atmosphere. The emission feature of the line profile is due to flux scattered into the line of sight from the atmosphere limb added to unscattered photospheric flux and the flux scattered toward the observer from the photodisk regions of the CD velocity surfaces. The atmosphere limb is that region of the atmosphere whose projection forms an annulus about the photodisk. Since the limb region is symmetric about the $z = 0$ plane, the limb emission is approximately symmetric about the line center wavelength; the use of the the first order Doppler formula formula for frequency rather than for wavelength breaks the exact symmetry. The emergent line emission feature does not exhibit this symmetry due to the interference of the trough feature on the blue side of the line profile.

The maximum of the emission feature in Figure 2 is exactly at the line center wavelength. This exact coincidence occurs because the CD velocity surface for the line center wavelength is located at $z = 0$. This location implies that the entire photospheric flux emerges from the atmosphere without being scattered by a CD velocity surface and that the limb contribution to the emergent flux will be at its greatest. If the Sobolev method assumption that the macroscopic atmosphere velocities are much greater than the random atmosphere velocities begins to lose validity, then emission maximum in more exact calculations tends to redshift from the line center wavelength. This and other departures of more exact calculation results from Sobolev method results are discussed by Hamann (1981).

The calculation of the line profile that emerges from an atmosphere requires the integration of the emergent specific intensity over the projected area of the atmosphere at each wavelength. In the Sobolev method, the integration at a given wavelength is in fact an integration over the emission and transmission from the particular CD velocity surfaces that correspond to that wavelength. Of course, there is no contribution from the CD velocity surfaces that lie in the excluded region and there will be unattenuated photospheric flux when there are no intervening CD velocity surfaces. When only a single line transition needs to be considered, the expression for the emergent specific intensity for the wavelength that corresponds to the CD velocity surface at z is

$$I_{\mathrm{emergent}} = \begin{cases} S(r)\,\{1 - \exp[-\tau(r)]\} + I_{\mathrm{ph}} \exp[-\tau(r)] & \text{for } p < R, \text{ but outside the excluded region;} \\ I_{\mathrm{ph}} & \text{for points in the excluded region;} \\ S(r)\,\{1 - \exp[-\tau(r)]\} & \text{for } p > R, \end{cases} \tag{71}$$

where p is the impact parameter measured from the z-axis in the plane of the CD velocity surface and I_{ph} is the photospheric specific intensity at the given wavelength. For the cases where multiple line transitions need to be considered, equation (71) can easily be generalized using equation (22) from § II.

Since the ES model assumes pure scattering, a line source function at a given point can only be determined by photospheric flux and by line flux emitted from bluer lines (see § II). The photospheric flux contribution is simply determined by the cone of beams emitted by the photosphere and incident on the point. The flux contribution from the bluer lines is emitted by spherical CP velocity surfaces that are centered on the point; this bluer line flux then converges on the point. Both a cone of photospheric beams and a CP velocity surface are shown schematically in Figure 1. The photospheric beams and beams from all but the innermost CP velocity surface will be diminished by transfer through CP velocity surfaces as they propagate to the point. In general, equation (22) must be integrated over all solid angle in order to determine the line source function at the point.

The remainder of this section presents the catalogue of line profiles. The initial ES model used for the calculations was spherically symmetric, and had a photospheric velocity $v_{\rm ph} = 6000\,{\rm km\,s^{-1}}$, an inverse power-law density profile with index $n = 7$, and an outer cutoff radius $r_c = 5R$. These characteristics were modified in various ways in order to investigate the range of line formation behavior. The specific intensity emitted by the photosphere was wavelength-independent. Since the ES model assumes pure scattering, the line source function for those cases where only a single line was considered is exactly given by equation (33): i.e., $S(r) = W(r)I_{\rm ph}$. Most of the figures in the catalogue have short and long vertical line segments to mark the line center and photospheric wavelengths, respectively. The photospheric wavelength is defined to be the wavelength that corresponds to the CD velocity surface that is tangent to that part of the photosphere that is nearest the observer. This definition applies to both spherically symmetric and asymmetric versions of the ES model.

Figure 3 presents the line profiles for a case with varied photospheric line optical depth. The first interesting feature to note is that for the lines with $\tau_{\rm ph} \leq 10$, the line trough minimum is nearly at the photospheric wavelength. For $\tau_{\rm ph} > 10$, the wavelength of the trough minimum decreases with increasing $\tau_{\rm ph}$. This behavior is easily understood. First, note that due to the exponential factors in the Sobolev method expression for line transfer through a velocity surface (see eq. [21]), the transmitted contribution is nearly at its maximum value for velocity surface optical depth $\tau << 1$ and small for $\tau >> 1$, whereas the line source function contribution is small for $\tau << 1$ and nearly at its maximum value for $\tau >> 1$. The two regimes, $\tau << 1$ and $\tau >> 1$, are called unsaturated and saturated, respectively. When the photodisk region of the CD velocity surface tangent to the photosphere is largely unsaturated, there is a strong tendency for the line trough minimum to form at the photospheric wavelength. This is because at a redder or bluer wavelength there is a strong tendency for more of the photospheric flux to propagate through the atmosphere without scattering: at a redder wavelength because some of the corresponding CD velocity surface photodisk region is inside the excluded region; at a bluer wavelength because of the decrease in the effective average optical depth of the CD velocity surface photodisk regions with radius. However, when the photodisk region of the CD velocity surface tangent to the photosphere is saturated, there is negligible decrease in the scattering power of the CD velocity surface photodisk regions as one moves away from the photosphere until the effective average optical depth falls to of order 1. Effectively no photospheric flux is transmitted by the saturated CD velocity surface photodisk regions and all the flux emerging from them is due to the line source function. Now the red side of the line profile trough due to a line that is saturated out to some large radius is formed by flux emitted by saturated CD velocity surface photodisk regions plus limb emission. Thus, the flux forming the red side of the trough tends to scale with the effective average of the source function for the CD velocity surfaces. Since the line source function decreases with radius, the flux forming the red side of the trough decreases with decreasing wavelength. However, as radius increases a point must be passed where the effective average optical depth of the CD velocity surfaces must decrease below 1. When this happens the CD velocity surface photodisk regions become increasingly transparent to the photospheric flux and the source function contribution to the emergent flux from the whole CD velocity surface decreases toward zero; therefore, the line profile curve rises toward the continuum flux level. This physical picture shows why strong lines tend to have trough minima at bluer wavelengths than the photospheric wavelength.

The wavelength of the trough minimum for the strong line case can be estimated from the z coordinate where the line optical depth is 1. For an inverse power-law density profile,

$$\lambda_{\rm min} \propto z_{\rm min} \sim z_{\rm ph}\,(\tau_{\rm ph})^{1/n} \quad . \tag{72}$$

The behavior of the trough minimum for the saturated case profiles shown in Figure 3 is roughly consistent with equation (72). The exact analytical determination of the wavelength of the minimum is complicated by the fact that the optical depth varies across the CD velocity surfaces and because there is emission from the atmosphere limb that tends to fill in the trough.

The profiles for the small $\tau_{\rm ph}$ cases in Figure 3 show clearly that net absorption is greater than net emission. The reason for this loss in net flux is that some photons are scattered back from the atmosphere to the photosphere where the calculation assumes that they are effectively destroyed. In the physical interpretation of the ES model, the line scattered photons that strike the photosphere are assumed to help to establish the conditions at and below the photosphere that give rise to the photospheric flux. Of the observer-directed line photons, it is those line photons emitted from the occulted region that strike the

photosphere. In a line profile calculation, the flux from the occulted region is simply never calculated. For the larger $\tau_{\rm ph}$ cases in Figure 3, the net loss in flux is not clearly seen. The reason for this is that in these cases relatively more of the scattered flux is scattered at larger radii. As the radius of a point increases, the solid angle at the point subtended by the photosphere decreases, and therefore the fraction of flux scattered back from the point to the photosphere decreases. Thus, having relatively more of the flux scattered from larger radii causes the size of the net loss in flux to decrease relative to the size of the total amount of flux scattered. The decrease in relative size of net loss, of course, makes the net loss harder to identify.

The maximum of the emission feature in Figure 3 for the larger $\tau_{\rm ph}$ cases increases approximately with the logarithm of $\tau_{\rm ph}$, until $\tau_{\rm ph} \sim 3 \times 10^4$. The logarithmic increase can be easily understood if the approximation is made that

$$S(r)\,[1-\exp(-\tau)] = \begin{cases} S(r) & \text{for } \tau > 1 \ ; \\ 0 & \text{for } \tau < 1 \ . \end{cases} \tag{73}$$

Using equation (73), the approximate net flux at the line center wavelength is given by

$$\begin{aligned} F(z=0) &= \pi I_{\rm ph} R^2 + 2\pi \int_R^{r_1} dr\, r S(r) \\ &\approx \pi I_{\rm ph} R^2 \left[\!\left[1 + \left(\frac{1}{2}\right)\left\{ \ln\left[r_1/R\right] + \ln(2) - \frac{1}{2} \right\} \right]\!\right] , \end{aligned} \tag{74}$$

where $r_1 = r(\tau = 1)$ and where all terms of order 1 and higher in (R/r_1) have been neglected. Since $r_1 = R\,(\tau_{\rm ph})^{1/n}$, it follows that $F(z=0) \propto \ln(\tau_{\rm ph})$.

The reason the emission maximum stops increasing logarithmically with $\tau_{\rm ph}$ for $\tau_{\rm ph} \gtrsim 3 \times 10^4$ is that the saturated region of the atmosphere cannot expand beyond the atmosphere's cutoff radius of $5R$. As the entire atmosphere approaches saturation, the emergent line profile must asymptotically approach a limiting shape. This is because when the entire atmosphere is saturated, the line optical depth is effectively infinite throughout the atmosphere and the radiative transfer is thus everywhere independent of the optical depth. The emergent specific intensity in this case is given by equation (71) with the $\exp\left[-\tau(r)\right]$ factors set to zero. In Figure 3, the calculation for the profile for the $\tau_{\rm ph} = 10^6$ case had $\tau(5R) \approx 10$, and thus the atmosphere was entirely saturated. The complete saturation accounts for the very steep blue edge of the line trough. The steep blue edge occurs at the wavelength corresponding to $z \approx 5R$, where the CD velocity surfaces suddenly change from being saturated to having no opacity at all. The blue edge is not exactly vertical due to the spherical shape of the outer boundary of the atmosphere.

Figure 4 presents the line profiles for a calculation where $\tau_{\rm ph} = 10$ and where the inverse power-law index n was varied. Fixing the photospheric optical depth while decreasing n has the effect of increasing the total scattering power of the atmosphere. Thus, it is not surprising that the size of the line profiles increases as n decreases. Except for the growth of an extended blue wing to the line trough, the shape of the line profiles shows little qualitative change as n is decreased. The development of the extended blue wing of the trough with decreasing n is just a consequence of the fact that with the gentler decrease in opacity with radius there is relatively more opacity at larger radii. The steep blue edge that appears for the $n = 2$ case is again a result of having finite cutoff radius for the atmosphere.

The fact that the line profiles for varied $\tau_{\rm ph}$ and varied n fail to show striking qualitative variations suggests that it is difficult to determine photospheric optical depth and opacity distribution independently. Additionally, the photospheric velocity is a third parameter that can be varied without changing the line profile qualitatively, since the width scale of the line profile just varies linearly with the photospheric velocity. Behavior degeneracy of various combinations of these three parameters presents a difficulty for spectral analysis. In order to demonstrate the degree of the behavior degeneracy possible, a calculation was done with three sets of the three parameters. The three sets of parameters were chosen to show how widely each of the parameters could be varied and still obtain a reasonably good agreement between the line profiles. The line profiles from this calculation and the chosen parameter sets are shown in Figure 5. There are two long vertical line segments in Figure 5, since the two chosen photospheric velocities give rise to two photospheric wavelengths. It was found that only a relatively small variation in the photospheric velocity was allowed. This is not surprizing since, as discussed above, the trough minimum for an unsaturated line has a strong tendency to form at the photospheric wavelength. Thus, in spectral analysis the photospheric velocity can usually be determined without too much ambiguity. However, rather drastic variations of the $\tau_{\rm ph}$ and n

combination could be made to yield rather similar profiles. There are real qualitative differences between cases with small n and $\tau_{\rm ph}$ and those with large n and $\tau_{\rm ph}$. However, in an observed spectrum the continuum will have a slope and the line features are likely to be overlapping. Thus, the qualitative differences will probably not be readily detectable. Simple morphological analysis of line profiles in spectra cannot therefore be expected to give clear insight into the density profile of a supernova atmosphere.

Figure 6 shows the line profiles that arise from a model with a detached atmosphere. The detached-atmosphere model has zero opacity from the photospheric radius R out to a radius of $2R$; at $2R$ there is a discontinuous jump to a detached boundary opacity. The optical depths at the detached boundary are displayed in Figure 6. At radii greater than $2R$, the optical depths decay with the usual inverse power law with index 7. For Figure 6, the longer vertical line segment marks the wavelength corresponding to the detached boundary velocity. This velocity is $12000\,{\rm km\,s^{-1}}$. The most striking features of the line profiles in Figure 6 are the flat tops of the emission features. To explain the flat tops, note that flux due to the line source function that is emitted by an annular area with fixed inner and outer radii of a CD velocity surface is independent of z:

$$\begin{aligned} F_{\rm annulus} &= 2\pi \int_{p_1}^{p_2} dp\, pS(r)\{1-\exp[-\tau(r)]\} \\ &= 2\pi \int_{r_1}^{r_2} dr\, rS(r)\{1-\exp[-\tau(r)]\}\ , \end{aligned} \tag{75}$$

where

$$r = \sqrt{p^2+z^2} \qquad \text{and} \qquad rdr = pdp\ . \tag{76}$$

For the model, the z interval $(-\sqrt{3}\,R, \sqrt{3}\,R)$ corresponds to a wavelength interval in which the photospheric flux is transmitted without scattering and in which the limb emission at each wavelength is due to an annular area of the corresponding CD velocity surface with inner and outer radii of $2R$ and $5R$, respectively. Thus, for this wavelength interval there is a constant photospheric flux and a constant limb flux that add to give a constant net flux. This constant net flux, of course, forms the flat top on the line emission feature. The small oscillations seen on the flat tops in Figure 6 are an artifact of the numerical integrations. For increasing wavelength redward of the wavelength corresponding to $z = -\sqrt{3}\,R$, the atmospheric flux is increasingly occulted, and thus the emission feature declines toward the continuum flux level. For wavelengths bluer than the wavelength corresponding to $z = \sqrt{3}\,R$, the photospheric flux is being scattered in the detached atmosphere, and hence the usual trough feature is formed. Additionally, for wavelengths bluer than the wavelength corresponding to $z = 2R$, the inner radii of the CD velocity surfaces are equal to their z coordinates rather than equal to $2R$; thus, as z increases for $z > 2$ the flux from the corresponding CD velocity surfaces must decrease.

Detached atmospheres are not likely structures in supernovae. However, hydrodynamic calculations show that density peaks may occur in supernova density profiles. These peaks are formed where the deflagration front stalls in SN Ia calculations (e.g., Nomoto et al. 1984; Jeffery and Sutherland 1985) and due to radioactive acceleration in SN II calculations (Woosley 1988; see also § V*a*). Density peaks should have effects on the spectra that are similar, but much less extreme, than the effects of a detached atmosphere. To investigate the effects of density peaks, a calculation was done with a model that has the usual inverse power law with index 7 for optical depth for the radius interval R to $2R$. However, at $2R$ there is a discontinuous jump to an optical depth equal to the photospheric optical depth. The ratio of optical depth above to optical depth below the jump is approximately 130. Above $2R$, the optical depth decreases again with an inverse power law with index 7 out to the cutoff radius $5R$. The resulting spectra for varied photospheric optical depth are shown in Figure 7. The extra long vertical line segment in Figure 7, marks the wavelength that corresponds to the z location of the optical depth jump. The profiles for the cases with $\tau_{\rm ph} \leq 10$, show features recognizably similar to those seen for the detached-atmosphere model. The flat red shoulders on the emission features and the blueshifted secondary emission maxima are both due to the same effects that give rise to the flat-top emission feature in the detached-atmosphere case. There are also, as in the detached-atmosphere case, trough features with red edges at the wavelengths corresponding to the z location of the optical depth jump. The fact that there is now some opacity between the photosphere and the opacity discontinuity causes the formation of the usual line center emission maximum and photospheric trough.

For the $\tau_{\rm ph} = 100$ case, the detached-atmosphere features are largely suppressed. For the $\tau_{\rm ph} = 10^6$ case, which is effectively an infinite opacity case, the detached-atmosphere features have completely vanished. The disappearance of the detached-atmosphere features is, of course, due to the fact that once the atmosphere has become completely saturated the emergent flux is independent of optical depths and is determined only by the line source function and the unscattered photospheric flux.

The optical depth jump in the model for Figure 7 was rather extreme since the ratio of optical depth above to below the jump was of order 100. In the hydrodynamic calculations cited above, the density peaks were only of order 10 higher than the surrounding density profile. Model calculations with optical depths with opacity jumps of order 10 showed no striking detached atmosphere features. The detached-atmosphere effects were averaged away in the integration over the velocity surfaces. Thus, the effects of density peaks in observed spectra may not be readily apparent. Additionally, in real supernovae, the density peaks predicted by hydrodynamic calculations may not occur. Turbulent mixing that is expected in supernovae (Nomoto et al. 1984; Woosley 1988) is not included in the hydrodynamic calculations that show the density peaks. This turbulent mixing may smooth out the density peaks. Peaks in optical depth can, however, arise from compositional or ionizational variations with radius. It is probably worthwhile to keep in mind the possibility of detached atmosphere effects when analyzing supernova spectra.

An extreme opposite to the detached-atmosphere case is the case where the atmosphere is a geometrically thin shell surrounding the photosphere. To investigate this case a model was used that has an outer cutoff radius of $r_{\rm c} = 1.1R$ and line optical depths τ that were constant with radius. The spectra resulting from calculations with this model are shown in Figure 8. The striking feature of these spectra is the flat bottoms of the line troughs. The small oscillations seen on the flat bottoms are an artifact of the numerical integrations. As with the flat tops of the detached-atmosphere profiles, the flat bottoms are due to the spherical geometry which causes the emergent flux from CD velocity surfaces between $z = \sqrt{r_{\rm c}^2 - R^2} = 0.4583R$ and $z = R$ to be independent of z. The expression for the emergent flux of the flat bottoms is

$$\begin{aligned} F &= \pi I_{\rm ph}\left(2R^2 - r_{\rm c}^2\right) + 2\pi \int_R^{r_{\rm c}} dr\, r\left[I_{\rm ph}e^{-\tau} + S(r)\left(1 - e^{-\tau}\right)\right] \\ &= \pi I_{\rm ph}R^2\left(0.79 + 0.21e^{-\tau}\right) + 2\pi\left(1 - e^{-\tau}\right)\int_R^{r_{\rm c}} dr\, rS(r)\ . \end{aligned} \tag{77}$$

This expression shows that in the saturation limit the flat-bottom flux will approach 0.79 of the continuum flux level, plus an amount due to the line source function contribution. This limiting behavior is displayed in Figure 8. The emission features in Figure 8 are rather narrow because the line-of-sight extent of the limb is only from $z = -0.4583R$ to $z = 0.4583R$. The CD velocity surfaces with $z < -0.4583R$ have no surface area inside the atmosphere that is not occulted, and so only the photospheric flux emerges at the redshifted wavelengths corresponding to these CD velocity surfaces.

Since there is a possibility that some supernovae are aspherical events (see § III), it is interesting to examine the line profiles that result from an aspherical version of the ES model. The line profiles in Figure 9 were calculated using a ES model with oblate axisymmetric ellipsoidal symmetry for both photosphere and atmosphere. Oblate asymmetry was considered because supernova oblateness has a plausible origin in the rotation of the supernova progenitor. For the calculations, the ratio of the symmetry semiaxis to the perpendicular semiaxis, c/a, was varied between 1 (spherically symmetric) and 0.1 (very oblate). The inclination angle of the line of sight to the symmetry axis was set to 57.3° which is the average of random inclination angles. The photospheric velocity for the aspherical models has been defined as the line-of-sight velocity of that part of the photosphere that is nearest the observer. As for most of the calculations in this section, a photospheric velocity of $6000\,{\rm km\,s^{-1}}$ has been used for the aspherical model calculations. From Figure 9, it seen that the line profiles remain P Cygni-like as oblate asymmetry is increased. Even the two most oblate cases have P Cygni profiles, albeit rather distorted ones with troughs extending redward of the line center wavelength. The redshift of the emission maximum that occurs with oblateness is due to the fact that CD velocity surfaces corresponding to the wavelengths near the line center wavelength can intercept some photospheric flux. The inclined oblate geometry causes cresent-shaped areas of the photodisk regions of these CD velocity surfaces to lie outside the excluded region. Only at somewhat redshifted wavelengths can the full photospheric flux emerge without being diminished by scattering in CD velocity surfaces. If the inclination angle were at 0° or 90°, there would clearly be no redshift.

Prolate asymmetry has rather similar effects as oblate asymmetry: there is some distortion of the P Cygni profile and redshifts of the line center occur for oblique inclination angles. A catalogue of line profiles for prolate and oblate axisymmetric ellipsoidal versions of the ES model is given by Jeffery (1988). The conclusion drawn from this catalogue of profiles was that moderate oblate and prolate asymmetries will be hard to detect from spectral analysis. The redshift of the P Cygni emission maxima may indicate asymmetry. However, as mentioned above, redshifts of the emission maxima can also arise in spherically symmetric systems due to non-Sobolev effects in line radiative transfer (see Hamann 1981).

Since supernova spectra generally show overlapping line profiles, some calculations have been done to examine the effects on line formation of interacting lines. Figure 10 shows a series of spectra calculated for a spherically symmetric model with two lines with equal photospheric optical depths of 10. The spectra are displaced from each other by one unit in relative flux for clarity. The wavelength separation (WS) in Ångstroms between the line center wavelengths of the two lines is shown in the figure. For wavelength separation of 500 Å, the lines are essentially independent and for wavelength separation of 250 Å, they are weakly interacting. For wavelength separation of 100 Å, the bluer line's trough minimum lies on and largely suppresses the redder line's emission feature. The dominance of trough features over emission features is a general characteristic of pure scattering P Cygni line blends. For wavelength separation of 75 Å, the two-line nature of the spectrum is still apparent. For wavelength separation of 0 Å, the two lines are exactly overlapping and effectively appear as a single line in the spectrum. In fact in the Sobolev method with pure scattering, two lines with the same line center wavelength give exactly the same behavior as a single line, hereafter called an equivalent single line, with an optical depth equal to the sum of the two lines. This is proven by the following argument. Whether the total optical depth of a resonance region arises from two lines or an equivalent single line, there will be the same amount of energy removed from an incident beam in a resonance region. In an actual calculation, the amount of energy removed by two lines is accounted for separately in some definite order, but that does not change the net amount removed. Because the scattering is isotropic pure scattering, all the energy removed from the beam in either the two-line case or the equivalent single-line case will emerge again isotropically from the resonance region. Thus, the whole resonance region behavior of the two cases is the same. It follows that the emergent line profiles for the two cases will be identical within numerical accuracy.

Figure 11 shows the results of a calculation identical to the calculation for Figure 10, except that the bluer line has a photospheric optical depth of 3. Figure 11 shows that the emission feature of a line can be largely suppressed by the trough of a substantially weaker line.

Figures 10 and 11 demonstrate that a line's trough feature will often be more detectable than its emission feature in a spectrum where there are many overlapping lines. This fact and the fact that photospheric velocity can be estimated from trough features are why trough features have usually been more useful than emission features in the analysis of supernova spectra.

Figure 12 shows the results of a calculation where five equally spaced lines all with photospheric optical depth 10 are converged from a wavelength spacing (WS) of 250 Å to 0 Å. Again the resilience of trough features in cases of line blending is demonstrated. The case with wavelength separation of 50 Å shows that a group of closely spaced lines can yield a profile that seems to be the P Cygni profile of a single line with a rather broad, unusually shaped trough feature. The appearance in supernova spectra of such unusual trough features due to closely spaced lines is possible.

V. ANALYSIS OF SN 1987A PHOTOMETRY AND OPTICAL SPECTRA

In this section, an analysis of SN 1987A photometry and optical spectra is presented. The supernova's epoch is measured in days from 23.316 Feb. 1987 U.T., the time of the neutrino event detected by the IMB and Kamiokande II neutrino detectors (Bionta et al. 1987; Hirata et al. 1987); the neutrino event preceded the discovery of the supernova (Shelton 1987) by one day. The photometric data (first 258 days) used for this analysis is the rather complete and self-consistent set of observations and derived quantities (Menzies et al. 1987; Catchpole et al. 1987, 1988) taken at the South African Astronomical Observatory (SAAO). The optical spectra (first 131 days) used are those taken at the Cerro Tololo Inter-American observatory (CTIO), and reported by Phillips et al. (1988); the spectra were obtained from the SN 1987A database at the National Optical Astronomy Observatories (NOAO) headquarters in Tucson. The photometry and spectrum analysis

assumes spherical symmetry although there is considerable evidence that SN 1987A had some significant asymmetries (see, e.g., Jeffery 1987, 1989; Cropper et al. 1988; Bailey 1988; Karovska et al. 1988, 1989). The spherical symmetry assumption is, of course, greatly simplifying, but is probably entirely adequate for the mostly qualitative level of the accuracy of the present analysis.

This section has been divided into four subsections: photometry analysis, line optical depths and abundances, observed and synthetic spectra, and summary.

a) Photometry Analysis

Derived quantities from the SAAO photometry that are used in this analysis are the bolometric luminosity (Fig. 13) and color temperature (Figs. 14a–14b). To obtain a bolometric luminosity, the SAAO observers considered all nights for which they had a complete set of U to L magnitudes and day 1.5 for which only U to I magnitudes were available. These magnitudes were converted into absolute fluxes assuming an LMC distance modulus of 18.5 and a reddening of $E(B-V) = 0.2$ (i.e., a visual absorption of $A_V = 0.6$) toward the supernova. The fluxes were then fit by a blackbody function in order to obtain color temperature from the fitted function's shape and bolometric luminosity from its integral over wavelength. The accuracy of these derived quantities depends on the accuracy of the assumed distance modulus and $E(B-V)$ values and the accuracy of assuming a blackbody distribution for the emitted flux. Both distance modulus and $E(B-V)$ are somewhat uncertain. Since recent determinations (e.g., Feast 1984; Laney and Stobie 1986; Shobbrook and Visvanathan 1987) indicate an LMC distance modulus of 18.5 ± 0.3 (i.e., a distance of 50 ± 7 kpc), the bolometric luminosity has an uncertainty of order 20 % due to uncertainty in LMC distance; the color temperature is, of course, independent of distance. The $E(B-V)$ value of 0.2 used by the SAAO observers was determined by West et al. (1987) using archival data from the supernova progenitor star, Sanduleak $-69°202$. A more recent determination based on photometry of bright stars close to SN 1987A gives $E(B-V) = 0.17 \pm 0.02$ (Walker and Suntzeff 1990). The uncertainties suggested by the variation in these $E(B-V)$ values can be of order 10 % (see, e.g., Fig. 4 of Menzies et al. 1987). The assumption of a blackbody flux distribution is justified by the smallness of the deviations of the magnitudes, except for U and B, from the fitted blackbody curves for at least the first 134 days (Catchpole et al. 1987).

The scenario for the supernova explosion and the interpretation of the bolometric luminosity and color temperature that are given here largely follow those given by Woosley (1988). Stellar evolution studies and the progenitor star's known luminosity allow estimates of the progenitor's main sequence mass and helium core mass to be made: $19 \pm 3\, M_\odot$ and $6 \pm 1\, M_\odot$, respectively. Prior to the explosion, the helium core consists of an inner core of about $1.5\, M_\odot$ of iron, a layer rich in intermediate mass elements, and an outer layer of about $2\, M_\odot$ that is dominated by helium. Above the helium core is the hydrogen envelope. In the presupernova evolution a theoretically unconstrained amount of hydrogen envelope may have been ejected; the remaining hydrogen envelope could have a mass anywhere between less than $1\, M_\odot$ and the main sequence mass of $\sim 13\, M_\odot$. When the explosion occurs, the iron core collapses to a neutron star and a shock wave propagates out through the star compressing, heating, and accelerating the matter. Essentially all the mass above the original iron core is thrown off into space where uniform motion homologous expansion is quickly established (see § III). Of the innermost ejecta, of order one solar mass is subjected to explosive nuclear synthesis. The high temperatures that result from the shock heating cause the supernova to radiate a large emergent luminosity with a distribution that peaks in the ultraviolet. The internal energy (i.e., thermal energy) is, however, small compared to the kinetic energy deposited by the shock. As the ejecta expands, adiabatic cooling converts most of the initial internal energy into kinetic energy and causes the ejecta's temperature to fall. The supernova's photosphere is growing in radius just due to the expansion of the ejecta, but in mass coordinate the photosphere is receding due to the falling temperature and opacity. The opacity that is due to electrons decreases greatly when hydrogen recombines. Thus, the photospheric radius will tend to stay smaller than the hydrogen recombination radius (i.e., the radius outside of which the hydrogen is mostly neutral) as the hydrogen recombination radius recedes into the ejecta and the photospheric temperature will, after the early hot phase, tend to be fixed at about the hydrogen recombination temperature (~ 5500 K). In NLTE calculations the hydrogen recombination radius is found to be larger than the photospheric radius by 20–50 % (Höflich 1988). Figures 14a–14b show that the color temperature is of the order of the hydrogen recombination temperature from about day 15 to about day 90.

During the first few hours after the neutrino burst, the supernova luminosity reaches an initial and

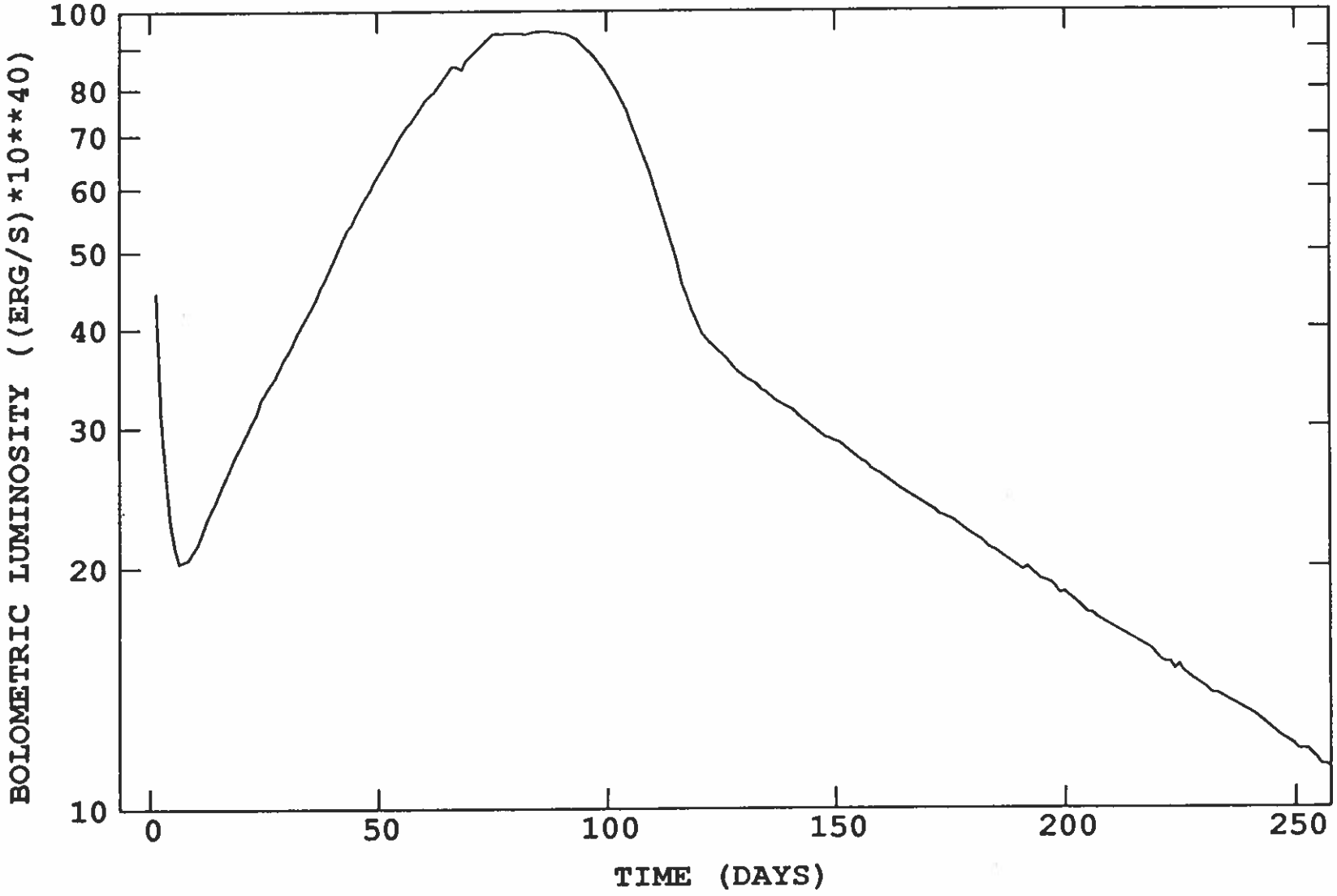

Fig. 13: *SAAO SN 1987A bolometric luminosity for days* 1.50–257.65.

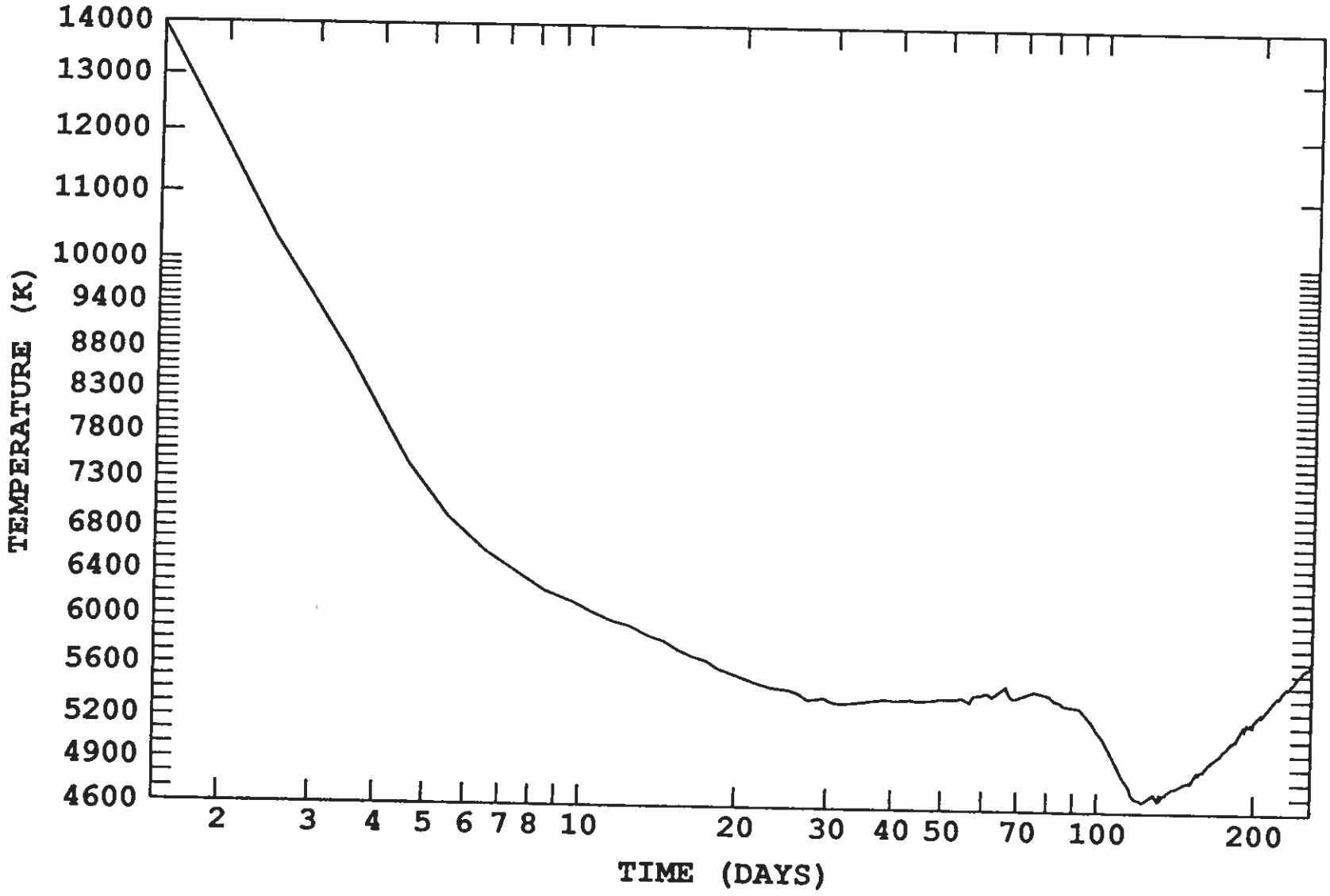

Fig. 14a: *SAAO SN 1987A color temperature for days* 1.50–257.65.

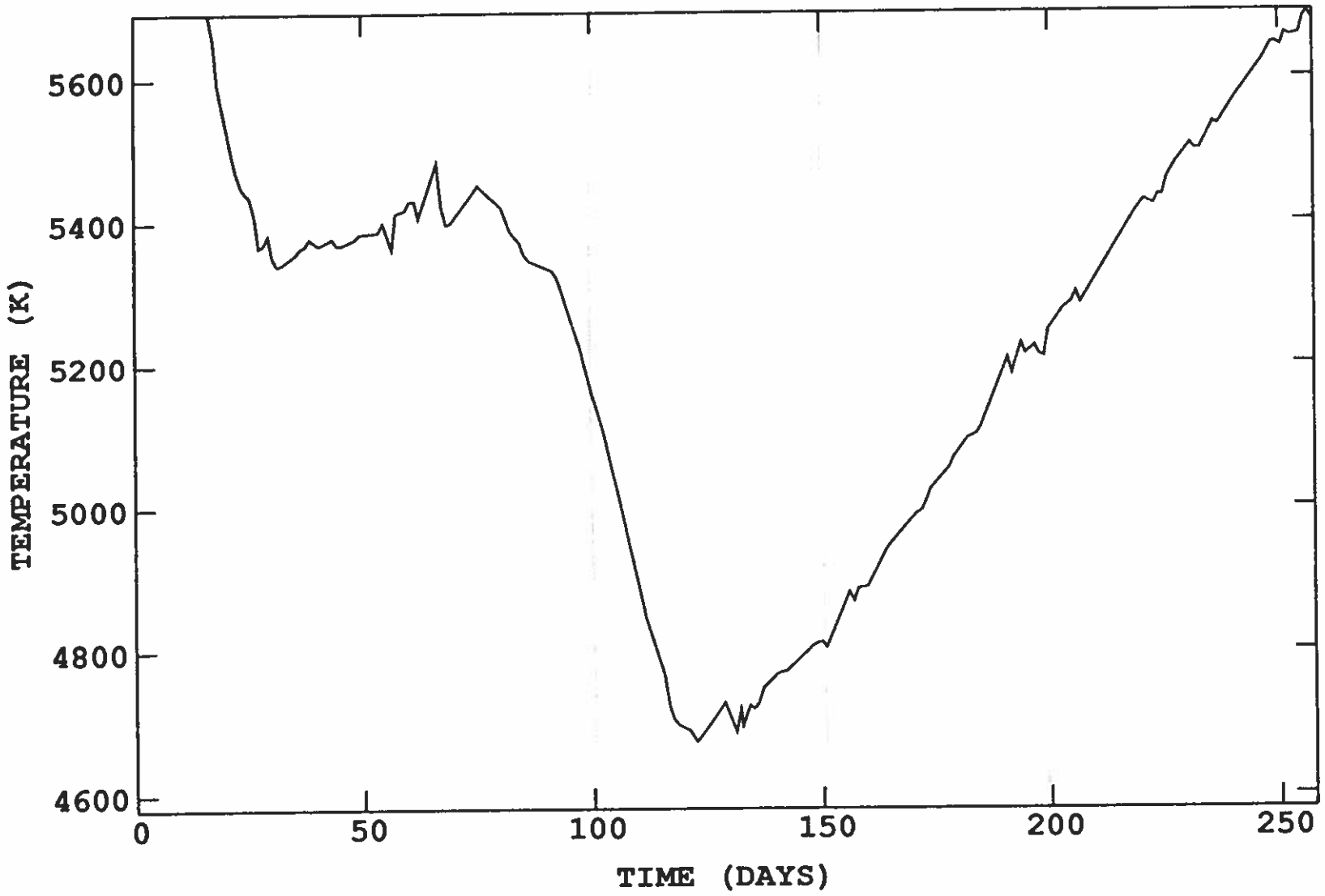

Fig. 14b: *SAAO SN 1987A color temperature for days* 16.45–257.65.

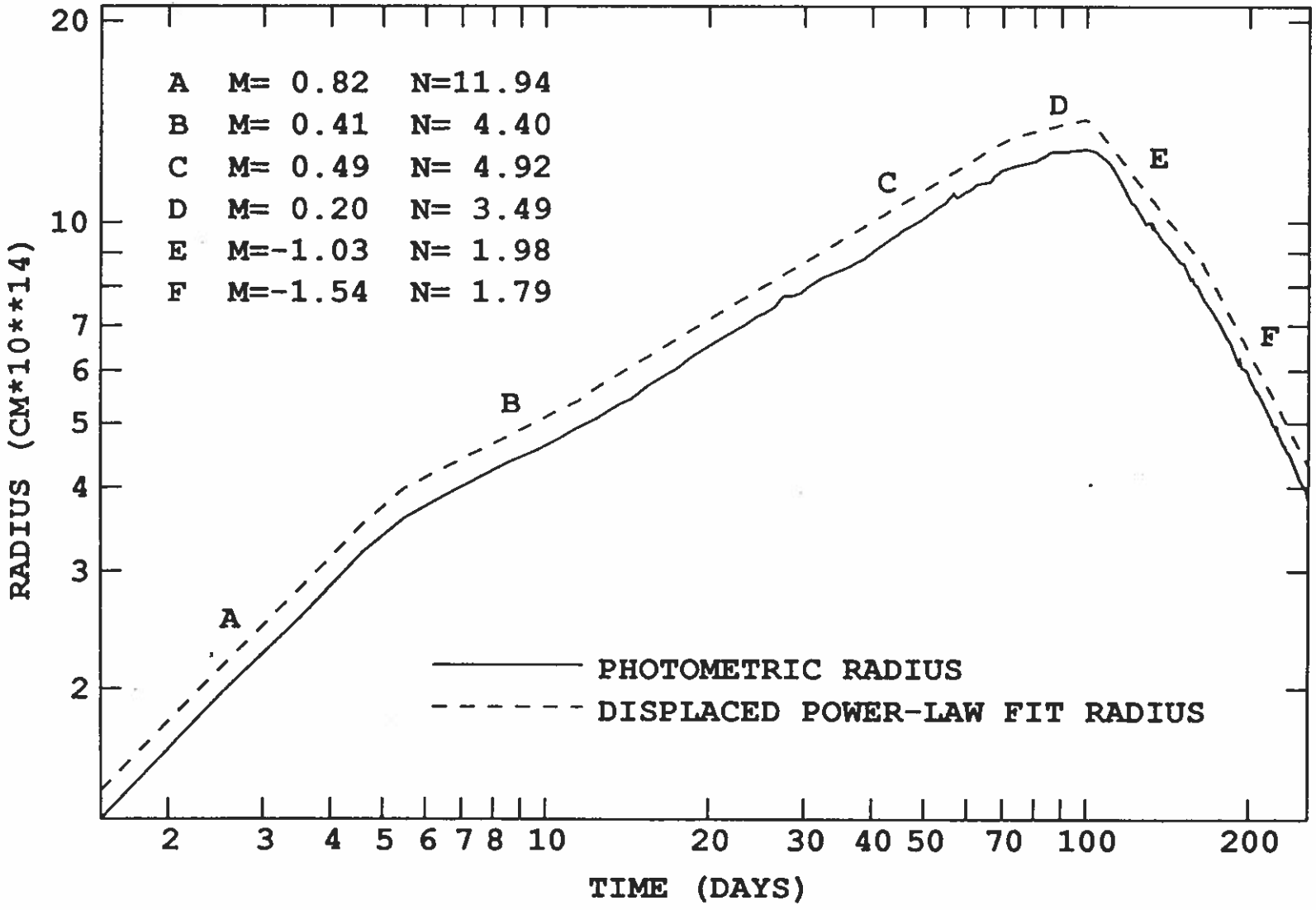

Fig. 15: *SAAO SN 1987A photometric radius and a displaced power-law fit radius for days* 1.50–257.65.

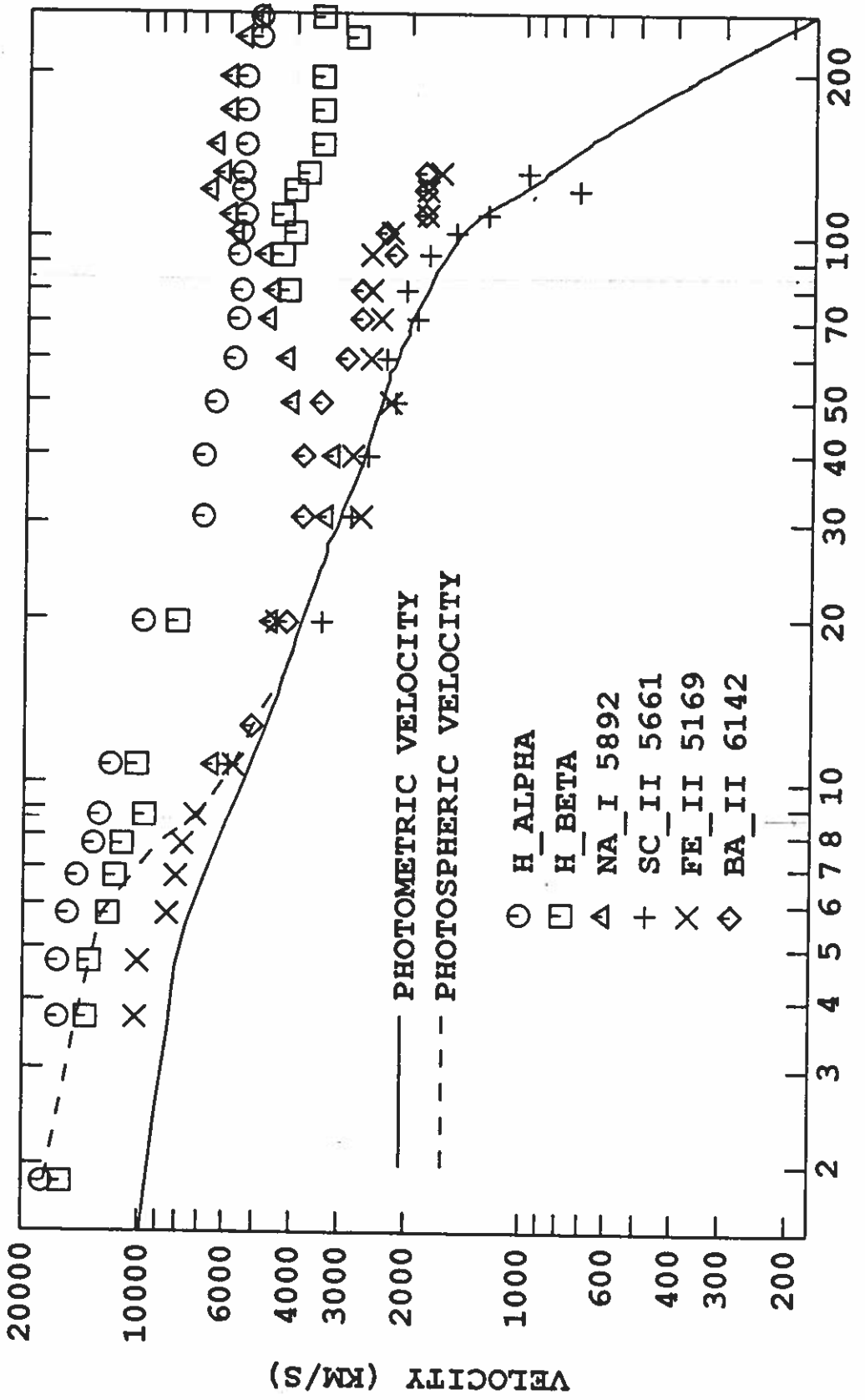

Fig. 16: *SAAO SN 1987A photometric velocity for days* 1.50–257.65, *spectrum-fitted photospheric velocity for days* 1.85–131.07 *(merges with the photometric velocity after day 16), and various line velocities.*

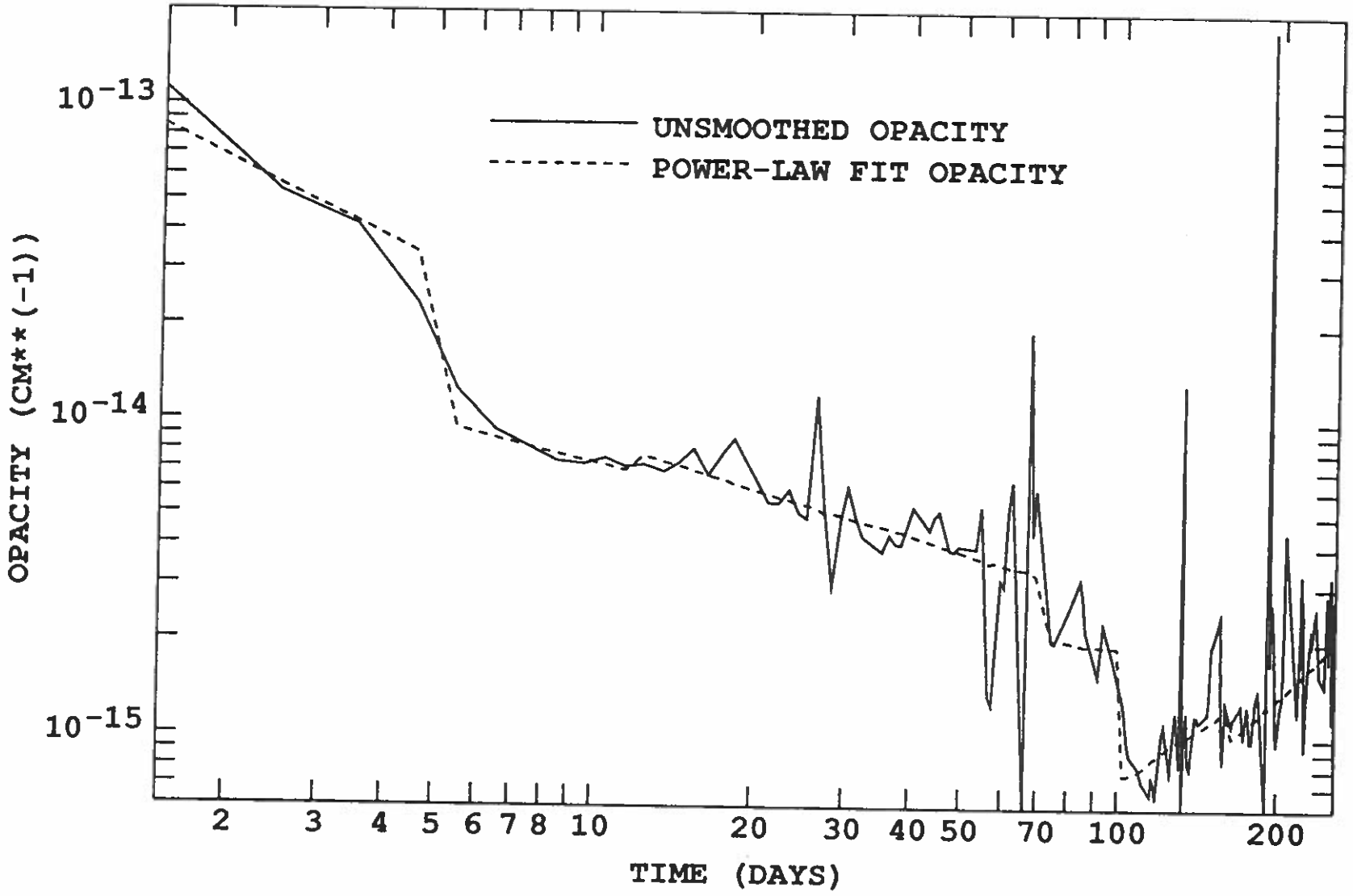

Fig. 17: *Empirical opacity evolution for SN 1987A for days* 1.50–257.65.

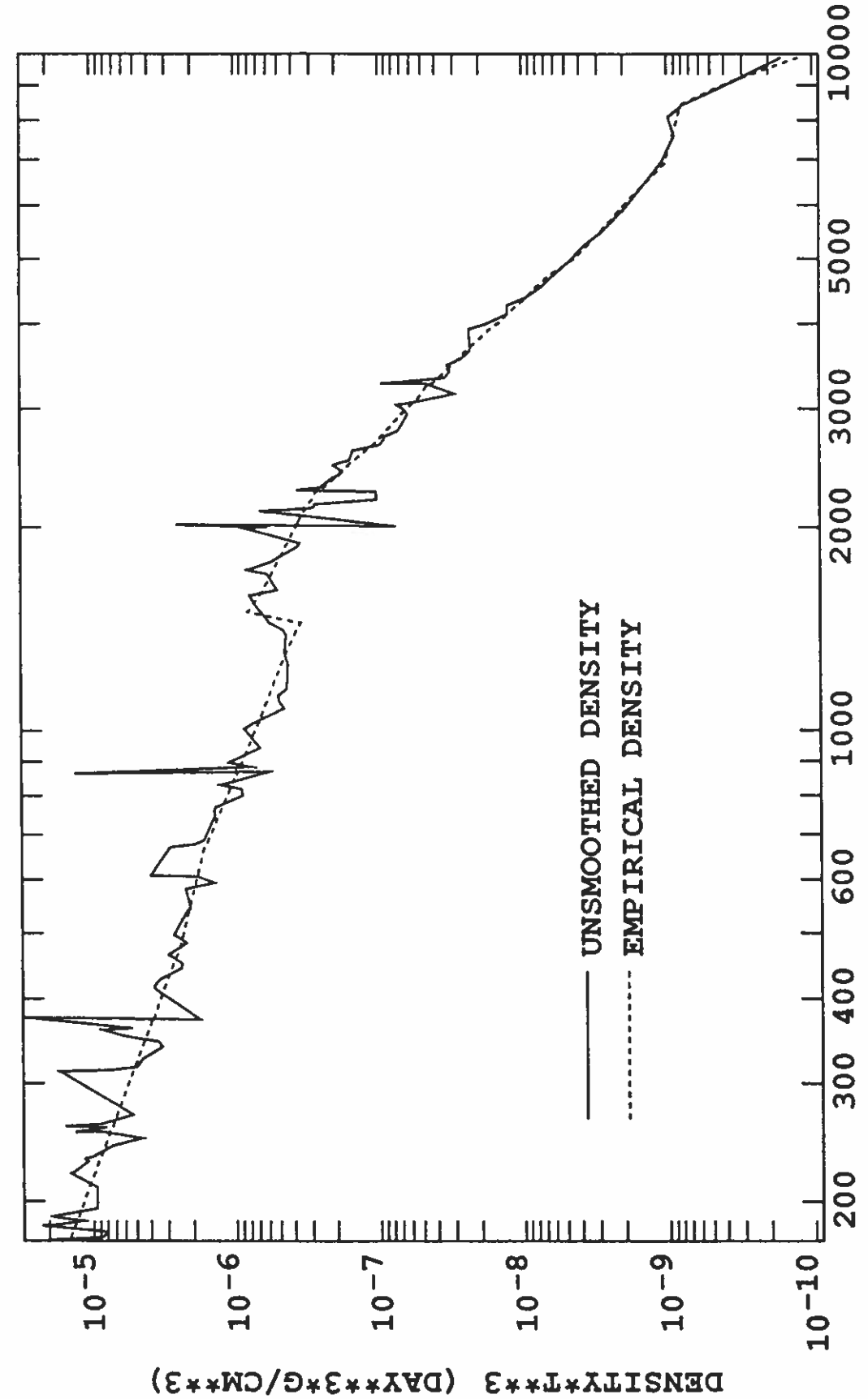

Fig. 18a: *Unsmoothed and smoothed empirical density profiles for SN 1987A.*

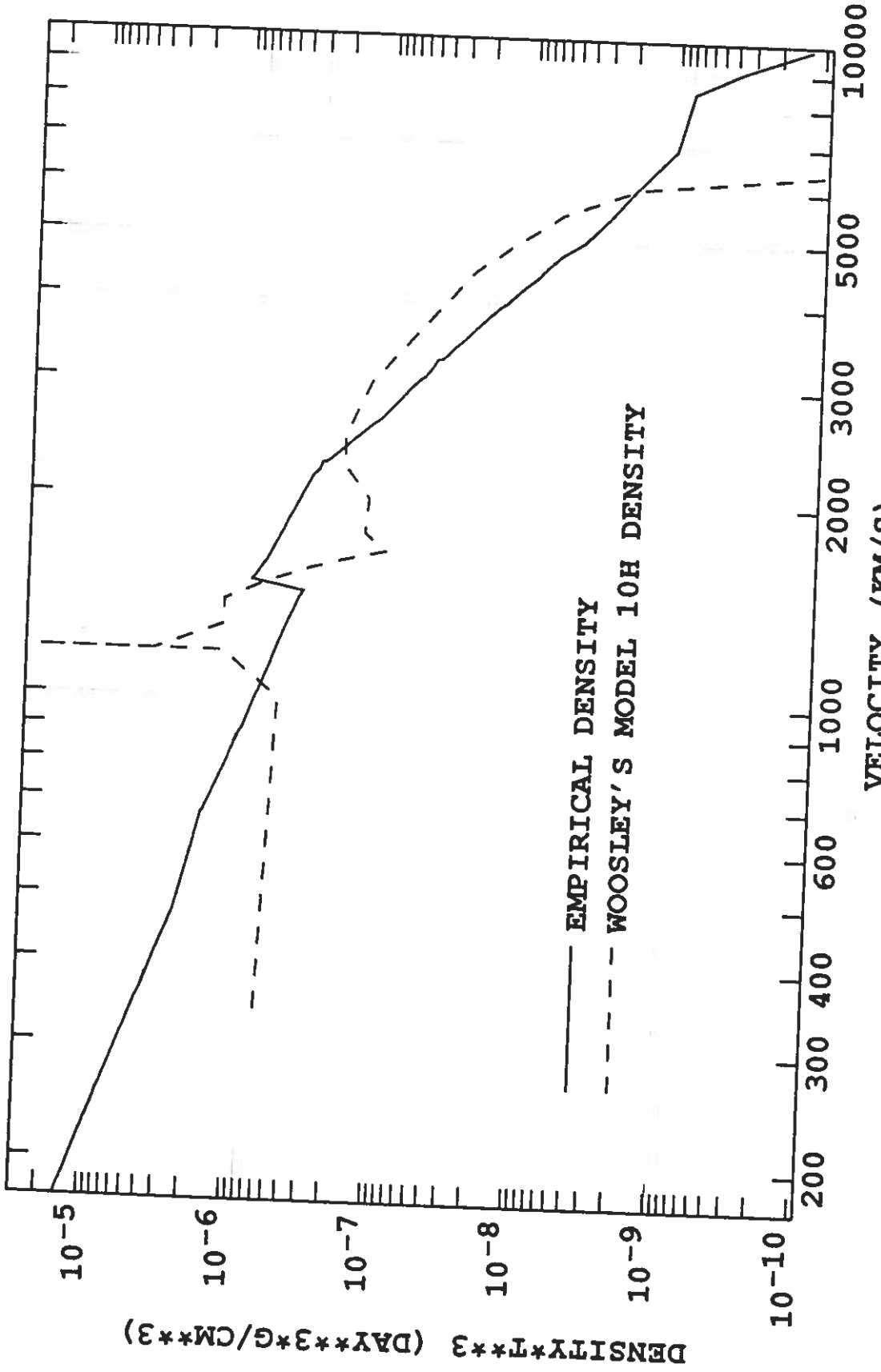

Fig. 18b: *The empirical density profile for SN 1987A and a smoothed version of Woosley's model 10H density profile.*

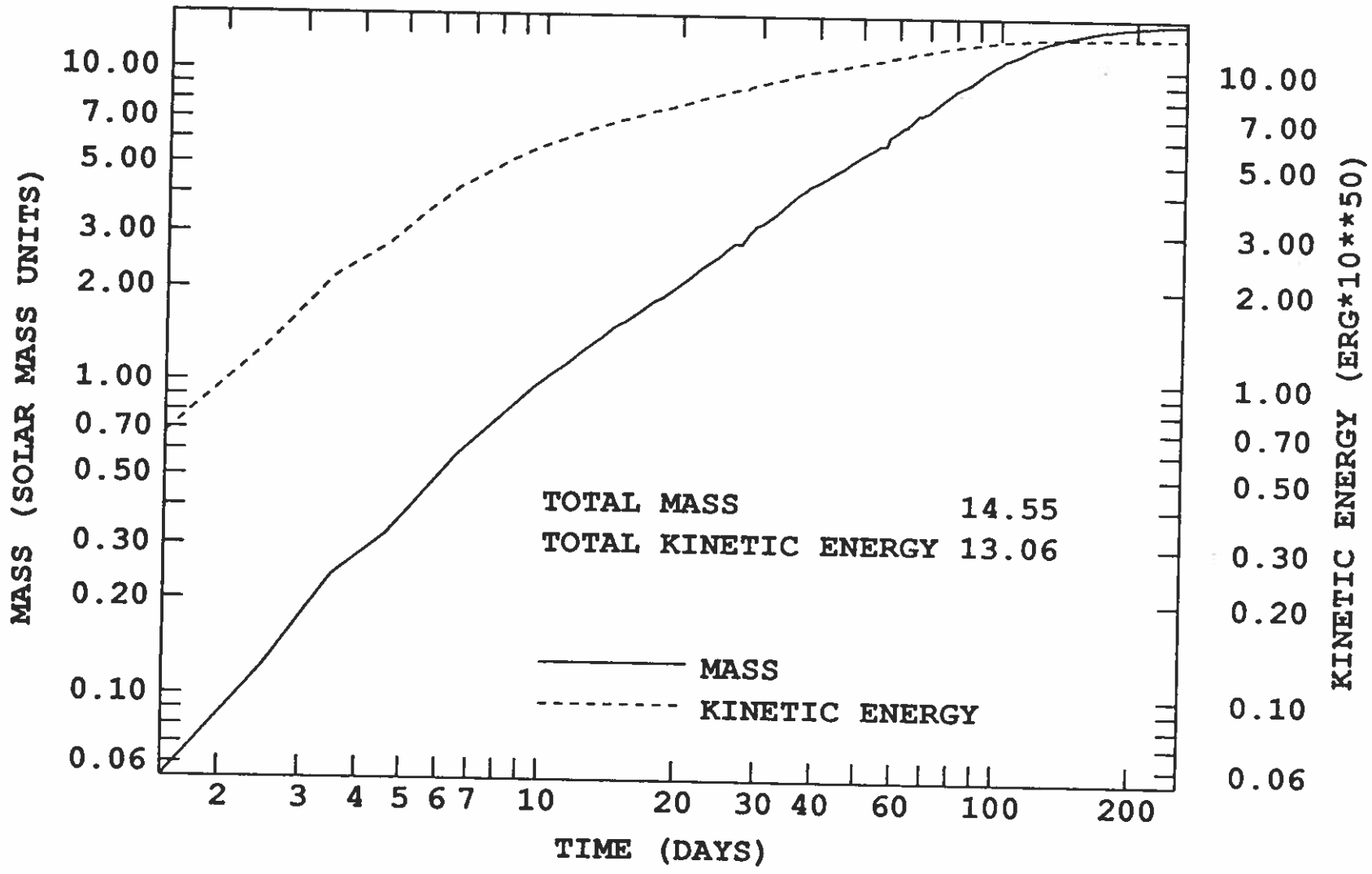

Fig. 19: *Derived SN 1987A photospheric outflow mass and photospheric outflow kinetic energy (i.e., mass and kinetic energy that have flowed out through the photosphere) plotted as functions of time since the explosion.*

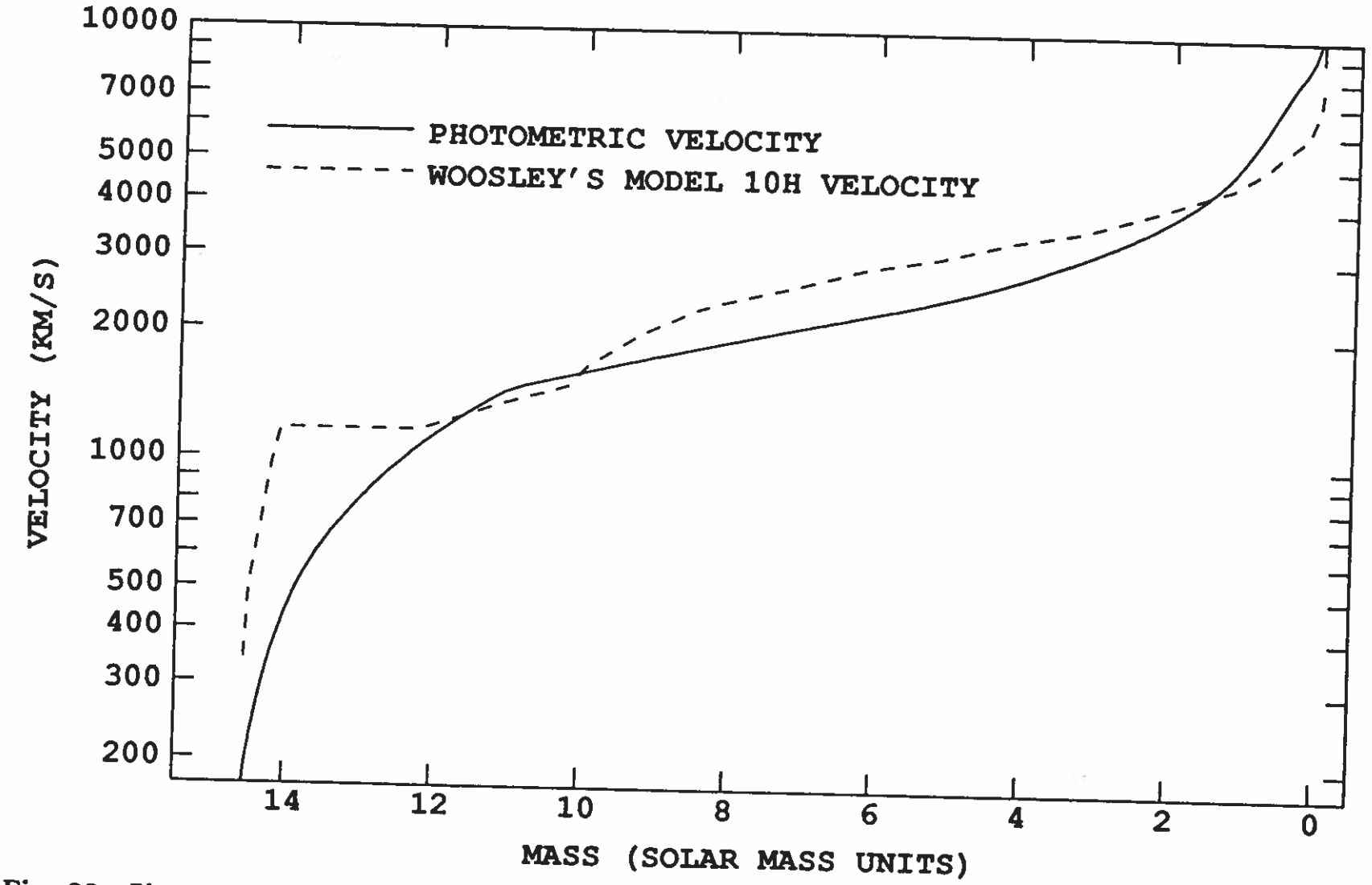

Fig. 20: *Photometric velocity and model 10H velocity plotted versus mass coordinate where mass is measured inward from the surface. The mass coordinate for the photometric velocity curve is just the derived photospheric outflow mass.*

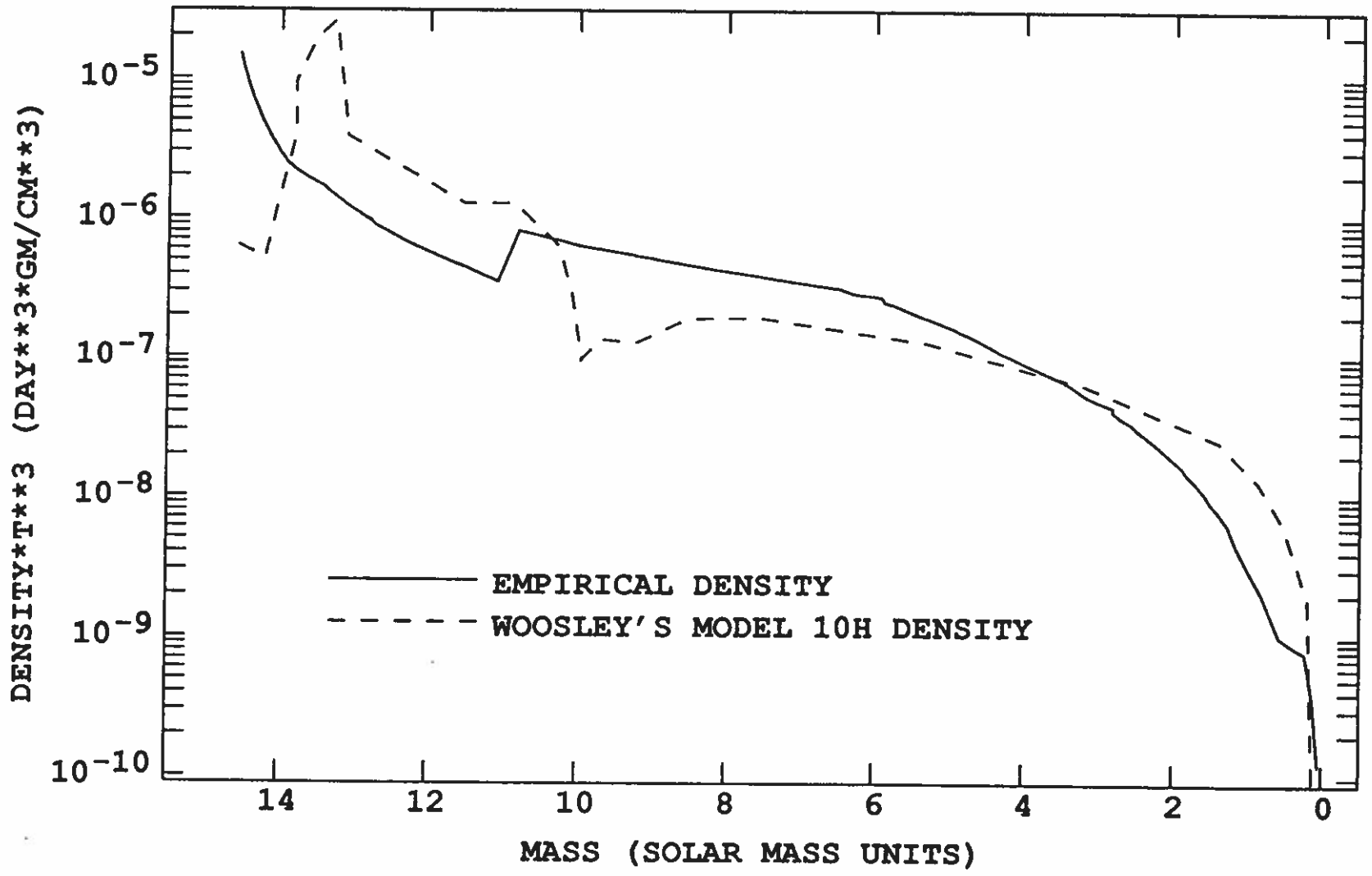

Fig. 21: *The empirical and smoothed model 10H density profiles plotted as functions of mass coordinate where mass is measured inward from the surface. The mass coordinate for the empirical density profile curve is just the derived photospheric outflow mass.*

unobserved maximum and then begins a rapid decline due to adiabatic cooling which temporarily more than cancels the effect of the outward diffusion of the shock-wave-produced internal energy. When the SAAO observations begin at day 1.5, the supernova luminosity is in this rapid decline phase. Most of the luminosity is still in the ultraviolet, and thus the color temperature, which is certainly of the order of the true photospheric temperature, is 14000 K. At about day 7.5, the luminosity reaches a minimum and then begins a slow rise. Initially, this resurgence is probably due to faster diffusion of the shock-wave-produced internal energy (see Figs. 11 and 16 of Woosley 1988). This shock-wave-produced internal energy exhausts in a few tens of days, but the rise in the luminosity continues. This continuance is a consequence of the reheating of the ejecta by the decays ^{56}Ni $\rightarrow^{56}$ Co and ^{56}Co $\rightarrow^{56}$ Fe: the decay half-lifes are 6.10 and 77.12 days, respectively (Huo et al. 1987); the decay energies, not counting the energy released in neutrinos which has no observable effect, are 2.96×10^{16} ergs g^{-1} and 6.41×10^{16} ergs g^{-1}, respectively (Woosley 1988). The initial radioactive ^{56}Ni is a product of nuclear burning during the explosion.

The radioactive decay energy does not contribute to the luminosity at early times because the radioactive elements are formed at the base of the ejecta and the diffusion time is longer then than the time since the explosion. Eventually, however, owing to the combination of receding photosphere and diffusion from the base of the ejecta, there is an increasingly fast release of the built-up store of radioactive decay energy. This energy takes over the powering of the luminosity from the exhausting shock-wave-produced internal energy. The faster the release of the decay energy, the higher the luminosity grows until the built-up store starts to become exhausted and then the luminosity falls. The time of the luminosity maximum (i.e., the second but now observed luminosity maximum) or maximum light is about day 85. The relatively rapid fall of the luminosity starts to slow about day 120 and becomes very closely an exponential decline by day 130. The half-life of this decline as determined by the SAAO observers is within 2 % of the ^{56}Co half-life. The observation of this exponential decay is conclusive evidence that radioactive decay powers the post-early-time luminosity. Furthermore, from their absolute luminosity determination, the SAAO observers find that the amount of ^{56}Ni ejected in the explosion is $0.078\,M_\odot$ with an uncertainty of at least 15 % (Catchpole et al. 1988).

Using their bolometric luminosity and color temperature and the formula for a spherical blackbody radiator (see eq. [49] in § III), the SAAO observers define a photometric radius:

$$r_{\rm pho} = \sqrt{\frac{L_{\rm bol}}{4\pi\sigma_S}}\,\frac{1}{T_{\rm col}^2}\ . \tag{78}$$

The SAAO photometric radius is plotted in Figure 15. If the color temperature were the photospheric effective temperature, then $r_{\rm pho}$ would be exactly the photospheric radius R. However, as argued in § III, the color temperature can be either higher or lower than the photospheric effective temperature and so $r_{\rm pho}$ can be either smaller or larger than R. As can be seen from Figure 15, the evolution of the photometric radius with time can be divided into epochs where R varies rather nearly as a power of time. For the purpose of fitting power laws to the photometric radius evolution, six epochs, here labeled A through F, were chosen. The power indices m for these epochs are displayed in the table in Figure 15. Actually, only three epochs are clearly physically justifiable; roughly these are days 1.5–5.5, days 5.5–100, and after day 100. These three epochs correspond roughly to the luminosity phases of initial decline, rise to maximum light, and post-maximum-light decline. If it is assumed that the photometric radius is the photospheric radius and that opacity per unit density is a constant, then for each epoch the ejecta density approximately obeys an inverse power law of radius (see § III). For the six fitting epochs, the indices n for the inverse power-law density profile segments are shown in the table in Figure 15. For the three physical epochs the indices n are approximately 12, 4.5 and 2.

A point that must be stressed in interpreting the color temperature and photometric radius is that by day 140 the supernova is clearly passing into the nebular phase (Catchpole et al. 1988). In the nebular phase, much of the energy from the radioactive decay emerges from the supernova as line emission and is never in the form of true TE internal energy. This line emission must, of course, come from above the photosphere. The nebular emission becomes very significant by day 250, and so it clear by this time that the color temperature and photometric radius have probably lost any simple relation to photospheric temperature and radius. At some point in the supernova evolution the photosphere will vanish when the continuum absorption opacity optical depth to the center of the ejecta has fallen to of order 1.

Dividing the photometric radius by the time since explosion gives a photometric velocity. If the photometric radius were the true photospheric radius, then, recalling equation (44) (see § III), the photometric velocity would be the photospheric velocity. The photometric velocity can be compared to a photospheric velocity obtained by fitting synthetic spectra to the observed spectra. Figure 16 shows the SAAO photometric velocity and a spectrum-fitted photospheric velocity obtained using the ES model; the two velocity curves merge at about day 16 where the velocity is about $4200\,\mathrm{km\,s^{-1}}$ and the photospheric velocity curve extends only to day 131. The accuracy of ES model photospheric velocity is, of course, limited by all the limitations of the ES model that are discussed in § III. Also plotted in Figure 16 are the line velocities (i.e., the velocities corresponding to the wavelength shifts of the P Cygni trough minima from the line center wavelengths) for some of the more interesting lines. Since the radial velocity (i.e., in this context, line-of-sight center of mass velocity) of SN 1987A gives a constant Doppler shift to the entire spectrum, a correction should be applied to get intrinsic velocities. However, the radial velocity of progenitor star is not known and so the LMC radial velocity of $270\,\mathrm{km\,s^{-1}}$ (Allen 1973, p. 287) was used to correct the line velocities and to give a global redshift to the synthetic spectra used in determining the photospheric velocities. The LMC radial velocity is little different from an average radial velocity of $265\,\mathrm{km\,s^{-1}}$ given by Elliot et al. (1977) for the 30 Dor region of the LMC where SN 1987A is located.

To obtain a photospheric velocity for a given day, the photometric velocity for that day was taken as the initial value of the photospheric velocity parameter and then this parameter was adjusted in order to get a reasonable fit of a synthetic spectrum to that day's observed spectrum. In judging the quality of the fit more weight was given to the metal lines than to the hydrogen Balmer lines: the hydrogen lines are either strong (Hα and Hβ) and so do not have trough minima that closely track the photosphere (see § IV) or are often strongly blended (Hβ and higher order Balmer lines) and so are not individually discernable (see § V*c* and Figs. 24–36); also the hydrogen lines are not well handled by the ES model (see § III). The uncertainty in the spectrum-fitted photospheric velocities, due to difficulty in judging the quality of the fits, is of order $1000\,\mathrm{km\,s^{-1}}$ up to about day 10 and of order $500\,\mathrm{km\,s^{-1}}$ thereafter; these uncertainty estimates do not include uncertainties due to the ES model assumptions. For the first CTIO spectrum (day 1.85; see Fig. 24), it is necessary to rely almost entirely on hydrogen lines for fitting a photospheric velocity; however, the weaker hydrogen Balmer lines, which may be expected to more closely track the photosphere than the stronger hydrogen Balmer lines, were fairly distinct. By day 3.71, there is already the K (3934 Å) and H (3968 Å) Ca II line blend to use for fitting in addition to the hydrogen lines (see Fig. 25). The observed spectrum features on this day that are identified as due to Fe II lines were too poorly reproduced in the synthetic spectrum to help in fitting the photospheric velocity. After day 3.71, Fe II and other metal lines appearing in the spectra (see Figs. 26–36) could be utilized in the fitting procedure. Thus, the discrepancy between the photometric and spectrum-fitted photospheric velocities for the period up to day 16 is probably real. After about day 100, the relative uncertainty in the spectrum-fitted photospheric velocity becomes large. Therefore, the most that can be safely concluded is that the photometric velocity and radius are probably close to the true photospheric velocity and radius from about day 16 to about day 100.

Since there is no *a priori* reason that the combined action of the flux reduction and atmospheric emission effects (see § III) will cause agreement between the photometric and photospheric radii, the initial phase where photometric radius is smaller than photospheric radius is understandable. It is the relatively long phase of agreement between the photometric and photospheric radii that is remarkable. However, no certain explanation has been thought of for this agreement. Nevertheless, it is easy to understand that the atmospheric emission effect should increase in strength in time and that this should cause the photometric and photospheric radii to come into closer agreement. As the photosphere recedes into the ejecta, the ejecta density gradient becomes less steep (see below), and this causes increasing atmospheric extension and thus increasing atmospheric emission (see § III). With more atmospheric emission, the color temperature is reduced and the photometric radius is larger.

An important point to make at the outset in interpreting the line velocities displayed in Figure 16 is that all the P Cygni line profiles were to some degree formed by line blending. The TE analysis of the spectra described in §§ V*b* and V*c* showed that this line blending was often quite significant. The Hα line because of its strength is certainly the line least affected by such blending. The line identifications shown in the table in Figure 16, except in the case of the Ba II λ6142 line (see § V*b*), were made according to solar-composition TE predictions (see § V*b*) of the strongest line contributing to an appropriately located P Cygni trough. Due to line blending, no single line can be used as an exact tracer of the photosphere; the Hα line is too strong to

closely track the photosphere and since the Hα line is obviously not a pure scattering line, it is not suitable for ES model interpretation (see § III). The ambiguity that line blending causes in the interpretation of line velocities makes it better, in principle, to determine photospheric velocity from synthetic spectrum fitting since line blending is included in the spectrum calculation. Line velocities can, however, be examined for interesting behaviors.

In Figure 16, the line velocities behave for the most part as expected. Except for the Na I λ5892 doublet velocity, all the line velocities are roughly declining with time: this is the expected tracking of the photosphere. The Hα and Hβ lines because of their strength (see Figs. 24–36) are much faster than the metal lines. The re-acceleration of the Na I λ5892 doublet velocity is anomalous. The Na I λ5892 doublet is always stronger and thus faster in the observed spectra than the TE-predicted behavior discussed in § V*b*. Thus, NLTE effects may explain the doublet's strength and re-acceleration. Another possibility is that the Na I λ5892 doublet is strongly contaminated by the He I λ5876 line. In TE with solar abundances, the He I λ5876 line would be insignificantly weak. However, an infrared P Cygni line that grows from being a relatively weak feature on day 76 to being a rather strong one on day 135 has been identified as the He I λ10830 line (Elias et al. 1988); this line should also not appear according to solar-composition TE predictions. Since the upper level of the He I λ10830 line is the lower level of the He I λ5876 line, it is possible that the He I λ5876 line is also important in the spectra. The appearance of the He I λ10830 line has been attributed by Graham (1988) to radioactive ionization of He I followed by recombination which populates the metastable lower level of the He I λ10830 line. The radioactive ionization is due to γ-rays from the ^{56}Co. Since these γ-rays leak out to the outer layers only after the density has fallen sufficiently, the He I λ10830 line appears and grows strong only after some delay. Graham finds that the excitation caused in this way will decline significantly more slowly than density with radius. Such a slowly declining excitation would account for the rather broad profile of the He I λ10830 line on day 135 line: the line velocity is about 4500 km s^{-1} and the velocity of the blue edge of the profile is about 8000 km s^{-1}. These velocities are high relative to the line and blue-edge velocities of line profiles confidently attributed to metal lines near day 135. If the line trough feature centered about 5775 Å on day 131 which is identified as due to Na I λ5892 (see Fig. 36) is interpreted as due to He I λ5876, then the line and blue-edge velocities are about 5500 km s^{-1} and 7700 km s^{-1}, respectively. The first velocity is not very consistent and the second is roughly consistent with the corresponding values for the He I λ10830 line. This mixed result does not suggest a strong conclusion. However, if the He I λ5876 line is indeed significant, then the high velocity of the trough associated with the Na I λ5892 doublet is understandable.

To investigate the relative strengths of the He I $\lambda\lambda$5876 and 10830 lines, one can assume the TE relation given by equation (66). With this relation and a temperature of 5000 K, the ratio of the 5876 Å line's optical depth to the 10830 Å line's optical depth is ~ 0.1. As was discussed in § IV, the size of line profile features of strong lines have a weaker than linear variation with optical depth (see eqs. [72] and [74]). Thus, it is possible even if the 5876 Å line's optical depth is a factor of ten weaker than the 10830 Å line's optical depth, that the 5876 Å line profile would still be comparatively strong. Of course, the TE relative strength result is only suggestive since the helium would be in a NLTE state if Graham's hypothesis is correct. In all subsequent discussion of the P Cygni line attributed to the Na I λ5892 doublet, the possibility of significant He I λ5876 contribution will be kept in mind.

Two other points should be made about the line velocities. The first is that although the Sc II λ5661 multiplet appears to roughly track the photometric velocity in the day 100 to day 131 epoch this cannot be considered a confirmation that the photometric velocity is the true photospheric velocity in this epoch. The individual lines of the Sc II λ5661 multiplet are spread over about 40 Å (see Table 1 in § V*b* for the line data for the 6 Sc II λ5661 multiplet lines) and the wavelength shift given by a velocity of 1000 km s^{-1} near 6000 Å is about only about 20 Å. Clearly, the multiplet line features must be considered as the result of line blending rather than as the line profile due to a single line for such low velocities, and thus the multiplet's line velocity cannot be interpreted in a simple fashion. Moreover, there are Na I lines near the longest wavelength line of the multiplet (see Table 1 in § V*b*) that may contribute significantly in the post-day-100 epoch. This ambiguity in interpreting the Sc II λ5661 multiplet's line velocity is a concrete example of the previously discussed difficulty in extracting photospheric velocities from line velocities. The second point is that the Hβ line velocities are not shown for the day 20 to day 80 epoch. In this epoch, the Hβ trough minimum is not clearly identifiable. From solar-composition TE predictions (see § V*b*), one would expect the Hβ trough minimum to be clearly identifiable despite heavy line blending. The distortion of the Hβ line

profile is probably a consequence of the Bochum event. A discussion of the Bochum event is included in the discusion given in § Vc of Figure 30.

Figures 17 through 21 show the results of a very simple-minded analysis done to extract an empirical density profile from the photometric data. Assumed are uniform motion homologous expansion throughout the ejecta and constant opacity per unit mass. The latter assumption is sweeping since it ignores all varying wavelength, TE, NLTE, expansion opacity, and composition effects. The photospheric radii used for this analysis are just the SAAO photometric radii. No use is made of the spectrum-fitted photospheric velocities to determine photospheric radii for the period up to day 16. The reason for this is that the rather steep decline of the photospheric velocity in the days 6–9 epoch would lead to a plateau region in the density profile of the outer ejecta. Theoretical studies give no evidence for such a plateau and there was no reason in the spectrum fitting process to invoke effects that a plateau would lead to. The plateau is probably a consequence of the failure of the assumption of constant opacity per unit mass. Thus, eliminating the plateau by ignoring the spectrum-fitted photospheric velocity is a straightforward but rough attempt to correct for the probable failure of this assumption. As mentioned above, the photometric radii from about day 140 to day 258 have less direct physical significance than the radii at earlier times. Since all the radius values are treated as if they had equal significance, another simplifying assumption has been made. With the already specified assumptions, a relative density profile can be obtained; to get an absolute density profile a value of 425 was chosen for the ratio of photospheric continuum optical depth to opacity per unit mass, $\tau_{\rm con}/\chi$. This value was chosen such that the ejecta mass derived from the empirical density profile (see below) would be $14.55\,M_\odot$ which is the ejecta mass of Woosley's rather successful model 10H (Woosley 1988). Model 10H has a hydrogen envelope of $10\,M_\odot$ and a helium core of $6.2\,M_\odot$; only $4.55\,M_\odot$ of the helium core is ejected. The total kinetic energy of the model is 14×10^{50} ergs. With the fit to the model 10H ejecta mass, an absolute comparison between the empirical density profile and the model 10H density profile can be made. If one assumes the photospheric continuum optical depth is exactly 1, then opacity per unit mass would be 0.00235; this assumption does not need to be made to obtain density values.

Figure 17 shows the evolution of opacity (the unsmoothed opacity) that is obtained using $\tau_{\rm con} = 1$ and equation (58) with both sides multiplied by χ, the opacity per unit mass. The derivative in equation (58) was evaluated numerically. Since a difference of quantities that were nearly equal within the uncertainty had to be taken to evaluate the derivative, there is a lot of noise in the resulting opacity evolution. Therefore, the n values from the inverse power-law fits to the photometric radii (see Fig. 15) were used along with equation (60) to obtain a smoothed inverse power-law fit opacity evolution. Because of the assumptions made, the behavior of the opacity evolution correlates strongly with the behavior of the photometric radius evolution.

To get a time-independent density profile, the photospheric density value given by equation (58) for a time t since the explosion is multiplied by t^3 in order to obtain a time-independent ρt^3 quantity which is plotted versus the photometric velocity $v(t)$. The curve formed by the collection of all $\left[v(t), \rho t^3\right]$ points is a uniform motion homologous expansion epoch density profile from which the actual run of densities with velocity at any time in the uniform motion homologous expansion epoch can be obtained by dividing by t^3. Figure 18a shows the density profile obtained in this way using the photometric data and a smoothed version of this profile. The smoothed density profile is here called the empirical density profile and it this empirical density profile that is used in the rest of this analysis and in the synthetic spectrum calculations reported in § Vc. The step-like increase in the empirical density profile at about $1500\,{\rm km\,s^{-1}}$ was not smoothed away since this feature seems to be above the noise in the unsmoothed density profile.

Figure 18b shows the empirical density profile and a somewhat smoothed version of the model 10H density profile; the model 10H densities are, of course, plotted versus the model 10H velocities. The local minimum at about $1700\,{\rm km\,s^{-1}}$ in the model 10H density profile is located near the boundary between the helium core and the hydrogen envelope. Since the pre-explosion model 10H density plotted versus mass had a near-vertical decrease in density at this envelope-core boundary, this local minimum in the model 10H density profile is strongly correlated with the pre-explosion model properties. The steepening density gradient in the outer region of the model 10H density profile is a feature retained from the pre-explosion model. The density spike near $1200\,{\rm km\,s^{-1}}$ and local minimum in density at about $1000\,{\rm km\,s^{-1}}$ are results of a radioactive acceleration. The radioactive heating of the inner ejecta due to the ^{56}Ni and ^{56}Co decays causes an expansion and lowering of the density in the inner ejecta. The expansion accelerates the overlying mass layer to a nearly constant velocity. A mass layer with constant velocity appears as a density spike in a density

versus velocity plot. It must be remarked that both the radioactive acceleration and the original explosion are probably turbulent events with considerable convective mixing (Woosley 1988; Benz and Thielemann 1990). Model 10H resulted from a one-dimensional calculation without convective mixing; it may be that the model 10H density profile features would be smoothed by such mixing. The fact that the empirical density profile seems somewhat smoothed out in comparison to the model 10H density profile might be partially a consequence convective mixing in the real explosion. The step-like feature in the empirical density profile may correspond to either the spike or local minimum near the envelope-core boundary in the model 10H profile. Little significance can be attached to the distinction between the the empirical and model 10H density profiles for velocities lower than $1000\,\mathrm{km\,s^{-1}}$ since the empirical density profile is particularly uncertain there. The empirical density profile has matter moving at higher velocities than in model 10H. The outer mass zoning in model 10H is probably too crude to show the high velocities that thin outer mass layers can display: e.g., $20000\,\mathrm{km\,s^{-1}}$ for the outermost $10^{-3}\,M_\odot$ of the supernova model 15B of Woosley, Pinto, and Ensman (1988, Fig. 6). The empirical density profile, however, implies (see below and Fig. 20) a higher average velocity of roughly the outermost $1\,M_\odot$ than does the model 10H density profile. Since the model 10H outer mass zoning is finer than $1\,M_\odot$, there is perhaps a significant discrepancy between the empirical and the model 10H density profiles for the outer ejecta. However, allowing for all the uncertainties, the overall conclusion can be made that the empirical and model 10H density profiles are not inconsistent with each other.

Figure 19 shows the photospheric outflow mass and photospheric outflow kinetic energy (i.e, the mass and kinetic energy that have flowed out through the photosphere) as functions of time. Using the photometric data and the empirical density profile, these photospheric outflow quantities were evaluated from

$$M\left(t_k\right) = \sum_{l=2}^{k} 4\pi \left[\rho R^2 \left(v - \dot{R}\right)\right]_{\bar{l}} \Delta t_l \quad + \quad \frac{4\pi \left(\rho R^3\right)_1}{n-3} \tag{79}$$

and

$$E\left(t_k\right) = \sum_{l=2}^{k} 4\pi \left[\frac{v^2}{2} \rho R^2 \left(v - \dot{R}\right)\right]_{\bar{l}} \Delta t_l \; + \; \frac{4\pi \left[\left(v^2/2\right) \rho R^3\right]_1}{n-5} \; , \tag{80}$$

where here R is just the photometric radius r_{pho}, v is the photometric velocity, ρ is obtained from the empirical density profile, the subscripts k, l, and 1 are observation numbers (e.g., SAAO observation 1, SAAO observation 2, etc.), the subscripts $\bar{l}$ indicate averages of the l and $l-1$ quantities, the sums are zero for $k = 1$, Δt_l is the time between observations l and $l-1$, and

$$\dot{R}_{\bar{l}} \equiv \left(R_l - R_{l-1}\right) \Big/ \Delta t_l \tag{81}$$

is the approximate rate of change of the photospheric (i.e., photometric) radius with time. The second terms in equations (79) and (80) were evaluated by extrapolating the density profiles to infinity using an inverse power-law fitted density profile for the outermost layers (see Fig. 15 for the n value for epoch A) and doing analytical integrations. The day 258 values of the photospheric outflow quantities are taken to be the empirical total mass and empirical total kinetic energy of the supernova ejecta. Of course, the photometric radius is nonzero on day 258. However, since the photometric radius by this late epoch is probably no longer closely related to the real photosphere, which may no longer exist, the complication of mass and energy interior to the day 258 photometric radius has not been considered in integrating for the empirical total quantities. The empirical total mass of the supernova ejecta is, of course, equal to the model 10H mass of $14.55\,M_\odot$ since the τ_{con}/χ value was chosen to recover the model 10H mass. The empirical total kinetic energy is 13.06×10^{50} ergs which is smaller than, but allowing for all the uncertainties consistent with, the model 10H total kinetic energy of 14×10^{50} ergs.

Figure 20 shows the photometric velocity and the model 10H velocity plotted as functions of mass coordinate where mass is measured inward from the surface. The mass coordinate for the photometric velocity is just the derived empirical photospheric outflow mass. The near-vertical increase and then plateau region in the inner part of the model 10H velocity curve is just the effect, now appearing in the velocity curve, of the radioactive acceleration discussed above for the model 10H density profile. As Figure 20 shows, the average velocity of roughly the outermost $1\,M_\odot$ of ejecta is higher in the empirical analysis results than in model 10H results. Figure 21 shows the empirical and the model 10H density profiles plotted as functions

of mass coordinate. The behaviors of the empirical and the model 10H curves in both Figures 20 and 21 are not inconsistent allowing for all the uncertainties.

b) Line Optical Depths and Abundances

Considering the large number of observed spectra to be examined, it is not very sensible to try to fit synthetic spectra by varying all the photospheric Sobolev optical depths for each spectrum; it would take a long time and interpreting the fitted optical depths would be difficult. Instead a set of photospheric Sobolev optical depths for each observed spectra have been calculated using TE, estimated photospheric electron densities, the color temperatures, and an assumed composition. The electron densities were calculated using the inverse power-law expression for electron density from equation (64) (see § III) with the n values taken from Figure 15 for the appropriate epochs and with $\tau_e = 1$. These electron densities are, of course, very approximate because of the simplifying assumptions used in deriving equation (64) and since again the photometric radii are used as the photospheric radii for all times.

With the photospheric electron densities calculated as just described, the photospheric electron density evolution with time is exactly the inverse power-law fit curve in Figure 17 divided everywhere by the Thomson cross-section σ_e. Using the electron densities, the color temperatures, an assumed composition, and TE, it would have been possible to calculate a density profile. This was not done; the empirical density profile, calculated as described in § V*a*, was preferred because fewer, albeit very simplifying, assumptions were needed for its construction. The inconsistency in using TE-predicted optical depths that imply a different density profile from the density profile actually used is not very troubling since any effects the inconsistency leads to are probably no greater than the uncertainties due to the approximate natures of both the TE-predicted optical depths and the empirical density profile.

Since the hydrogen envelope must consist mostly of material that has never undergone nuclear burning in the supernova or progenitor star, the envelope composition should be mostly a zero age main sequence (ZAMS) composition. Some convective mixing of material that has undergone nuclear burning into the envelope is possible both in the presupernova star (Woosley 1988) and in the explosion itself (Benz and Thielemann 1990). In the helium core, all the material has been through some nuclear burning except for ZAMS material that has been convectively mixed down into the core. Using a ZAMS composition in a TE calculation and assuming that the photospheric electron densities and the color temperatures used in the calculation are truly characteristic values for line formation, one can make a useful comparison of the relative sizes of the calculated synthetic spectrum features to the relative sizes of the observed spectrum features. Absolute size comparisons are less reliable with the ES model since the true continuum formation is not treated (see § III). Discrepancies in the relative size comparison would suggest NLTE effects or compositional deviations from the ZAMS composition in the supernova. For the synthetic spectrum calculations reported here, the primitive solar nebula composition given by Cameron (1982) has been used; for brevity, this composition is simply called the solar composition hereafter. Actually, the ZAMS composition for the LMC has a metallicity reduced by a factor of about 4 from the solar composition (see, e.g., Dufour, Shields, and Talbot 1982). However, since it is the relative strength of the metal lines that is of main interest in this analysis, solar composition is adequate. The predicted photospheric Sobolev optical depths calculated using the solar composition and the other assumptions (TE, color temperature, estimated photospheric electron density, etc.) are hereafter usually called the solar-composition TE-predicted optical depths.

In the synthetic spectra calculations, 19 ions (see Figures 22a–22c for their designations) and over 400 transitions were included. It is believed that all the most important and interesting optical transitions for SN II spectra have been included. The transition data was taken from various sources: e.g., Wiese et al. (1966, hydrogen through neon data), Wiese et al. (1969, sodium through calcium data), Wiese and Fuhr (1975, scandium and titanium data), Younger et al. (1978, vanadium, chromium, and manganese), and Phillips (1979, Fe II data). Table 1 shows the transition data for a selection of the transitions that were particularly important or interesting in calculating the synthetic spectra for SN 1987A. Throughout this article all kinds of transitions are usually referred to simply as lines. This usage is convenient since it is usual to talk about line profiles, but not about transition profiles. However, many of the transitions used are formally multiplets: e.g., He I λ5876 and Li I λ6708. The hydrogen Balmer transitions are formally transition arrays.

Figures 22a–22c show, plotted as functions of time, the solar-composition TE-predicted photospheric

TABLE 1—Transition data for a selection of the transitions that were particularly important or interesting in calculating the synthetic spectra for SN 1987A.

λ (Å)	E (eV)	$\log(gf)$	Ion	λ (Å)	E (eV)	$\log(gf)$	Ion
512.	2.48	-1.06	Cr II	5198.	3.22	-2.38	Fe II
546.	1.10	-0.23	V II	5270.	0.86	-1.41	Fe I
660.	10.20	-3.07	H I	5527.	1.76	0.06	Sc II
835.	10.20	-1.36	H I	5535.	3.23	-3.08	Fe II
889.	10.20	-1.19	H I	5641.	1.49	-1.01	Sc II
889.	19.81	-0.72	He I	5658.	1.50	-0.50	Sc II
901.	1.13	-0.27	Ti II	5658.	1.49	-1.12	Sc II
934.	0.00	0.14	Ca II	5667.	1.49	-1.20	Sc II
956.	0.01	-0.16	Al I	5669.	1.49	-1.09	Sc II
968.	0.00	-0.16	Ca II	5683.	2.10	-0.70	Na I
970.	10.20	-0.99	H I	5684.	1.50	-1.01	Sc II
032.	0.00	-0.08	Mn I	5688.	2.10	-0.45	Na I
078.	0.00	0.17	Sr II	5876.	20.95	0.74	He I
102.	10.20	-0.75	H I	5890.	0.00	0.12	Na I
216.	0.00	-0.15	Sr II	5896.	0.00	-0.19	Na I
226.	0.00	0.20	Ca I	6142.	0.70	-0.16	Ba II
233.	2.57	-1.92	Fe II	6148.	3.87	-2.84	Fe II
270.	0.00	0.25	Cr I	6149.	3.87	-2.89	Fe II
340.	10.20	-0.45	H I	6238.	3.87	-2.80	Fe II
395.	1.08	-0.55	Ti II	6246.	1.50	-0.93	Sc II
550.	1.58	-0.22	Ti II	6248.	3.87	-2.46	Fe II
554.	0.00	0.19	Ba II	6347.	8.12	0.22	Si II
584.	2.79	-2.10	Fe II	6371.	8.12	-0.07	Si II
861.	10.20	-0.02	H I	6456.	3.89	-2.26	Fe II
924.	2.88	-1.61	Fe II	6497.	0.60	-0.46	Ba II
934.	0.00	-0.13	Ba II	6516.	2.88	-3.18	Fe II
018.	2.88	-1.40	Fe II	6563.	10.20	0.71	H I
169.	2.88	-1.66	Fe II	6605.	1.35	-1.08	Sc II
184.	2.72	-0.32	Mg I	6678.	2.69	-1.51	Fe I
189.	1.58	-1.20	Ti II	6708.	0.00	0.01	Li I

NOTE: No distinction is made in this table between line, multiplet, and transition array transitions.

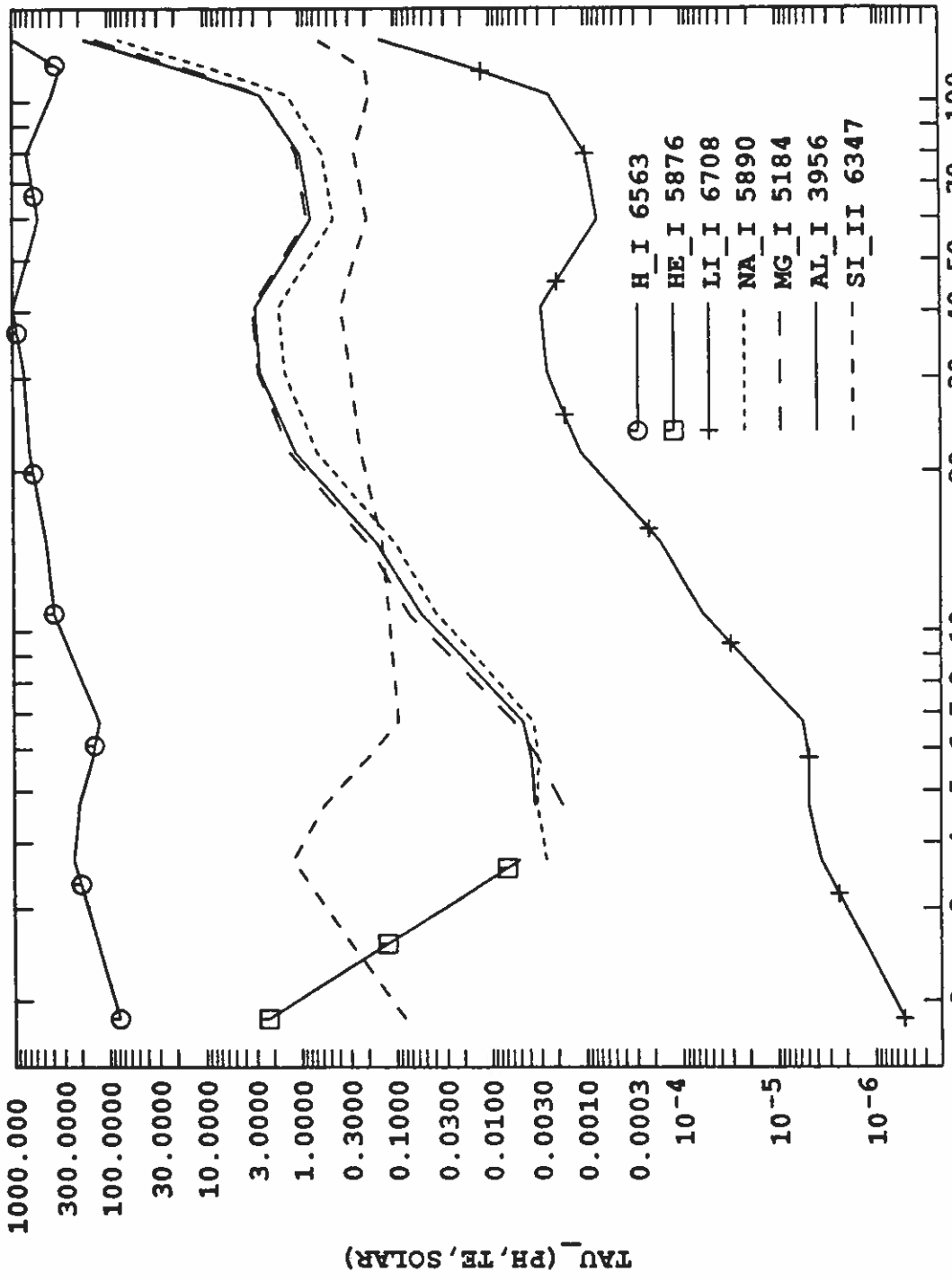

Fig. 22a: *Solar-composition TE-predicted photospheric Sobolev optical depths.*

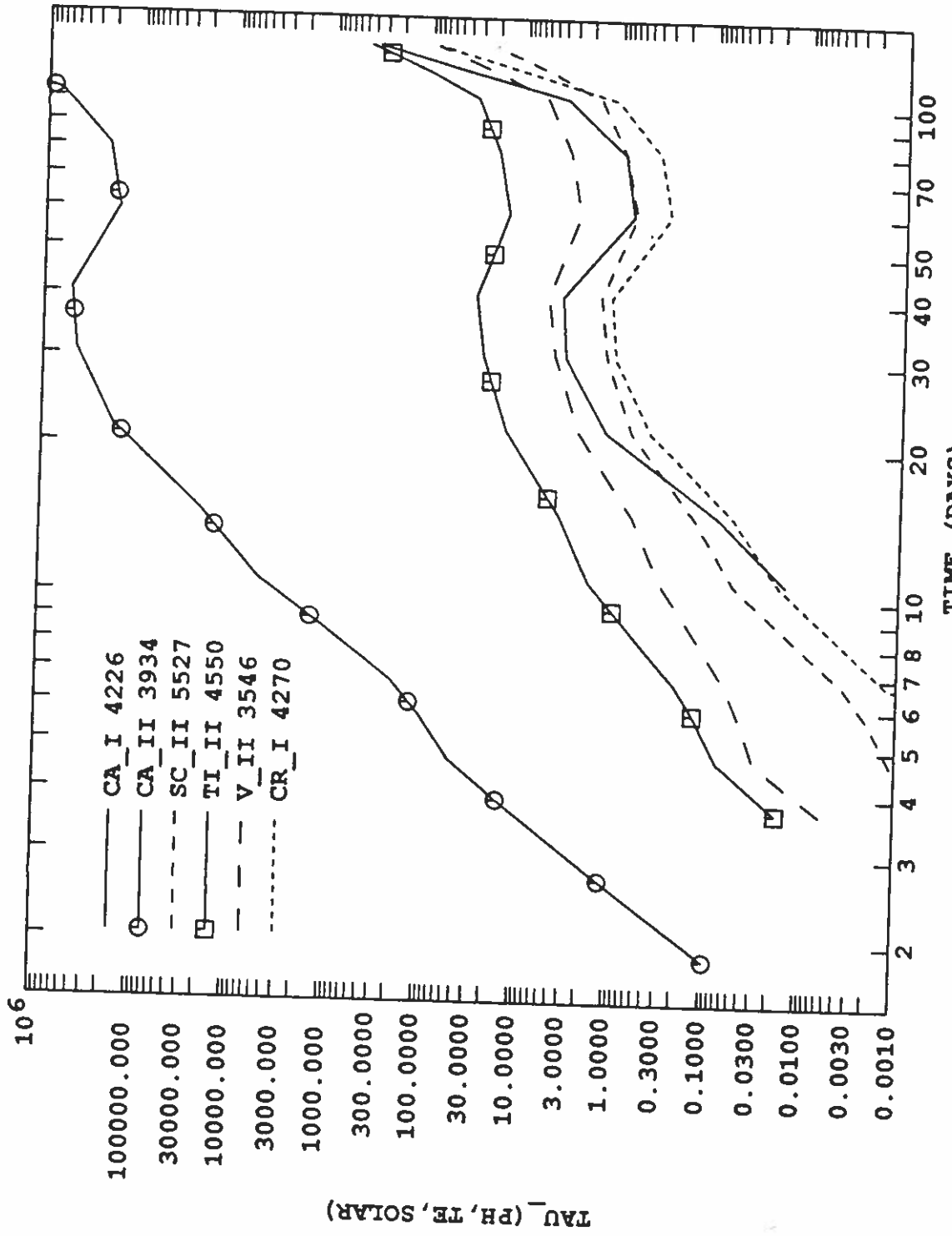

Fig. 22b: *Solar-composition TE-predicted photospheric Sobolev optical depths.*

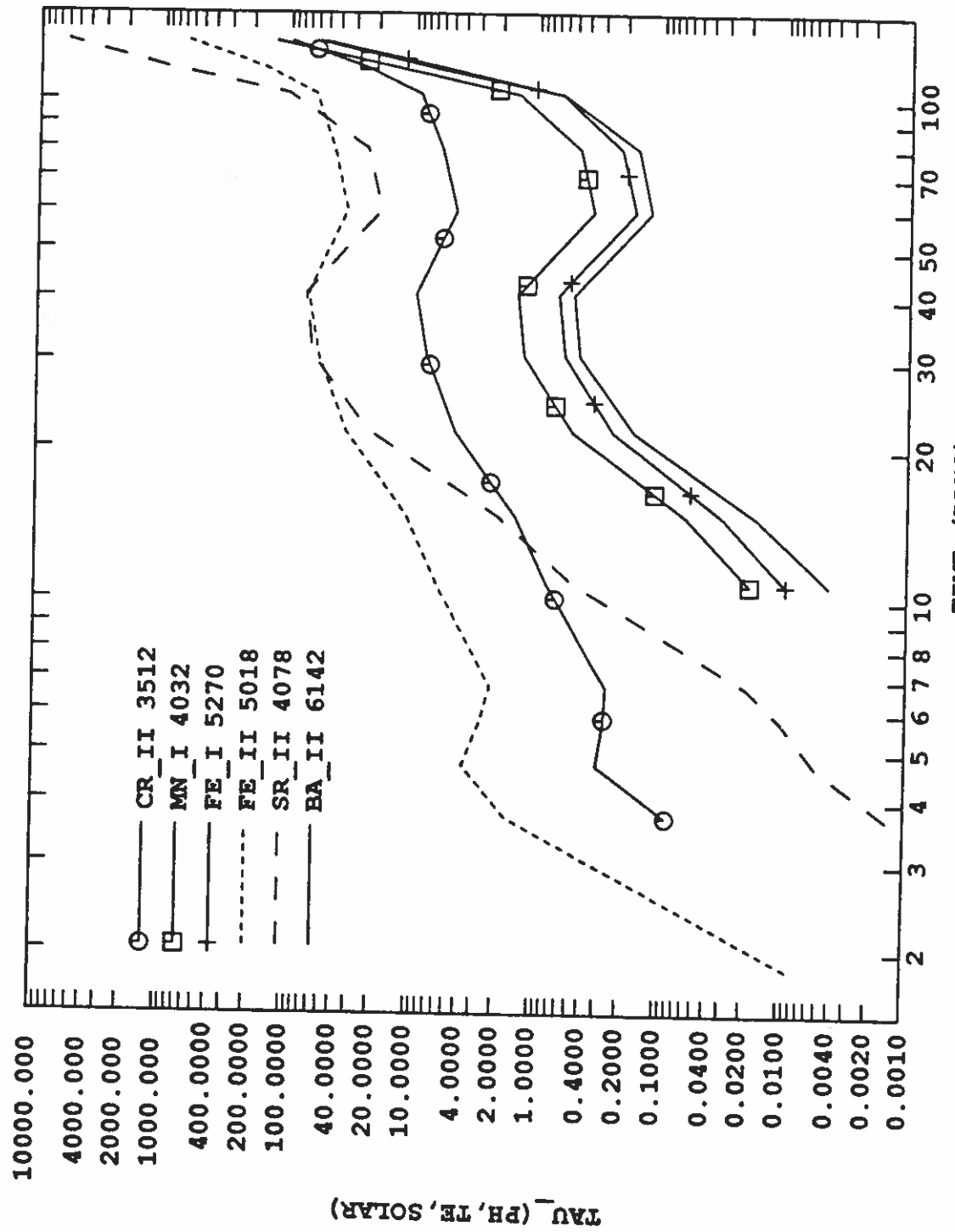

Fig. 22c: *Solar-composition TE-predicted photospheric Sobolev optical depths.*

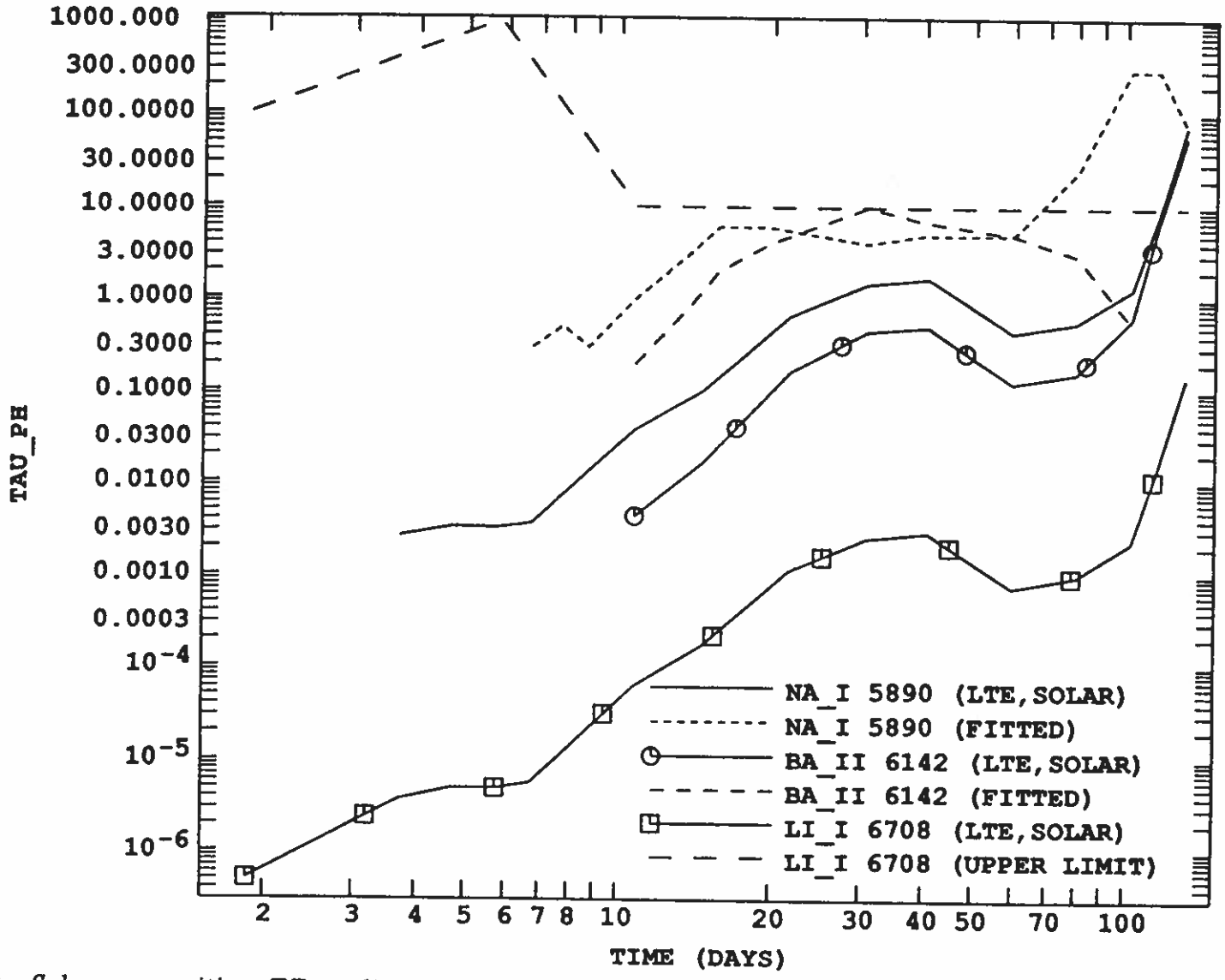

Fig. 23: *Solar-composition TE-predicted and spectrum-fitted photospheric Sobolev optical depths, and upper limits on the Sobolev photospheric optical depths of the Li I 6708 line.*

optical depths calculated for a strong line for each ion considered. For brevity, the chosen strong lines will be called the control lines; the line data for all the control lines appears in Table 1. The photospheric Sobolev optical depths for the noncontrol lines for each ion were calculated using the control line optical depths, the color temperature, and equation (66). Photospheric optical depths that are less than ~ 0.1 will not give rise to very noticable line features (see Fig. 3); the cumulative effect of many weak lines is, of course, important (see § III). The Hα line varies in strength by only about a factor of 10 over the first 131 days. The He I λ5876 line strength declines to insignificance in the first 4 days. The lower level of this line is 20.95 eV above the ground level, and thus the level occupation number is a very rapidly increasing function of temperature for temperatures of order 10^4 K. The other optical He I lines are weaker than the 5876 Å line. As discussed in § V*a*, the He I λ5876 line may become significant again in the observed spectra after about day 76 due to a radioactive nonthermal effect. The metal line optical depths show an initial increasing phase due to the rapid decline in color temperature during the first 20 days (see Figs. 14a–14b): the decreasing temperature greatly increases the abundances of the ionization stages to which the metal lines belong. During the period when color temperature is relatively constant from about day 20 to day 90, the metal line optical depths do not vary strongly. When the temperature starts falling rapidly after about day 90, the hydrogen recombines much more completely in the TE calculation, and thus, to maintain the imposed photospheric electron density, the particle density must increase greatly so that the electrons contributed by the ionized metals will increase greatly. This large increase in calculated particle density leads to the large increase in the TE-predicted optical depths of the metal lines after about day 100. As will be seen in § V*c*, the post-day-100 large increase in metal line optical depths leads to a general discrepancy between the synthetic and observed spectra (see Figs. 34–36) that is not present for earlier times (see Figs. 24–33). Therefore, after day 100, the solar-composition TE synthetic spectra can no longer be confidently used as a basis for detecting NLTE or non-solar abundance effects in the formation of the observed spectra; in the discussion given below, no conclusions are drawn about these effects on this basis for the post-day-100 epoch. The general discrepancy after day 100 is certainly due to the failure of one or more of the many assumptions used in calculating the synthetic spectra. It may be that TE is generally inadequate to describe the post-day-100 epoch. On the other hand, it may be that TE is still valid but that the color temperature, the assumed photospheric electron density, or both of these are no longer good characteristic values for line formation. It seems unlikely that the real photospheric electron density could fall by the two orders of magnitude that are needed to keep the post-day-100 metal line optical depths very roughly equal to their pre-day-100 and probably more accurate values since electron opacity is probably needed to cause a significant part of the optical depth to the photosphere. Therefore, it seems more probable that the general discrepancy, if not due to NLTE effects, is due the color temperature ceasing to be a good characteristic temperature.

The solar-composition TE-predicted optical depths generally yielded synthetic spectra that were reasonably consistent with the observed spectra, although, as stated just above, the consistency is notably poorer after day 100. There is no strong evidence from comparisons of the observed and synthetic spectra that an LMC ZAMS composition with its low metallicity would have given greater overall consistency than the assumed solar composition. A lower metallicity would have given greater consistency in the post-day-100 epoch, but one would expect higher not lower metallicities to be appropriate for epochs when the photosphere had receded into the deeper and probably more metal-rich ejecta.

No general fine tuning of the optical depth values was undertaken to obtain better fits of synthetic to observed spectra since it was thought that the uncertainty in the fitted values would usually be larger than any difference of the fitted values from the predicted values. This being the case, a general fine tuning would have been merely cosmetic and would have obscured the real degree of consistency between prediction and observation. However, for the lines of three ions, Na I, Ba II, and Li I, the optical depths were varied from the predicted values. For Na I and Ba II, the variation was done because the predicted optical depths for their lines were distinctly too weak for the synthetic spectra to fit observed spectrum features. Many other authors have previously noted that something other than TE and solar composition are needed to fit the line profiles attributed to Na I and Ba II (e.g., Höflich 1988). For Li I, the variation was done to try to put an upper limit on lithium abundance; none of the synthetic spectra calculated with the varied Li I optical depths are displayed in this article. For the variations, only the control line for each ion was varied explicitly and the other ion lines were again calculated using equation (66). The predicted optical depths and final fitted or upper limit optical depths for the control lines of Na I, Ba II and Li I are shown in Figure 23. It should be noted that no abundance alteration considered in the discussion below for the three elements sodium,

barium, and lithium is too large to invalidate the simple interpretation of the ratio of fitted optical depth to predicted optical depth as the ratio of real abundance to solar abundance. This simple interpretation would become invalid if it yielded an abundance that was so far from the solar abundance that the abundance normalization was significantly affected or that implied a significantly different photospheric electron density than that assumed in the prediction calculations. Of course, if the assumptions, in particular that of TE, used in calculating the synthetic spectra fail, then the simple interpretation of optical depth ratios is of doubtful validity.

In the case of the Na I, it is the line profile attributed to the Na I λ5892 doublet (i.e., the Na D resonance lines) that is too strong compared to the solar-composition TE prediction. This line profile's trough feature is probably present in the observed spectra blueward of 5892 Å from about day 7 on; the trough feature becomes unambiguous in the day 8.71 observed spectrum (see Figure 27). No other line features in the observed spectra are identifiable as due to Na I lines nor were such line features expected from the solar-composition TE-predicted optical depths. From Figure 23, it can be seen that until day 131 the fitted Na I line optical depths varied between being about a half to about 2 orders of magnitude larger than the predicted optical depths; for the post-day-100 epoch, the difference between the fitted and predicted optical depths is considered too uncertain for any conclusions to be drawn. The unpredicted strength of the observed line profile can be attributed to three possible causes which are perhaps all operative: NLTE effects, overabundance of sodium relative to solar composition, and, as already discussed, line blending from a radioactive-nonthermal-effect strengthened He I λ5876 line. Since the He I λ10830 line is still relatively weak on day 76 (Elias et al. 1988) and the He I λ5876 line must be weaker still at that time, it seems probable that the first two possible causes need to be invoked to explain the early strength of the observed line profile. In the TE calculations, Na I is orders of magnitude less abundant than Na II thoughout the first 100 days; thus, a NLTE effect that is small in the sense that it does not greatly affect the main ionization stage abundance could radically increase the Na I abundance. However, in a NLTE investigation, Höflich (1988) requires a sodium overabundance relative to solar composition of a factor of about 5 in order to fit the observed spectra; this factor is roughly consistent with what the ES model TE spectrum fit requires considering all the uncertainties in ES model calculations. Höflich's calculations did not include a radioactive nonthermal effect on He I; the inclusion of such an effect might alter his results. The presence of a strong line profile located at the appropriate wavelength to be attributed to the Na I doublet is not a unique feature of SN 1987A; present evidence suggests that all SNe II exhibit such a profile for some period in their evolution.

In the case of Ba II, it is the line profile fairly confidently attributed to the Ba II λ6142 line that is noticably too strong compared to the solar-composition TE prediction. Other important Ba II lines are in regions where there is too much line blending to tell if these lines are also too strong. From Figure 23, the ratio of the fitted to predicted Ba II λ6142 line optical depths is seen to decline from about 15 on day 10 to about 10 on day 80. After day 100 the discrepancy between the fitted and predicted values vanishes; however, this consistency is not considered significant. The strength of the Ba II line may be a NLTE effect. In the solar-composition TE predictions, the Ba III ion is a factor of order 10 more abundant than the Ba II at 5500 K and of comparable abundance at 5000 K. Thus, either a NLTE-heightened Ba III recombination rate or a lower characteristic temperature for the TE optical depth calculations could account for the observed Ba II λ6142 line profile. However, a sufficiently lower characteristic temperature may worsen the overall fit of the synthetic to the observed spectra; lowered characteristic temperatures in the post-day-100 epoch do make the solar-composition TE-predicted Ba II λ6142 line optical depth larger, but also worsen the overall fit (see the discussion of Figures 34–36 in § V*c*). Höflich's NLTE investigation found that barium needed to be overabundant by a factor of about 10 relative to solar composition. This requirement is qualitatively quite consistent with what the TE fits to the observed spectra require. Among other SNe II, only SN 1985H exhibits a line profile similar to the line profile attributed to Ba II λ6142 in the SN 1987A spectra (Wheeler, Harkness, and Barkat 1988). Since only one spectrum and few other kinds of observations exist for SN 1985H, an extensive comparison to SN 1987A is not possible.

Dearborn et al. (1989) find that the Population I lithium abundance, which is within a factor of 2 of solar-composition lithium abundance (i.e., primitive solar nebula composition lithium abundance), may be largely due to nucleosynthesis in SNe II. From their blue-star explosion models, which are appropriate to compare to the blue-star explosion of SN 1987A, they find a range of $\sim 10^{-7}\,M_\odot$ to $\sim 10^{-5}\,M_\odot$ of lithium may be synthesized by the explosion shock wave at the base of the hydrogen envelope. A solar mass with solar composition would contain $\sim 10^{-8}\,M_\odot$ of lithium. Thus, if lithium is produced in the quantities predicted

by Dearborn *et al.*, then there could be an enhancement of the strength of lithium lines by up to a factor of 100 over a solar-composition prediction of line strength if it is imagined that the synthesized lithium is convectively mixed over of order 10 $M_\odot$ of a supernova's ejecta. If the synthesized lithium is confined to a mass shell, then the lithium line profiles would first appear when the photosphere receded into the mass shell. The line profiles for a mass shell would tend to look like the profiles for a geometrically thin atmosphere (see § IV and Fig. 8) when the photosphere was inside the mass shell and like the profiles for a detached atmosphere (see § IV and Fig. 6) when the photosphere had receded substantially below the mass shell.

The SN 1987A spectra were examined for the presence of the Li I λ6708 resonance line which in TE with the assumed temperatures and photospheric electron densities should be very much the strongest optical lithium line. No noticable profile could be detected. Synthetic spectrum analysis was done to show that the red wing Hα Bochum feature (see § V*c* for a discussion of the Bochum features) could not reasonably be interpreted as 6708 Å line profile. The solar-composition TE synthetic spectra calculations which include Li I never produced a noticable 6708 Å line profile; thus they are entirely consistent with the observed spectra. However, given the Dearborn et al. prediction, it became interesting to try to put a TE upper limit on the amount of lithium that could exist in the supernova. The procedure chosen was cautious; the 6708 Å line optical depth was increased until a detectable synthetic line profile was created that no compensating effect that was imagined could have made undetectable. The upper limit 6708 Å line optical depths are plotted in Figure 23. If no compensating effects had been allowed for in procedure, the upper limit optical depths would be a factor of 10 smaller; let such upper limits be called the less-cautious upper limits. From Figure 23 and not counting the post-day-100 period, the greatest enhancement of lithium abundance relative to the solar composition allowed by assumptions of the present analysis would be about a factor of 3500; using the less-cautious upper limits, the factor would be only about 350. Thus, if even the largest amount of synthesized lithium found by Dearborn et al. is well mixed throughout the ejecta, the Li I λ6708 line would be at best marginally detectable assuming the less-cautious limit of detectability. However, if there is a NLTE effect that increased the abundance of the Li I ion by a factor of order 3 or more, then a detectable feature would become probable for the largest lithium production case; such a NLTE effect is possible since the lithium atom is very similar to the sodium atom where some NLTE effect enhancing the first ionization stage abundance may occur (see above). If the predicted amount of synthesized lithium is confined to a mass shell, then detectable although unusual line profiles might be expected even from a TE analysis and even assuming less lithium than in the largest production case. To conclude, there is no inconsistency between Dearborn *et al.*'s predictions of lithium synthesis in SNe II and the lack of any Li I λ6708 line in the SN 1987A spectra. However, given their results, it is possible that the Li I λ6708 line may appear in some SN II spectra.

c) Observed and Synthetic Spectra

Observed and synthetic spectra are shown in Figures 24–36. The CTIO archive actually contains 84 spectra for the first 131 days. For the present analysis only about 20 of these spectra were examined and only 13 have been chosen for presentation. The rate of evolution of the supernova spectrum was sufficiently slow that the limited sample of spectra examined is considered adequate to follow the evolution. The details of the calibrations and uncertainty estimates for the observed spectra are given by Phillips et al. (1988); here it is sufficient to note that the B and V magnitudes derived from the spectra are found to be accurate to about 5 % and that the rapid oscillations superimposed on larger scale structures in the spectra are noise. All the presented spectra, except those in Figure 34b, are plotted on a relative flux scale normalized to the highest flux in each of the observed spectra. The flux spectra are plotted in the wavelength description form not the frequency description form: i.e., f_λ not f_ν has been plotted.

The synthetic spectra displayed in Figures 24 to 36 were calculated with the ES model using information from the photometry analysis for some of the model features. As discussed in § III, true continuum formation is not treated in the ES model and thus a continuum fitting procedure is used. For the present work, the ES model photosphere produces a blackbody radiation field at the color temperature; this field is propagated through the line scattering atmosphere to produce an emergent synthetic spectrum. The synthetic spectrum is then fitted to the observed spectrum by demanding that the integrals from 5000 Å to 6200 Å of the two spectrum curves be equal. The integration range chosen is roughly the bandwith of the V magnitude (see, e.g., Allen 1973, p. 201). The V magnitudes for SN 1987A were well fitted by the color temperature

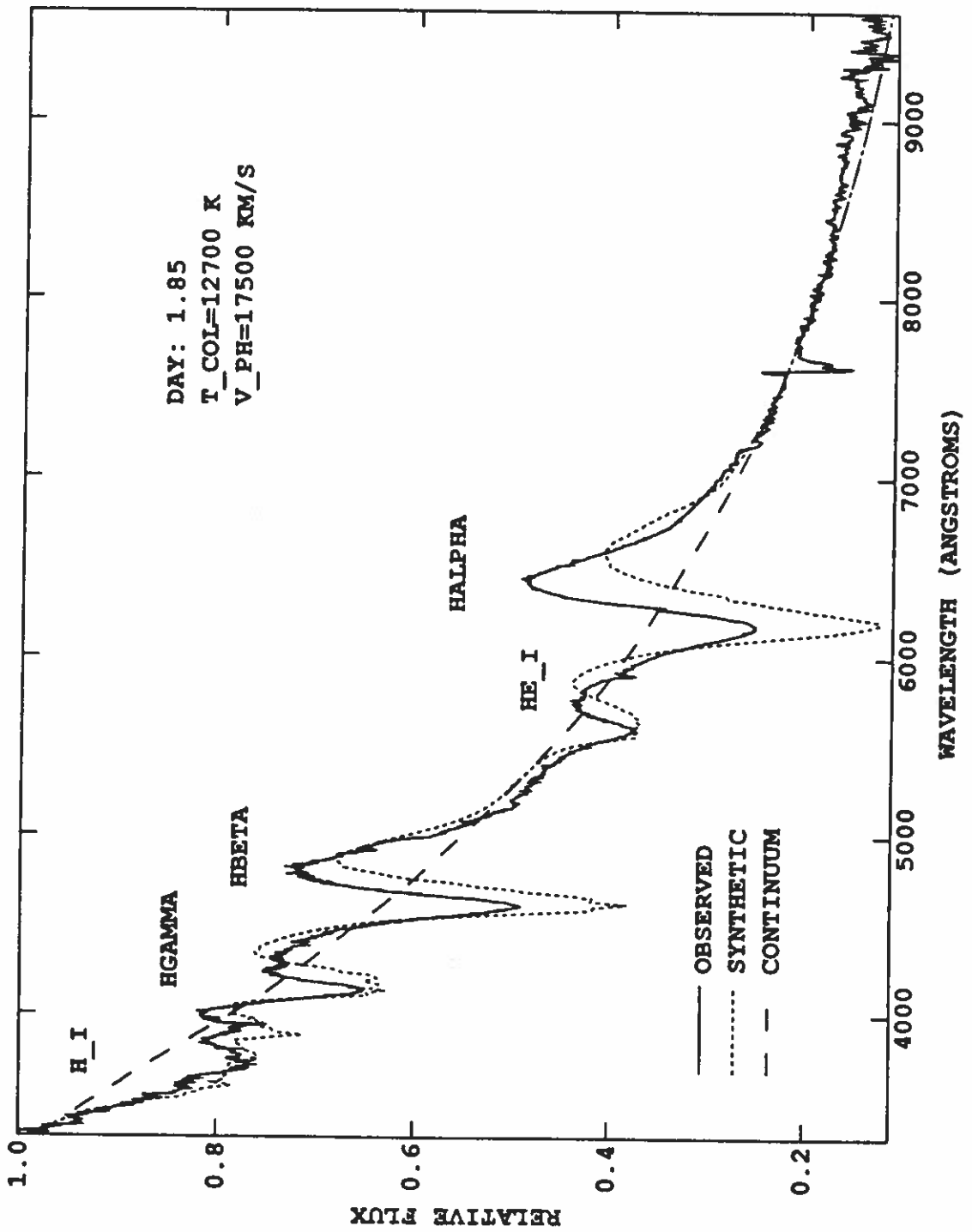

Fig. 24: *Observed and synthetic spectra for 25.17 Feb. 1987 U.T.*

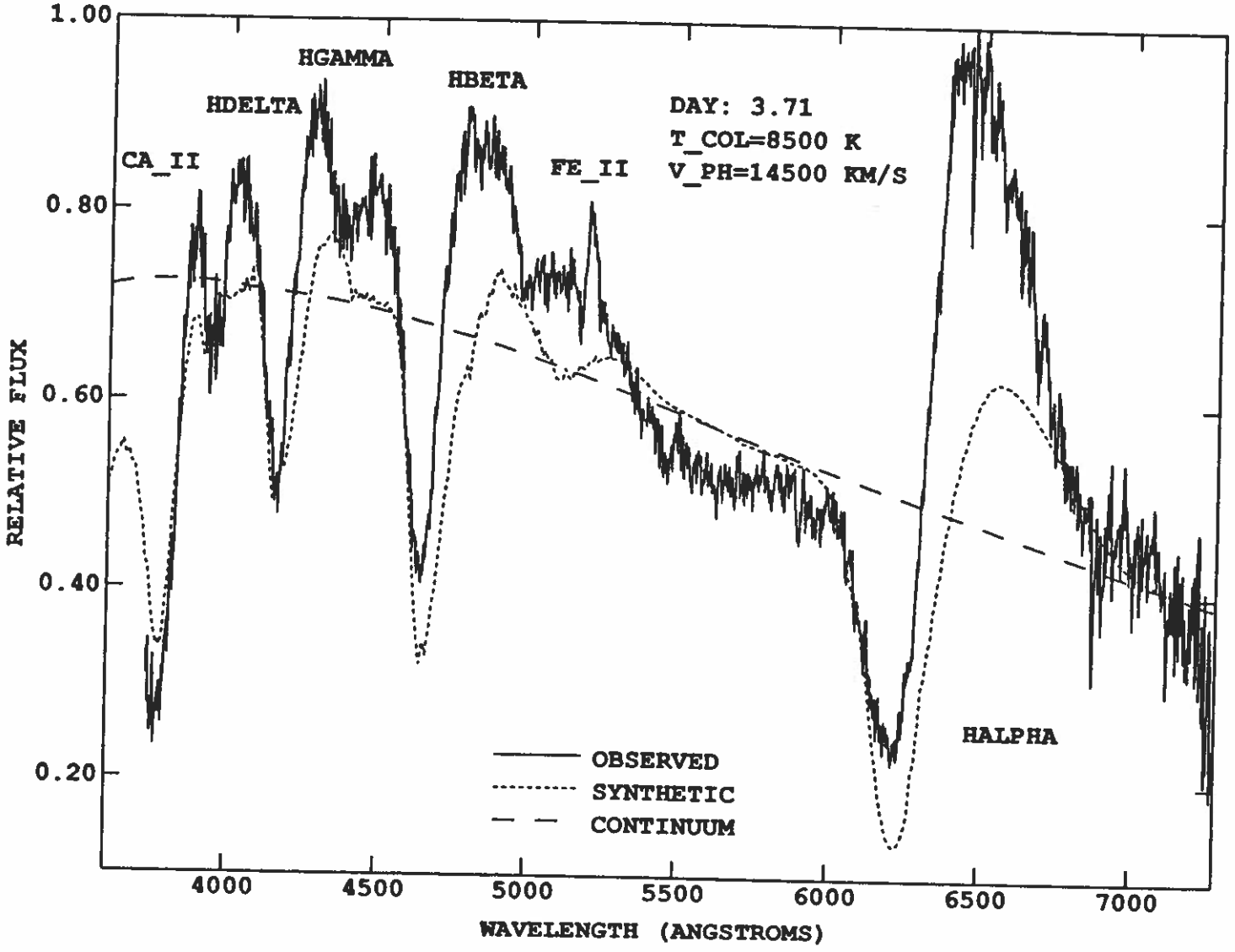

Fig. 25: *Observed and synthetic spectra for 27.03 Feb. 1987 U.T.*

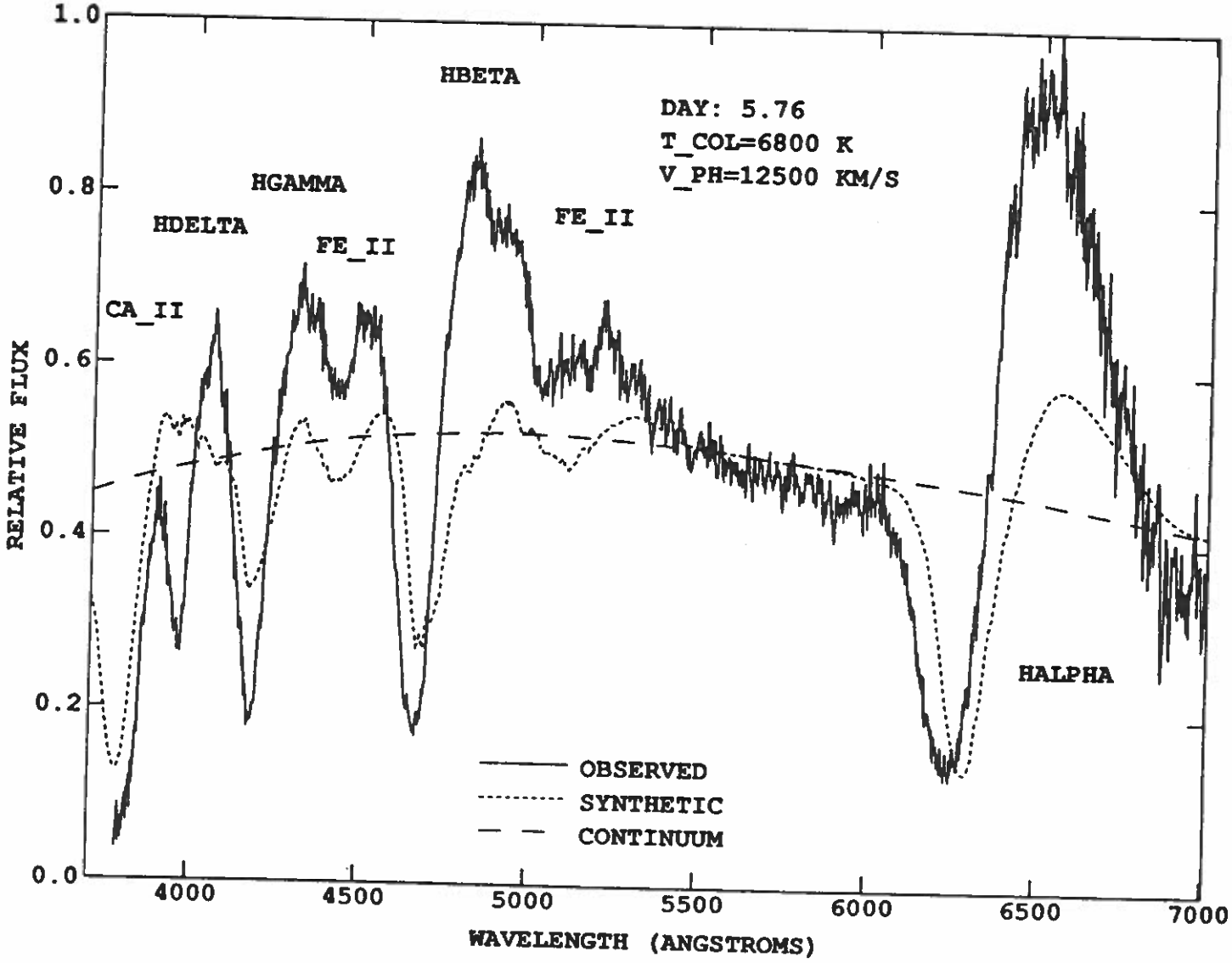

Fig. 26: *Observed and synthetic spectra for 1.07 Mar. 1987 U.T.*

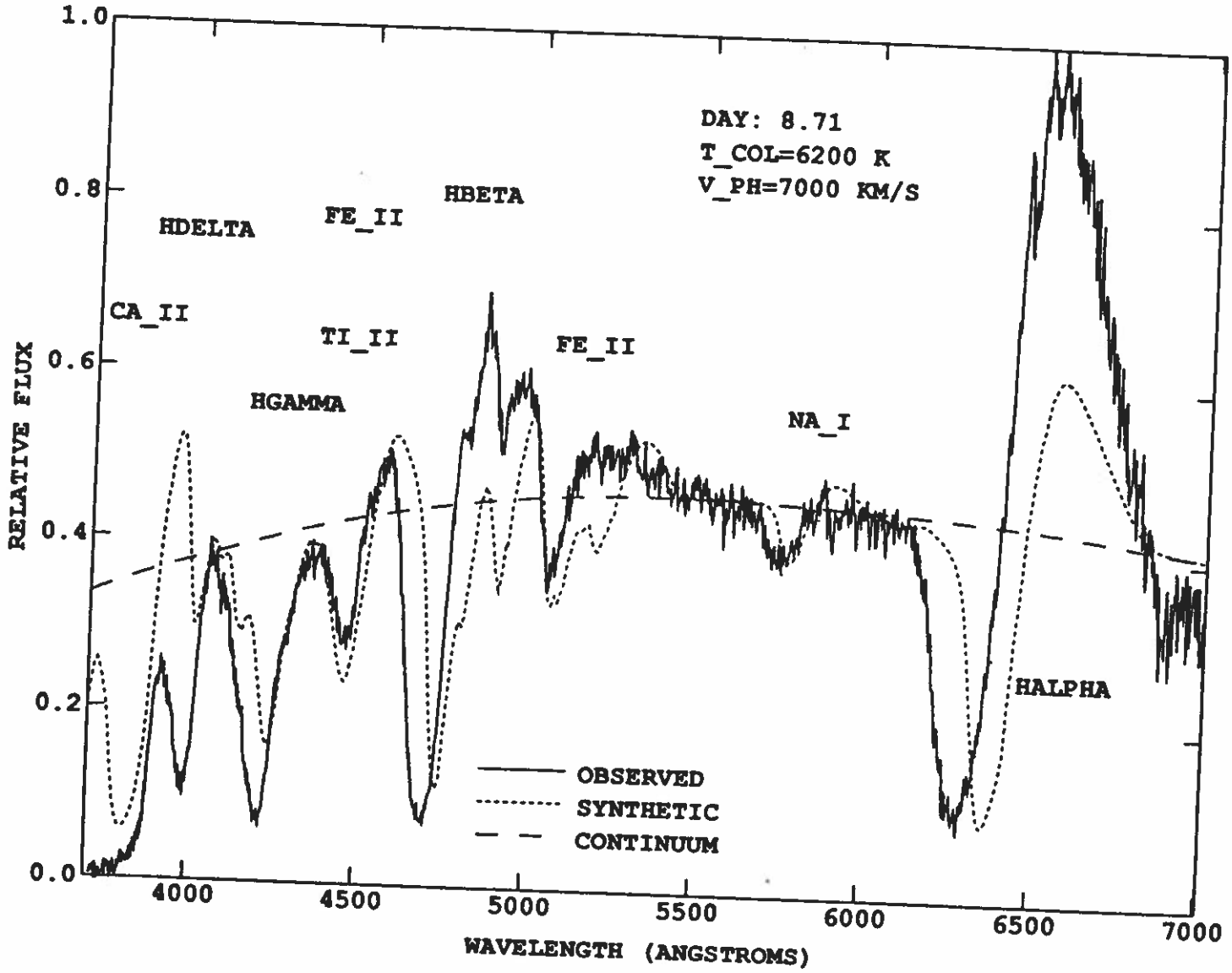

Fig. 27: *Observed and synthetic spectra for 4.02 Mar. 1987 U.T.*

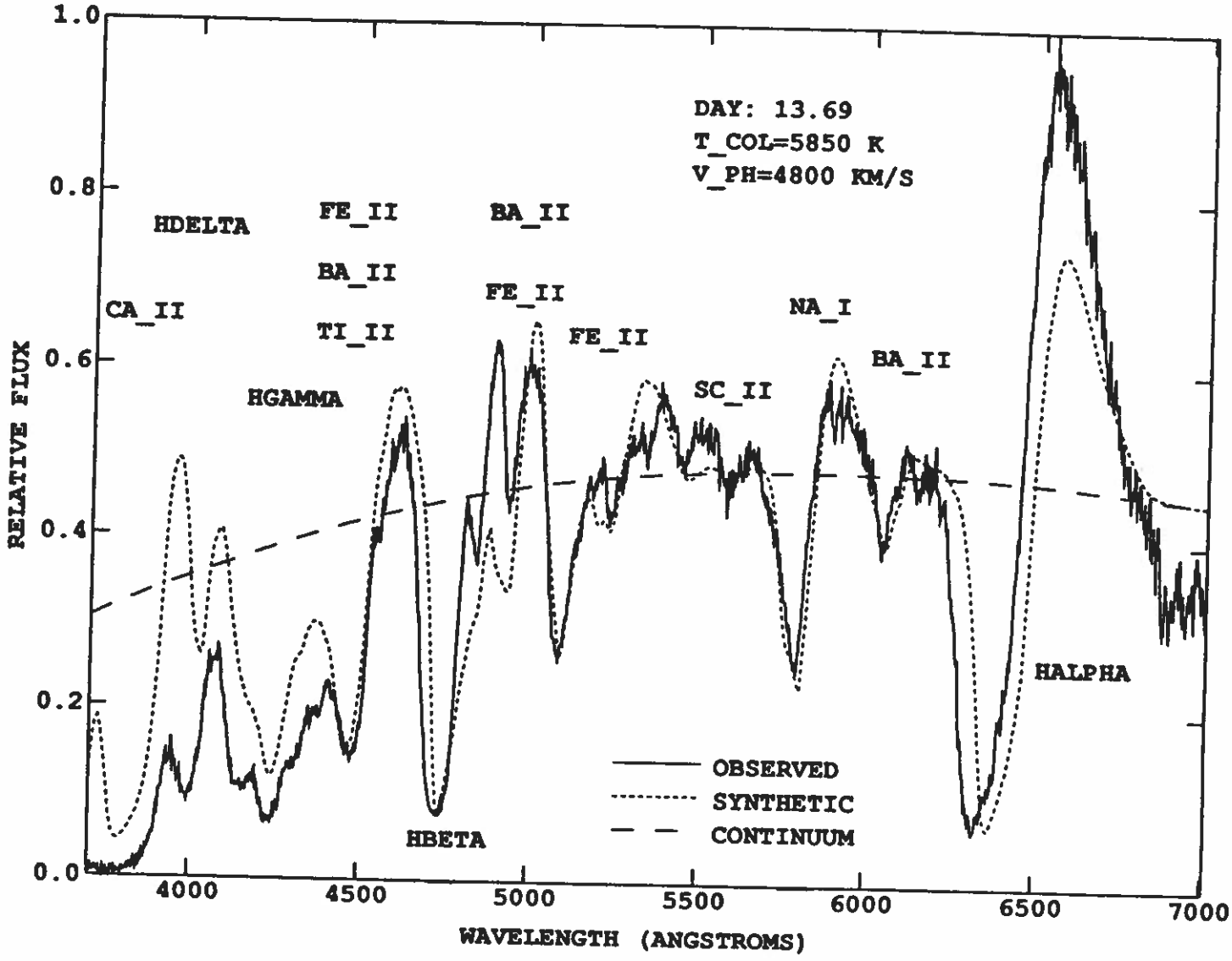

Fig. 28: *Observed and synthetic spectra for 9.00 Mar. 1987 U.T.*

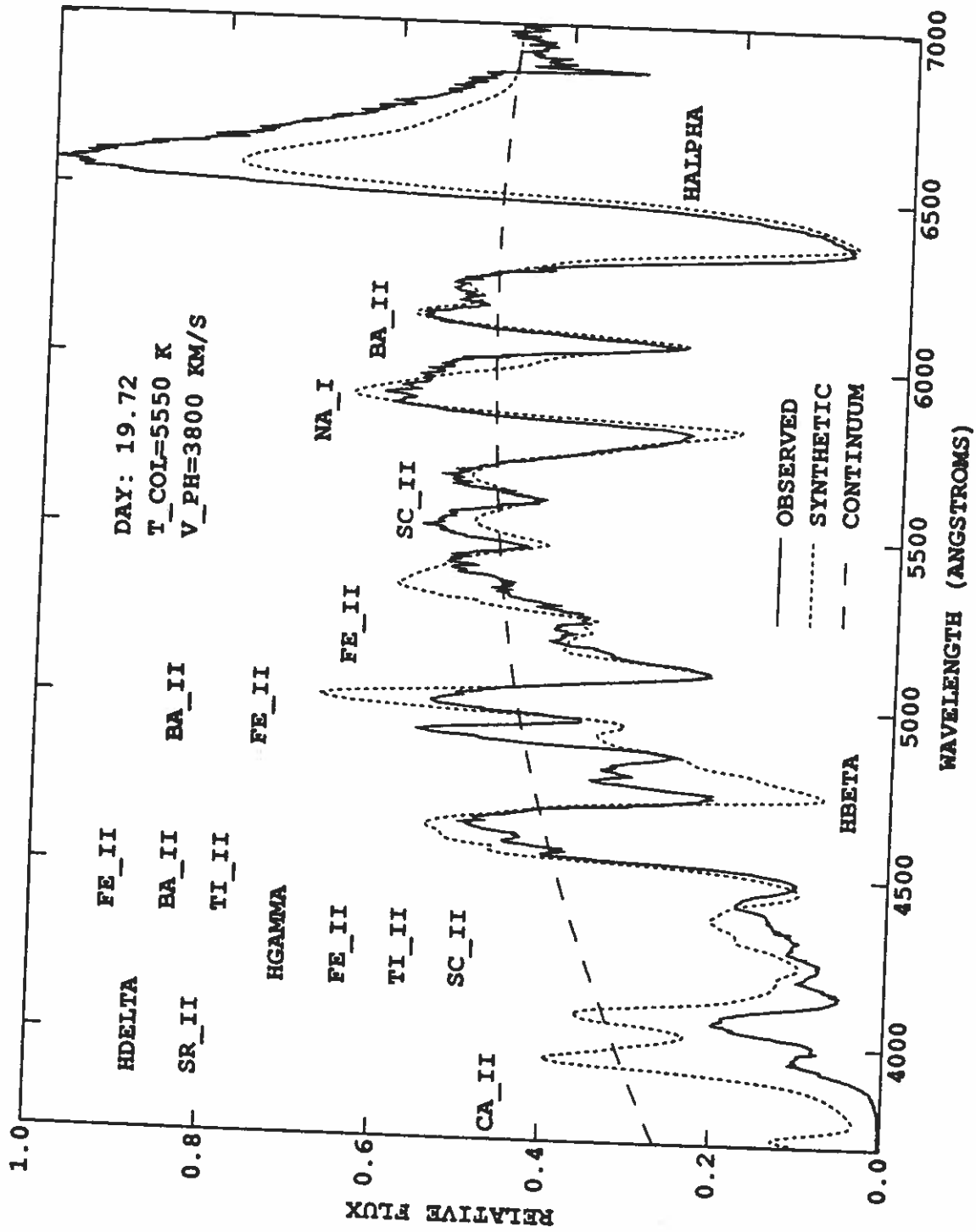

Fig. 29: *Observed and synthetic spectra for 15.03 Mar. 1987 U.T.*

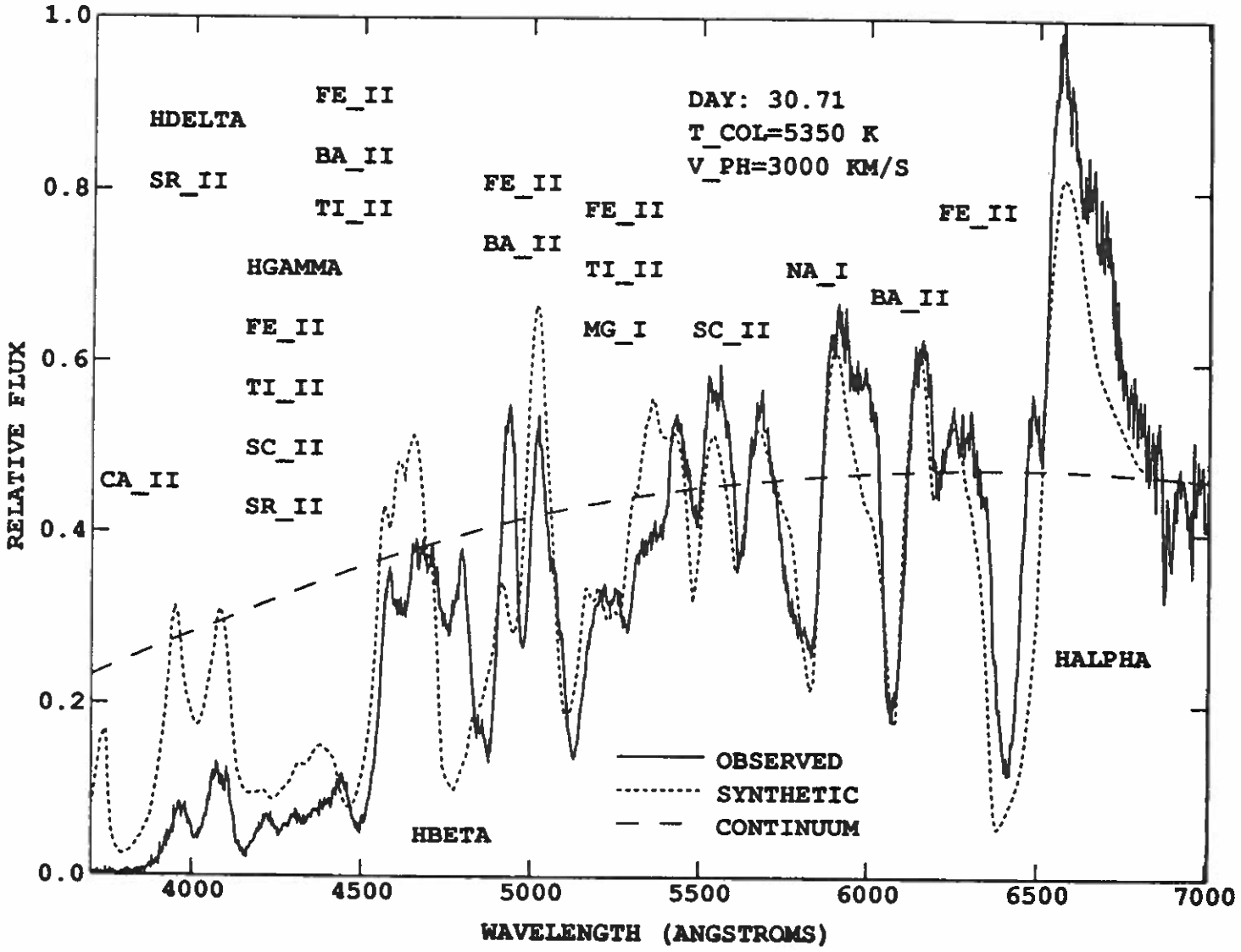

Fig. 30: *Observed and synthetic spectra for 26.02 Mar. 1987 U.T.*

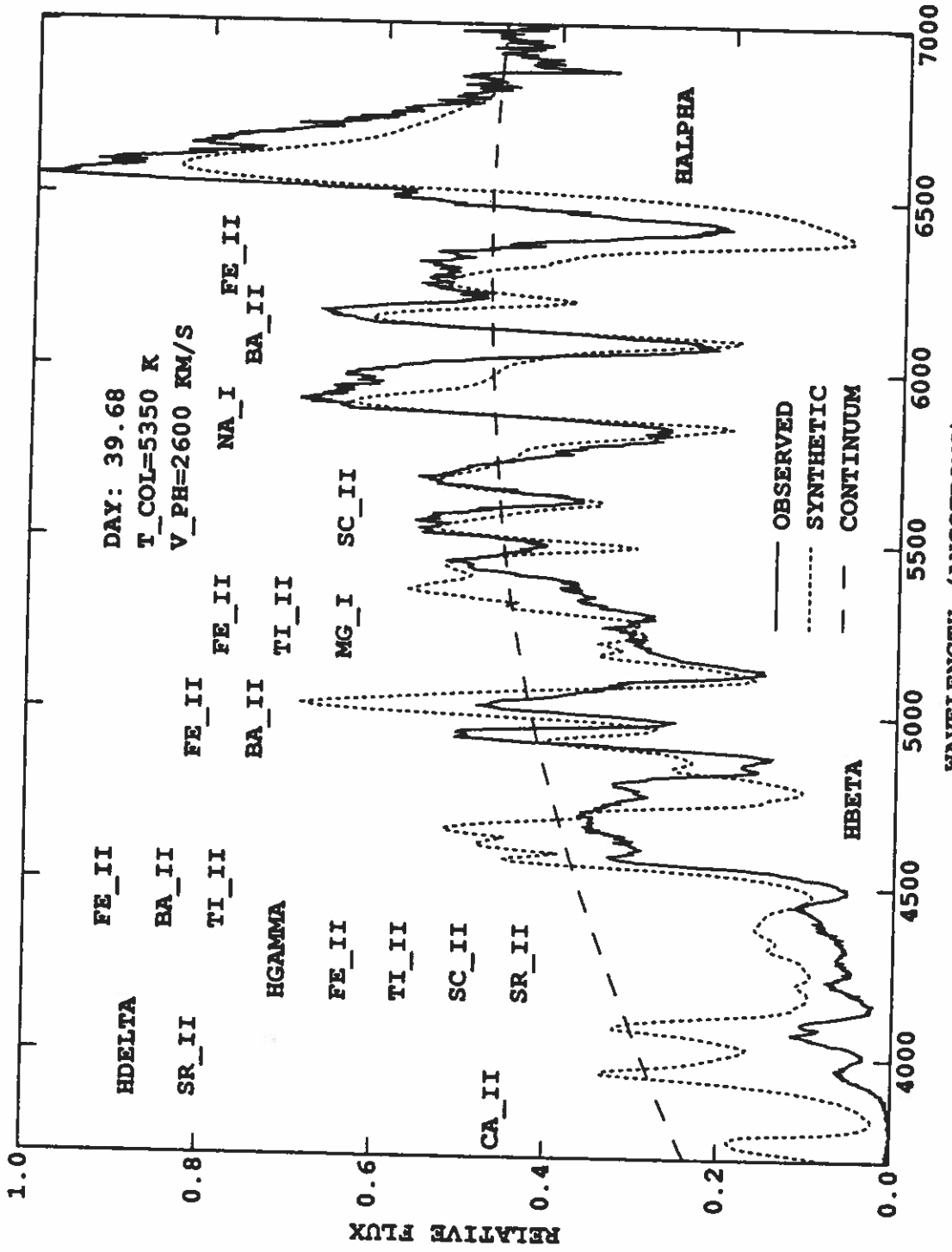

Fig. 31: *Observed and synthetic spectra for 8.99 Apr. 1987 U.T.*

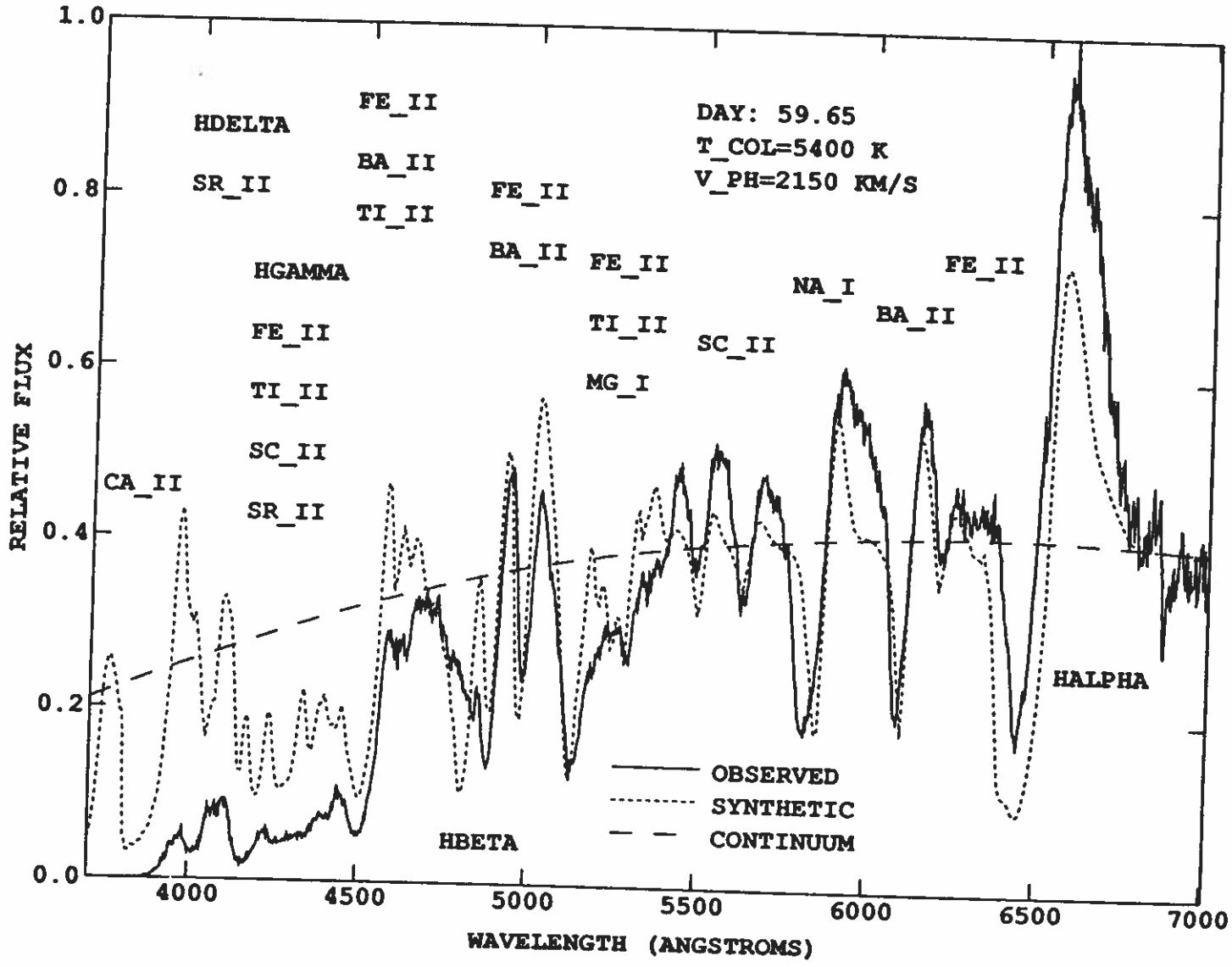

Fig. 32: *Observed and synthetic spectra for 23.97 Apr. 1987 U.T.*

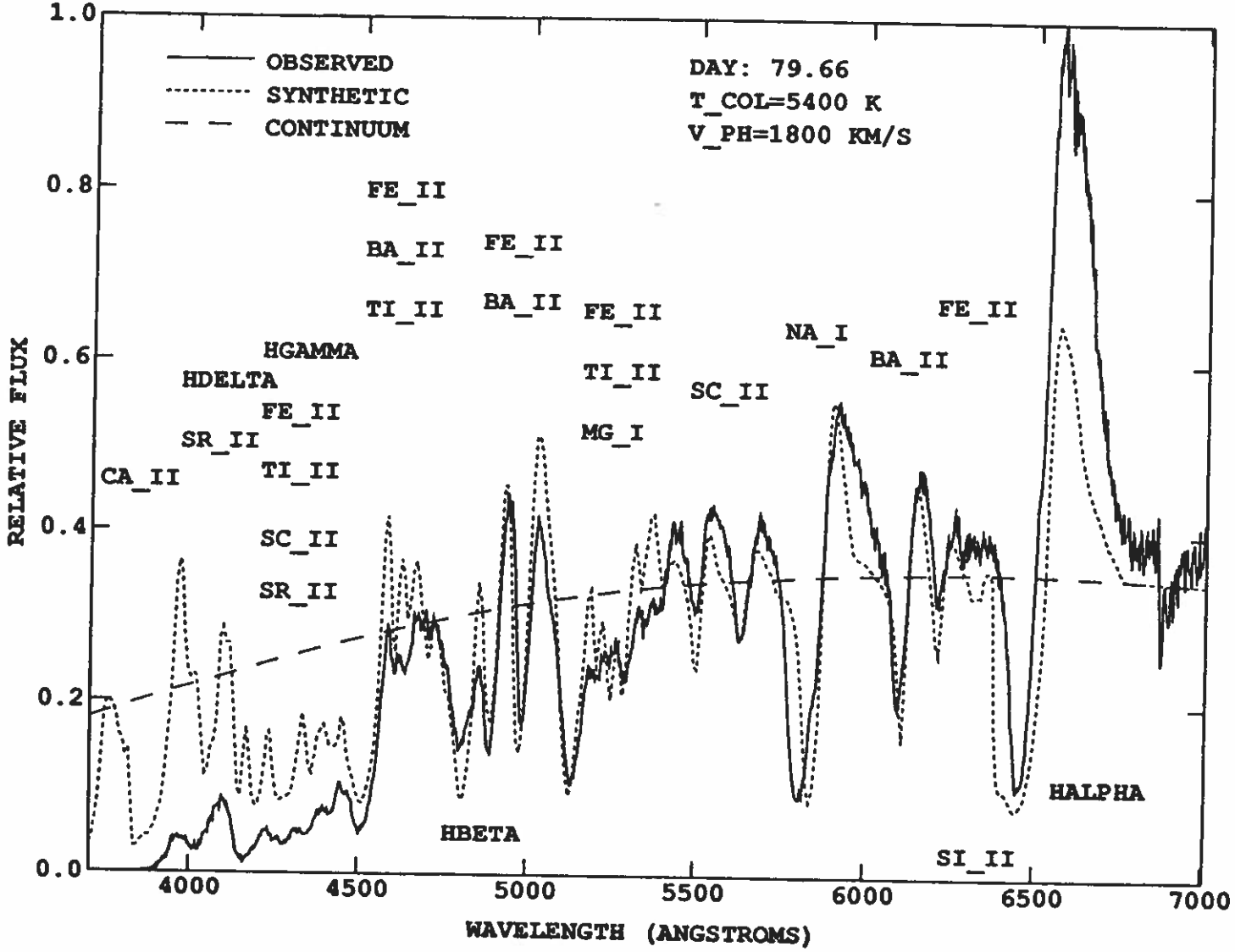

Fig. 33: *Observed and synthetic spectra for 13.97 May 1987 U.T.*

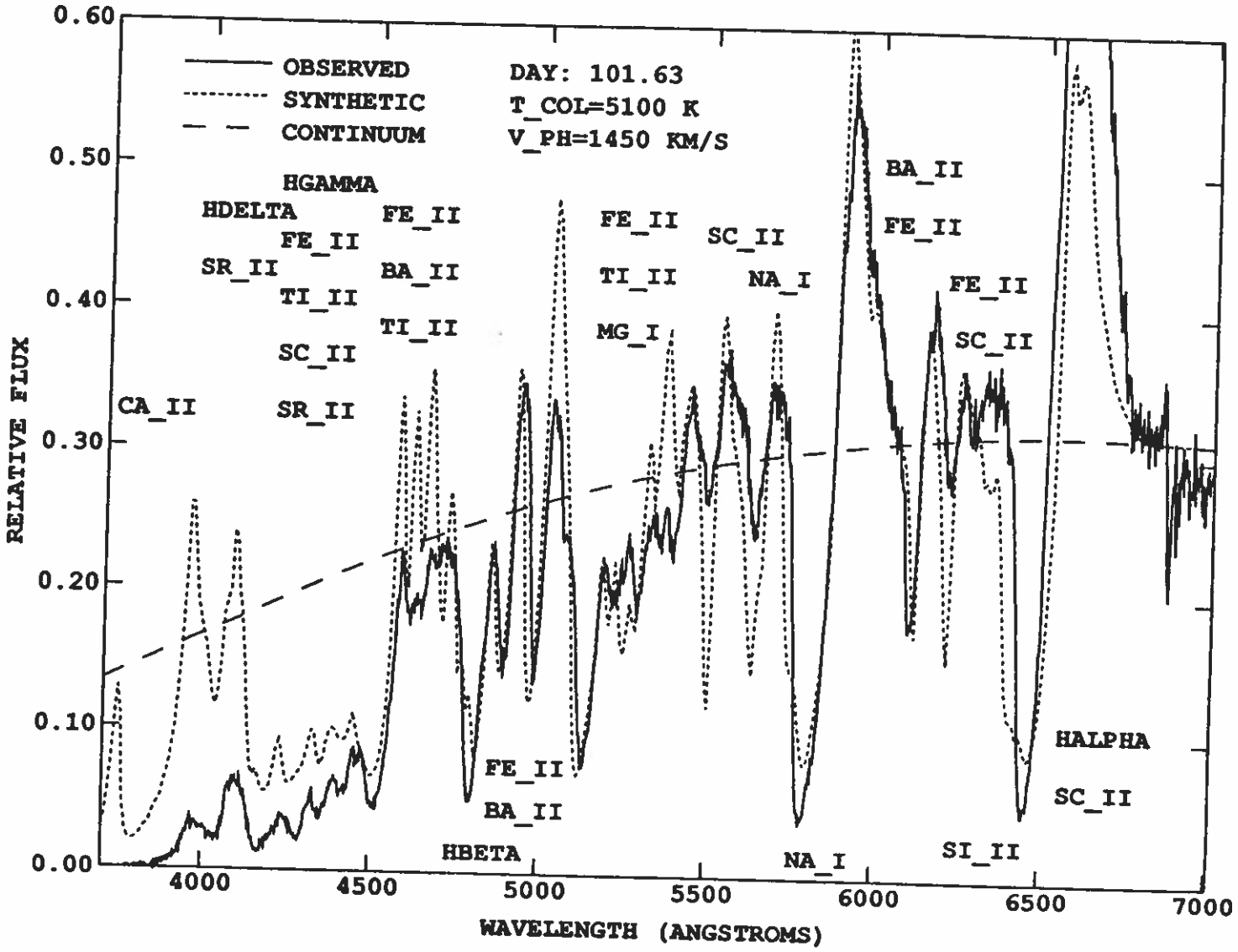

Fig. 34a: *Observed and synthetic spectra for 4.95 Jun. 1987 U.T.*

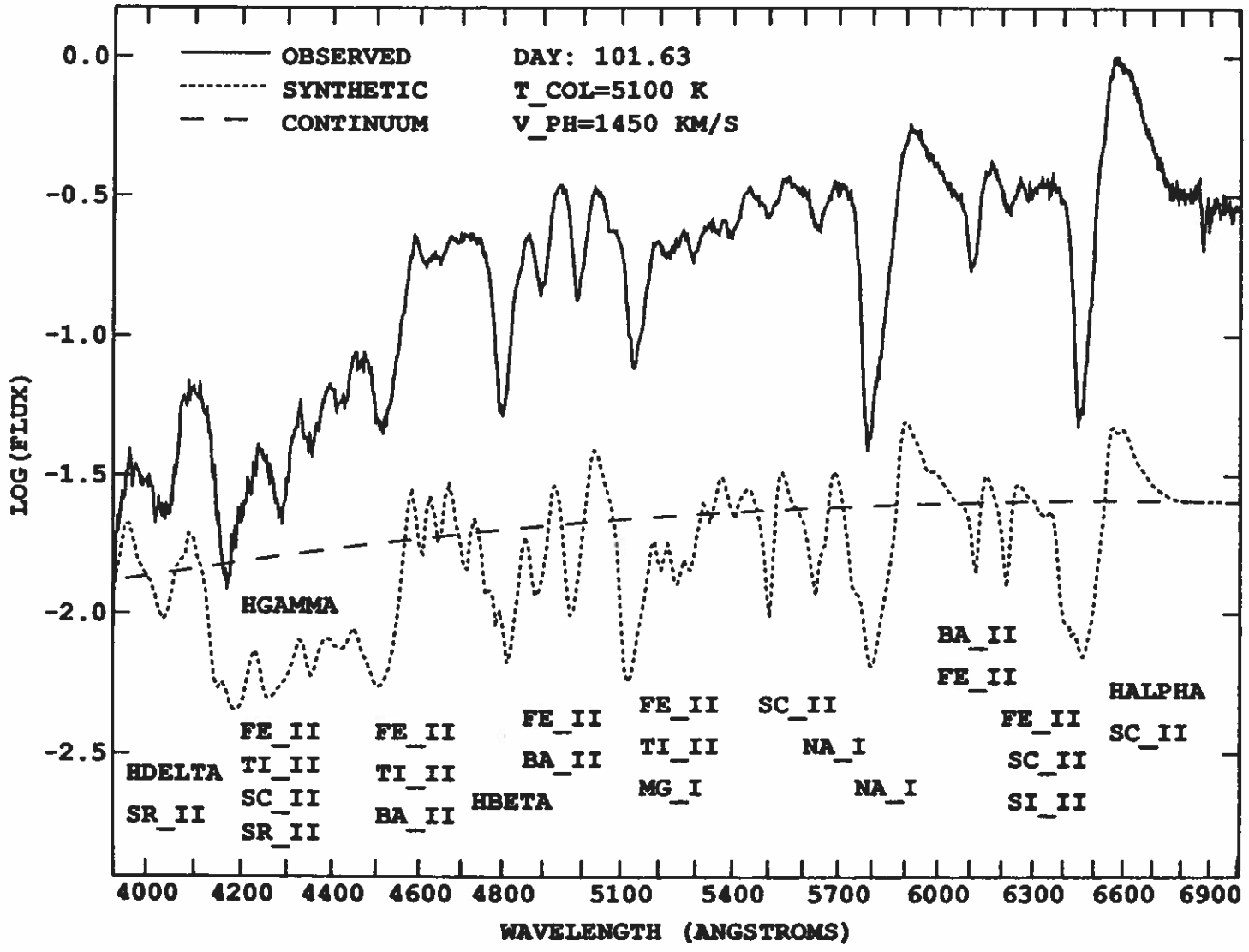

Fig. 34b: *Logarithmic plot of the spectra shown in Fig. 34a.*

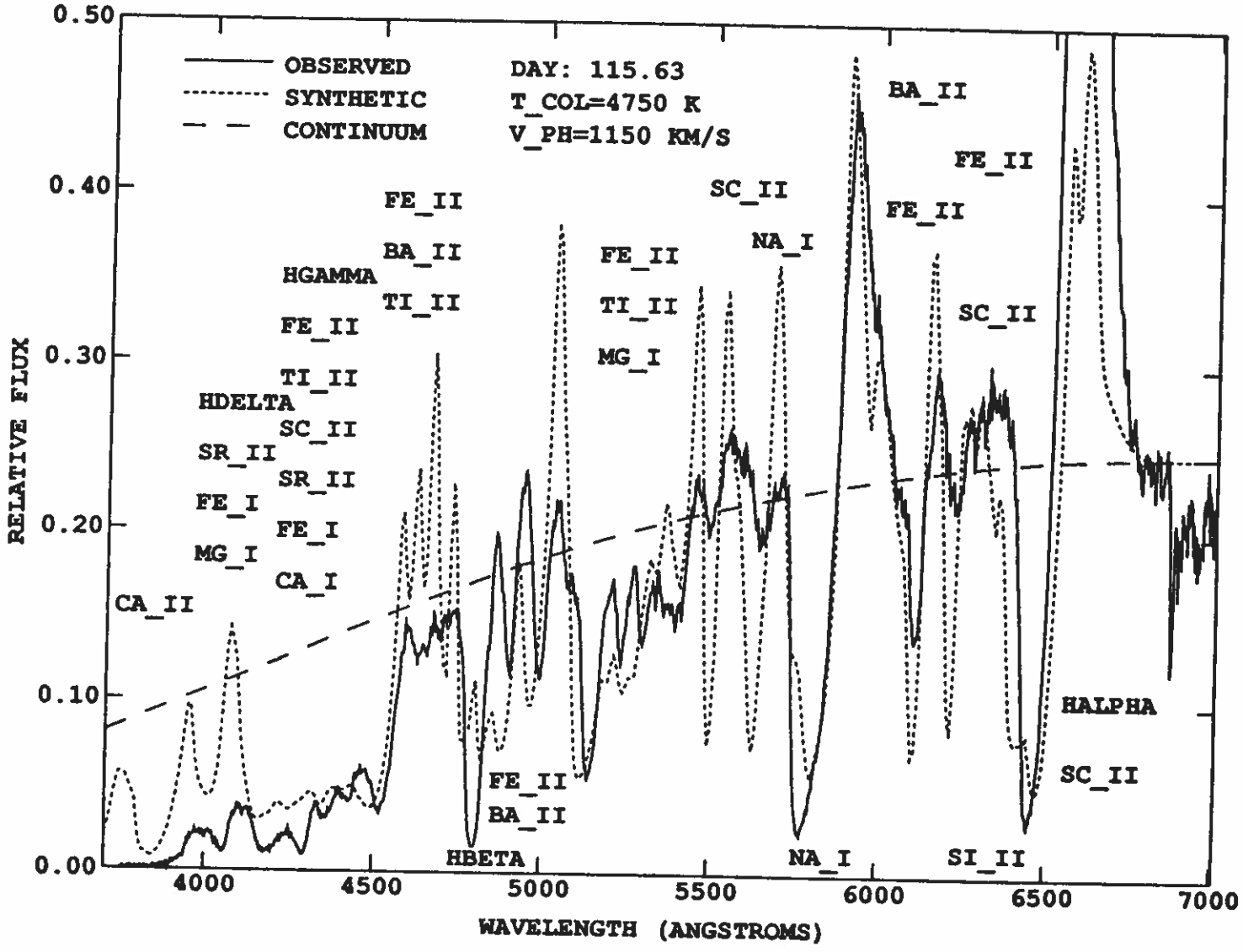

Fig. 35: *Observed and synthetic spectra for 18.95 Jun. 1987 U.T.*

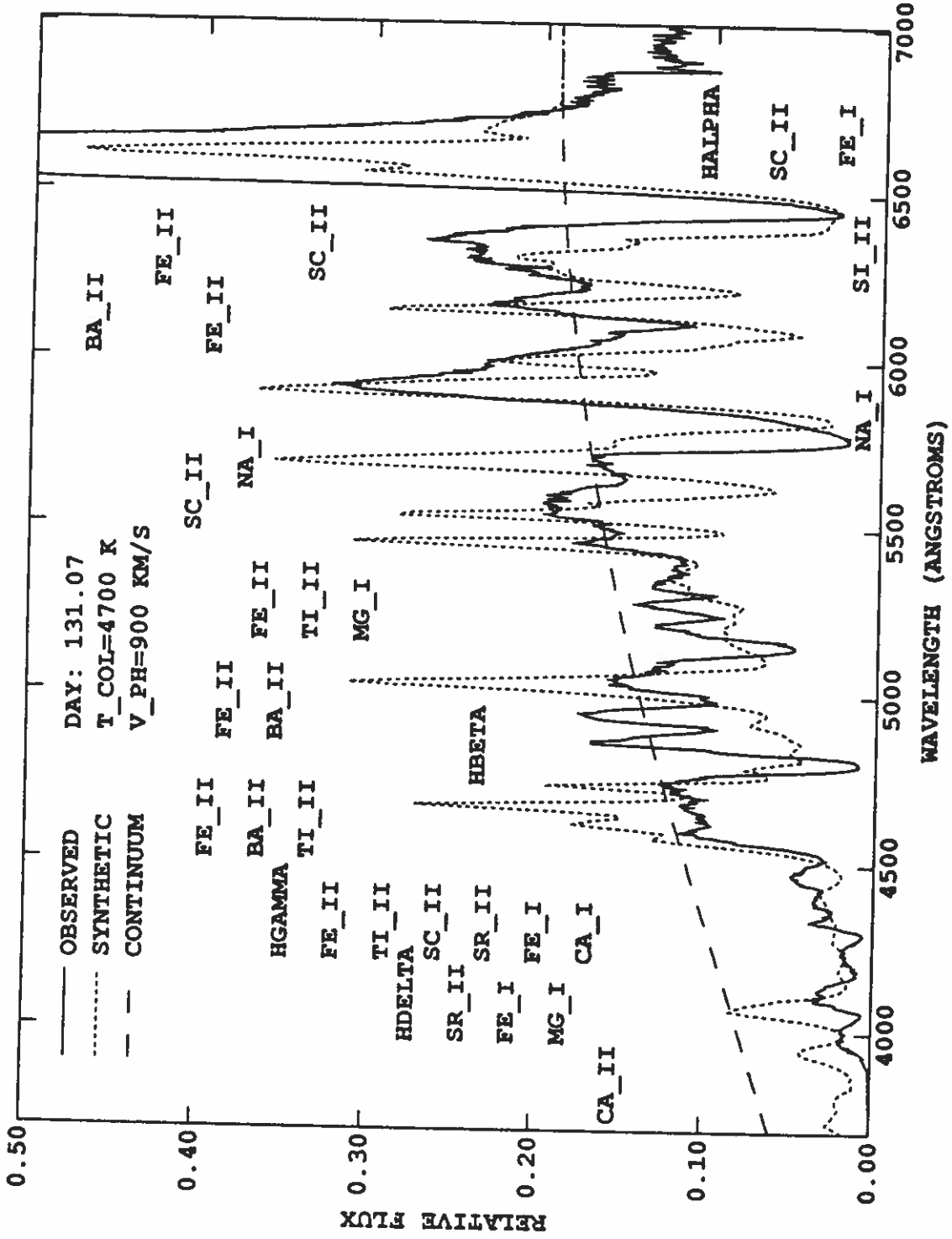

Fig. 36: *Observed and synthetic spectra for 4.39 Jul. 1987 U.T.*

blackbody curve through the first 134 days (Catchpole et al. 1987). Also shown in the figures is the synthetic blackbody continuum that would have emerged from the atmosphere if no line opacities had been included in the calculation. The synthetic spectra are reddened using $E(B-V) = 0.2$ and are given a global redshift corresponding to the LMC radial velocity of $270\,\mathrm{km\,s^{-1}}$. The photospheric velocities were obtained, as mentioned in § V*a*, using the photometric velocities as initial values for the photospheric velocity parameter and then adjusting this parameter for reasonable fits of the synthetic spectra to the observed spectra. The photospheric Sobolev optical depths were obtained as described in § V*b*. Above the photosphere, the optical depths were scaled with the empirical density profile which was extended to velocities above $10000\,\mathrm{km\,s^{-1}}$ by logarithmically extrapolating from the two outer density profile points. For all calculations the density profile was extended to high enough velocities that the computationally required outer cutoff for the atmosphere did not affect the calculated spectra.

Each spectrum figure shows the day the observed spectrum was taken, the color temperature appropriate for that day interpolated from the SAAO color temperatures, and the spectrum-fitted photospheric velocities (up to day 16) or the photometric velocities interpolated from the SAAO data (after day 16). In the figures, some of the synthetic line profile features are labeled by the ion designation of the ion whose line gives rise to the feature. The more important hydrogen line features are labeled by their line designations. These designations may label trough or emission features, or just a region of strong line blending where the designated ion or line contributes opacity; it is hoped that the figure context makes clear what the designations are labeling. The identification both on the figures and in the text of synthetic features is, of course, correct. It is believed that the identification of observed features implied by the fit of synthetic features to the observed features is for the most part correct; some identifications that cannot be made or are doubtful are discussed below.

Figure 24 shows the day 1.85 spectra. The observed spectrum is one of the earliest available; Menzies et al. (1987) report a spectrum from day 1.6, but it is similar to the day 1.85 CTIO spectrum. The synthetic line profiles are typical results of line formation with the pure scattering source function (see § III): see § IV for a discussion and examples of such line profiles. In the observed spectrum, five distinct line profiles are visible and are confidently identified: the Hα, Hβ, Hγ, Hδ (not labeled), and He I λ5876 line profiles. The Hδ line profile is greatly distorted by line blending with the Hγ line, and hydrogen, helium, and calcium lines blueward of the Hδ wavelength. The observed broad shallow trough feature blueward from the Hδ trough is due to blending of all the Balmer and other lines bluer than 4000 Å; in the synthetic spectrum calculation all Balmer lines down to 3660 Å were included to create a synthetic feature to fit the observed feature. The location and overall size of the synthetic features is consistent with the observed features. However, it is clear that at least the Hα and Hβ line profiles show net emission; the net emission from the Hα line is a characteristic feature of SN II spectra and, as discussed in § III, is not reproducable in an ES model calculation without assuming an *ad hoc* net line emission: i.e., line emission in excess of the pure scattering line emission.

All the observed distinct line profiles for day 1.85 have emission features that are blueshifted. The blueshifts are understandable if for all these lines

$$S(r) > I_{\mathrm{ph}} \tag{82}$$

for some sufficiently large large part of the atmosphere. Recalling equation (71), equation (82) immediately implies

$$I_{\mathrm{emergent}} = [S(r) - I_{\mathrm{ph}}]\left[1 - e^{-\tau(r)}\right] + I_{\mathrm{ph}} > I_{\mathrm{ph}}\ , \tag{83}$$

for $p < R$ and a CD velocity surface region that is above the photosphere. Recall from § IV that the projection of the photosphere is called the photodisk. Equation (83) shows that the total flux emergent from the photodisk at wavelengths blueward of the line center wavelength can exceed the photospheric flux. Whether there is an enhancement or a diminishment of photodisk flux relative to the photospheric flux at given wavelength depends on the variation of $S(r)$ and $\tau(r)$ with radius and how much of the photodisk region of the CD velocity surface corresponding to the given wavelength is above the photosphere. At wavelengths where an enhancement occurs, no absorption feature can form in the line profile and the line profile emission feature will be larger than just photospheric flux plus limb emission flux. Photodisk flux redward of the line center wavelength is always just the photospheric flux since all the redshifted photodisk

line emission is occulted. Thus, redward of line center wavelength the line profile is formed by just the limb emission added to the photospheric flux. Therefore, one has a stronger blue or red wing to the line profile emission feature depending on whether photodisk flux enhancement or diminishment occurs blueward of the line center wavelength. For a single line with a pure scattering source function in an atmosphere with no continuous opacity, there is never any enhancement since $S(r)$ is always less than $I_{\rm ph}$; this can be seen from equation (30) and equation (31) with ϵ and G set to zero. Given that the inequality of equation (83) holds out to some sufficient radius, it is easy to see that there is a tendency for the photodisk flux enhancement and thus the line profile emission feature to increase in the blueward direction. This is because the annular region of the photodisk region of the CD velocity surface that is above the photosphere increases as the corresponding wavelength is decreased from the line center wavelength to the photospheric wavelength. Blueward of the photospheric wavelength this effect is, of course, not operative. If source function and/or optical depth are decreasing with radius, then there is also a strong tendency for the enhancement to decrease and perhaps become a diminishment with decreasing wavelength. How the increasing and decreasing tendencies interact to form a line profile depends on the exact parameters of the system. It is, however, clear that a blueshifted emission feature and an even further blueshifted trough feature are both possible for in a line profile. This picture of line profile formation probably explains the blueshifted maxima and blueshifted trough features in the observed day 1.85 line profiles.

Figure 25 shows the day 3.71 spectra. The color temperature has fallen by 4200 K since day 1.85 and this decline correlates with the obvious decline in the slope of the observed continuum. Note that the fit of the synthetic continuum level is not very good; the observed spectrum is stronger in the B band and weaker in the V band relative to the synthetic continuum. Except for the Hα trough, the synthetic spectrum features appear weak compared to the observed features. However, the relative sizes of the larger features are roughly consistent. Both the observed and synthetic He I λ5876 line have vanished due to falling temperature. The Ca II K (3934 Å) and H (3968 Å) lines give rise to a single line profile due to line blending; these lines now dominate the blue end of both spectra. Although the synthetic spectrum does not well reproduce it, the trough feature at about 4400 Å should be due mainly to a blend of Fe II lines. The synthetic spectrum predicts that Fe II line blend features should appear in the 5000–5300 Å region; the observed spectrum is not consistent with this prediction in any obvious way.

The narrow emission feature centered at about 5200 Å in the day 3.71 observed spectrum is spurious. This feature which is seen in all the CTIO spectra from day 3.71 to day 7.72 is due a detector flaw that was corrected after day 8.71 (Phillips 1990). Well-displayed SN 1987A spectra from the days 3.71–7.72 epoch that have been published by other observers (e.g., Cropper et al. 1988; Hearnshaw et al. 1988) show no remarkable behavior at about 5200 Å.

Figure 26 shows the day 5.76 spectra which are similar to the day 3.71 spectra. The synthetic spectrum features are generally weak compared to the observed features, but the relative sizes of features are consistent between the two spectra. In the synthetic spectrum, the Hδ trough has all but vanished due to the strength of the Ca II K and H lines. The synthetic spectrum Fe II line blends in the regions about 4400 Å and 5100 Å are now more clearly identifiable with the observed features.

Figure 27 shows the day 8.71 spectra. The blue end of the observed spectrum now shows the severe ultraviolet deficiency relative to blackbody fits of the U to L magnitudes (Catchpole et al. 1987) that persists throughout the photospheric phase of the supernova. The TE-predicted optical depths show Ti II lines making a significant contribution to the line features near 4500 Å. Due to line blending no individual Ti II line can ever be identified in the spectra. However, the cumulative effect of the Ti II lines significantly improve the fit of the synthetic spectra to the observed spectra from this day on. The line trough feature near 5750 Å has been identified as due to the Na I λ5892 doublet. As discussed in § V*b*, to fit this and all later observed spectra up until day 131, the optical depths of the Na I λ5892 doublet have been increased from the solar-composition TE-predicted values. Once again, it should be kept in mind that a radioactive nonthermal effect may cause the He I λ5876 line to contribute to the line profile attributed to the Na I λ5892 doublet. However, significant He I λ5876 line contribution is more likely after about day 76.

Figure 28 shows the day 14 spectra. In the B band region, the observed spectrum is becoming deficient relative to the synthetic spectrum. This deficiency persists at least until day 131. The cause of the deficiency is probably line blanketing in the supernova atmosphere due to thousands of weak lines. Including more weak lines in the synthetic spectra calculations should improve the fits of the synthetic spectra. For this and all later observed spectra up until day 102, the Ba II λ6142 optical depths have been increased from

the predicted values in order to fit the observed line profile just redward of 6000 Å. Since the other Ba II line optical depths increase according to equation (66) when the Ba II λ6142 line optical depth increases, they now become more important in the synthetic spectra. In particular, the Ba II $\lambda\lambda$4554 and 4934 lines now contribute significantly in the synthetic spectra. In the synthetic spectrum for day 14, strong Fe II lines and the Ba II λ4934 line are mainly responsible for suppressing the Hβ emission feature. This suppression is present, but less severe in the observed spectrum. Line profiles due mainly to the Sc II $\lambda\lambda$5527 and 5661 lines are now appearing near 5500 Å.

Figure 29 shows the day 20 spectra. The most notable feature of this figure is the poor fit of the synthetic spectrum Hβ line profile trough to the observed features. In the observed spectrum, some sort of emission feature has formed where the Hβ trough should be. This emission feature is probably a Bochum feature (Phillips and Heathcote 1989). From about day 20 to about day 80 this emission feature obscures the location of the observed Hβ trough. Bochum features and the Bochum event are discussed below along with Figure 30. Both the predicted and fitted metal line optical depths, which had been increasing before day 20, have on day 20 reached the level at which they roughly remain until about day 100 (see Figs. 22a–22c and 23).

Figure 30 shows the day 31 spectra. The observed spectrum shows two satellite features on the Hα line profile: one feature is blueshifted and the other redshifted from the Hα line center wavelength. These features and similar features associated with other SN 1987A spectrum line profiles have been collectively called the Bochum event after the university, Ruhr-Universität Bochum, of some of the discoverers (see Cristiani et al. 1987; Hanuschik and Dachs 1987). The Bochum event is well described and discussed by Phillips and Heathcote (1989); their discussion is followed here. The blue and red Hα features appeared about day 20 and day 22, respectively. The features are most prominent about day 30 and then fade to undetectability on about day 111. They are most probably emission features superimposed on the Hα line profile rather than absorption features cutting into it. The velocities of the peaks of the Bochum features track the photospheric velocity. Bochum features identified in other line profiles are usually less prominent and for the most part only one of the red or blue features is noticable. These other lines profiles with identified Bochum features are the Hβ, Pα, Pβ, Brα, Brβ, Brγ, Brδ, Brϵ, and Na I λ5892 doublet line profiles. As mentioned just above and in § V*a*, a blue Bochum emission feature is the probable cause of the distortion of the Hβ trough feature seen in observed spectra in the day 20 to day 80 epoch. The most probable cause of the Bochum event is some asymmetry in the supernova. For example, Lucy (1988) suggests that the Bochum event might have arisen from an aspherical diffusion of the radioactive energy. Aside from the Bochum features, the synthetic spectrum for day 31 is a reasonable fit to the observed spectrum.

In the day 30 to day 80 epoch, the observed and synthetic spectra, shown in Figures 30–33, are reasonably consistent. The Bochum features fade through this epoch. By day 80 the Hβ line profile trough is identifiable again (see Fig. 33). Starting from sometime after day 40 and carrying on through day 131, the observed Hα emission feature gains in height relative to the the local continuum.

An interesting feature of the synthetic spectra after day 30 is the appearance of inflection points on the blue sides of the Na I λ5892 and Hα troughs. These inflection points are due to the flattening of the empirical density profile in the 6900–8400 km s^{-1} velocity range (see Fig. 18b). The inflection points only appear when the Na I λ5892 and Hα lines become unsaturated in this velocity range: i.e., when their optical depths for the 6900–8400 km s^{-1} velocity range satisfy $\tau \lesssim 1$. When $\tau >> 1$, a line is saturated and the line emission is determined only by the line source function (see the discussion of Fig. 3 in § IV). For strong lines, the inflection points only appear on the blue sides of trough features since the red sides are largely formed by line transfer through the photodisk regions of CD velocity surfaces where the line is mostly saturated. The density profile flattening has less evident effect on weak lines partially due to line blending which tends to distort out of recognition any narrow features due to a single line. However, the lack of evident effect is mainly due to the fact that the photosphere is larger when the weak lines have any significant optical depth in the 6900–8400 km s^{-1} velocity range. The larger the photosphere relative to any opacity shell, the larger the wavelength band from which photospheric flux can be removed by the opacity shell. If this wavelength band is comparable in breadth to a trough feature, then the opacity shell will tend not to cause any distinct narrow features in that trough feature. Since there are no features in the observed spectra that are obviously similar to the inflection points in the synthetic spectra, the real supernova density profile probably does not have a flattened region corresponding to the flattened region in the empirical density profile.

Figure 34a shows the day 102 spectra. The relative flux scale has been truncated and the lower part

expanded in this and subsequent plots in order to maintain a good display of the spectra. The fit of the synthetic to the observed spectrum is still reasonably good. However, the synthetic spectrum line profiles due mainly to the Sc II $\lambda\lambda$5527 and 5661 lines are relatively too strong. In addition, the synthetic Ba II λ6142 line profile required no increase in strength from the solar-composition TE prediction on this day; this actually means a bad fit if one assumes that barium abundance is enhanced relative to solar abundance by an order of magnitude. The cause of the increasing strength of the solar-composition TE-predicted metal line optical depths was discussed in § V*b*. An interesting feature in the synthetic spectrum for day 102 is the small trough feature due to the Sc II λ6605 line appearing on top of the Hα emission. This feature also appears in the day 116 and day 131 synthetic spectra. There is too much noise on top of the observed Hα emission features to tell if corresponding trough features are present.

Figure 34b, also showing the spectra for day 102, is presented as an example of a logarithmic plot. The displacement of the observed and synthetic spectra is arbitrary. Logarithmic plots are useful for displaying spectra where the features vary greatly in size. For instance, Figure 34b gives a more equal emphasis to the B and V bands than does Figure 34a. As can also be seen, logarithmic plots emphasize trough features and de-emphasize emission features. The different emphases of logarithmic plots can be useful in recognizing some spectrum features.

Figures 35 and 36 show the spectra for days 116 and 131, respectively. In the synthetic spectra, the metal line features have increased in strength and are often much stronger than in the observed spectra. Although, as discussed in § III, determinations of the absolute sizes of optical depths from comparisons of the absolute sizes of synthetic and observed line profile features cannot be expected to be very accurate, the great degree of difference between the sizes of the synthetic and observed line profile features for these days strongly suggests that the solar-composition TE-predicted optical depths are too large. It is true that the increase in metal line strength has helped to fit the continuum level in the region blueward of 4500 Å; however, the correlation of synthetic and observed features that is present in this region on day 102 (see Fig. 34a) and earlier is not so evident for the later days. Due to line blending, there is no way to tell if lines of the neutral ions, such as Mg I, Ca I, and Fe I, are as significant in the observed spectra as their solar-composition TE-predicted optical depths suggest they should be. The only neutral metal ion line profile, other than the Na I λ5892 doublet profile, that is clearly seen in a synthetic spectrum is the Fe I λ6678 line profile and it is not present in the corresponding observed spectrum (see Fig. 36); of course, net line emission from the Hα line may have obliterated any Fe I λ6678 line features in the observations. Because of the above arguments, it is believed that the solar-composition TE-predicted optical depths for the period after about day 100 are less accurate than for earlier times. Therefore, judgements about the relative strengths of the Na I λ5892 doublet and Ba II λ6142 line have not been drawn for the post-day-100 epoch (see § V*b*).

d) Summary

Several remarks summarize the SN 1987A photometry and optical spectra analysis presented in this section. For the period from about day 16 to about day 100, it seems probable that the photometric radius is close to being the true photospheric radius; earlier than day 16, the photometric radius is too small. The empirical density profile determined from the photometry is in rough qualitative agreement with Woosley's model 10H density profile. The total ejecta kinetic energy determined from the photometry and a fit of total mass to the model 10H mass agrees within 10 % with the total kinetic energy of model 10H. The ES model and the solar-composition TE-predicted line optical depths give synthetic spectra that are in rough qualitative agreement with the observed spectra; the agreement becomes poorer after day 100. However, the observed line profiles identified as due to the Na I λ5892 doublet and the Ba II λ6142 line are distinctly stronger than predicted; NLTE effects or non-solar abundances are needed to explain these line profiles. This analysis uses many simplifying assumptions and reaches mainly qualitative or weak conclusions. However, the results obtained can be used as benchmarks to which the more advanced and detailed analyses can be compared.

ACKNOWLEDGEMENTS

We thank the Hebrew University of Jerusalem for giving us the opportunity for discussions with colleagues and friends at the Jerusalem Winter School. We also thank our directors and editors Tsvi Piran and

Craig Wheeler for their many services to the Winter School and their patience in waiting for this article. Part of the article was written while we were guests at the Institut für Astronomie und Astrophysik der Universität München. The research for the article was supported by the University of Oklahoma and NSF grant AST 8620310.

REFERENCES

Allen, C. W., 1973, in Astrophysical Quantities (London: The Athlone Press)
Bailey, J., 1988, *Astronomical Society of Australia: Proceedings*, ed. R. X. McGee, Vol. **7**, No. 4, p. 405.
Benz, W., and Thielemann, F.-K., 1990, in Ap. J. (Letters), 348, L17
Bionta, R. M., et al. 1987, in Phys. Rev. Letters, 58, 1494
Bodenheimer, P., and Woosley, S. E., 1983, in Ap. J., 269, 281
Branch, D., 1977, in M.N.R.A.S., 179, 401
_____. 1979, in M.N.R.A.S., 186, 609
_____. 1980, in Supernova Spectra, ed. R. Meyerott and G. H. Gillespie (New York: American Institute of Physics), p 39.
_____. 1987a, in Ap. J. (Letters), 316, L81
_____. 1987b, in Ap. J. (Letters), 320, L23
Branch, D., Buta, R., Falk, S. W., McCall, M. L., Sutherland, P. G., Uomoto, A., Wheeler, J. C., and Wills, B. J., 1982, in Ap. J. (Letters), 252, L61
Branch, D., Doggett, J. B., Nomoto, K., and Thielemann, F.-K. 1985, in Ap. J., 294, 619
Branch, D., Falk, S. W., McCall, M. L., Rybski, P., Uomoto, A., and Wills, B. J., 1981, in Ap. J., 244, 780
Branch, D., Lacy, C H., McCall, M. L., Sutherland, P. G., Uomoto,A., Wheeler, J. C., and Wills, B. J., 1983, in Ap. J., 270, 123
Branch, D., and Patchett, B., 1973, in M.N.R.A.S., 161, 71
Cameron, A., 1982, in Essays on Nuclear Astrophysics, ed. C. Barnes, D. Clayton, D. Schramm (Cambridge: Cambridge University Press), p 23.
Castor, J. I., 1970, in M.N.R.A.S., 149, 111
Castor, J. I., and Nussbaumer, H., 1972, in M.N.R.A.S., 155, 293
Catchpole, R. M., et al. 1987, in M.N.R.A.S., 229, 15P
Catchpole, R. M., et al. 1988, in M.N.R.A.S., 231, 75P
Chevalier, R. A., and Klein, R. I., 1978, in Ap. J., 219, 994
Chevalier, R. A., and Soker, N., 1989, in Ap. J., 341, 867
Clayton, D. D., 1983, in Principles of Stellar Evolution and Nucleosynthesis (Chicago: The University of Chicago Press)
Colgate, S. A., and McKee, C., 1969, in Ap. J., 157, 623
Cristiani, S., Gouiffes, C., Hanuschik, R. W., Magain, P., 1987, *IAU Circ.*, No. 4350.
Cropper, M., Bailey, J., McCowage, J., Cannon, R. D., Couch, W. J., Walsh, J. R., Straede, J. 0., and Freeman F., 1988, in M.N.R.A.S., 231, 695
Dearborn, D. S. P., Schramm, D. N., Steigman, G., and Truran, J. 1989, in Ap. J., 347, 455
Dufour, R. J., Shields, G. A., and Talbot, R. J., Jr., 1982, in Ap. J., 252, 461
Eastman, R. G., and Kirshner, R. P., 1989, in Ap. J., 347, 771
Elias, J. H., Gregory, B., Phillips, M. M., Williams, R. E., Graham, J. R., Meikle, W. P. S., Schwartz, R. D., and Wilking, B. 1988, in Ap. J. (Letters), 331, L9
Elliot, K. H., Goudis, C., Meaburn, J., and Tebbutt, N. J., 1977, in Astr. Ap., 55, 187
Feast, M. W., 1984, in M.N.R.A.S., 221, 51P
Feldt, A. N., 1979, in Proc. Okla. Acad. Sci., 59, 94
_____. 1980, Ph.D. thesis, University of Oklahoma.
Graham, J. R., 1988, in Ap. J. (Letters), 335, L53
Hamann, W.-R., 1981, in Astr. Ap., 93, 353
Hanuschik, R. W., and Dachs, J., 1987, in Astr. Ap., 182, L29
Harkness, R. P., and Wheeler, J. C., 1989, McDonald Observatory Preprint, No. 031.
Hearnshaw, J. B., McIntyre, V. J., and Gilmore, A. C., 1988, in J. Ap. Astr., 9, 93

Hirata, K., et al. 1987, in Phys. Rev. Letters, 58, 1490
Höflich, P., 1988, *Astronomical Society of Australia: Proceedings*, ed. R. X. McGee, Vol. **7**, No. 4., p. 434.
Huo, J., Hu, D., Zhou, C., Han, X., Hu, B., and Wu, Y., 1987, in Nuclear Data Sheets, 51, 1
Hummer, D. G., 1969, in M.N.R.A.S., 145, 95
Hummer, D. G., and Rybicki, G. B., 1985, in Ap. J., 293, 258
Jeffery, D. J., 1987, in Nature, 329, 419
_____. 1988, Ph.D. thesis, McMaster University.
_____. 1989, in Ap. J. Suppl., 71, 951
_____. 1990, in Ap. J., 352, 267
Jeffery, D. J., and Sutherland, P. G., 1985, in Ap. Sp. Sci., 109, 277
Jones, A., 1987, *IAU Circ.*, No. 4340.
Karovska, M., Koechlin, L., Nisenson, P., Papaliolios, C., and Standley, C., 1988, *IAU Circ.*, No. 4604.
Karovska, M., Koechlin, L., Nisenson, P., Papaliolios, C., and Standley, C., 1989, in Highlights in Astronomy, Vol. 8, ed. D. McNally (Dordrecht: Kluwer), p 193.
Karp, A. H., Lasher, G., Chan, K. L., and Salpeter, E. E., 1977, in Ap. J., 214, 161
Kirshner, R. P., and Kwan, J., 1974, in Ap. J., 193, 27
Laney, C. D., and Stobie, R. G., 1986, in M.N.R.A.S., 222, 449
LeBlanc, J. M., and Wilson, J. R., 1970, in Ap. J., 161, 541
Lucy, L. B., 1971, in Ap. J., 163, 95
_____. 1988, in Supernova 1987A in the Large Magellanic Cloud, ed. M. Kafatos and A. G. Michalitsianos (Cambridge: Cambridge University Press), p 323.
Mazzali, P. A., 1988, in *ESA SP-281*, Vol. **2**, *A Decade of UV Astronomy with the IUE Satellite*, (Noordwijk: ESA), p. 163.
_____. 1989, Ph.D. thesis, University of California, Los Angeles.
McCall, M. L., 1985, in Supernovae as Distance Indicators, ed. N. Bartel (Berlin: Springer-Verlag), p 48.
McCall, M. L., Reid, N., Bessell, M. S., and Wickramasinghe, D. T. 1984, in M.N.R.A.S., 210, 839
McNaught, R. H., 1987a, *IAU Circ.*, No. 4316.
McNaught, R. H., 1987b, *IAU Circ.*, No. 4389.
Méndez, M., Clocchiatti, A., Benvenuto, O. G., Feinstein, C., and Marraco, H. G., 1988, in Ap. J., 334, 295
Menzies, J. W. et al. 1987, in M.N.R.A.S., 227, 39P
Mihalas, D., 1978, in Stellar Atmospheres (San Francisco: W. H. Freeman and Company)
Natta, A., and Beckwith, S., 1986, in Astr. Ap., 158, 310
Nomoto, K., Thielemann, F.-K., and Yokoi, K., 1984, in Ap. J., 268, 644
Olson, G. L., 1982, in Ap. J., 255, 267
Panagia, N., 1985, in Supernovae as Distance Indicators, ed. N. Bartel (Berlin: Springer-Verlag), p 14.
Patchett, B., and Branch, D., 1972, in M.N.R.A.S., 158, 375
Pauldrach, A., Puls, J., and Kudritzki, R. P., 1986, in Astr. Ap., 164, 86
Phillips, M. M., 1979, in Ap. J. Suppl., 39, 377
_____. 1990, private communication.
Phillips, M. M., and Heathcote, S. R., 1989, in Pub. A.S.P., 101, 137
Phillips, M. M., Heathcote, S. R., Hamuy, M., and Navarrete, M. 1988, in A. J., 95, 1087
Puls, J., and Hummer, D. G., 1988, in Astr. Ap., 191, 87
Rybicki, G. B., 1970, in Spectrum Formation in Stars with Steady-State Extended Atmospheres, ed. H. Groh and P. Wellmann, NBS Spec. Publ. No. 332 (Washington: U.S. Government Printing Office), p 87.
Rybicki, G. B., and Hummer, D. G., 1978, in Ap. J., 219, 654
Schwarz, H. E., 1987, in ESO Workshop on the SN 1987 A, ed. I. J. Danziger (Garching: ESO), p 167.
Schwarz, H. E., and Mundt, R., 1987, in Astr. Ap., 177, L4
Shelton, I., 1987, *IAU Circ.*, No. 4316.
Shobbrook, R. R., and Visvanathan, N., 1987, in M.N.R.A.S., 225, 947
Sobolev, V. V., 1947, *Moving Envelopes of Stars* (Leningrad: Leningrad State University) (English transl. S. Gaposchkin [Cambridge: Harvard University Press, 1960]).
Swartz, D. A., Harkness, R. P., and Wheeler, J. C., 1989, in Nature, 337, 439
Symbalisty, E. M. D., 1984, in Ap. J., 285, 729

_____. 1985, in Numerical Astrophysics, ed. J. M. Centrella, J. M. LeBlanc and R. L. Bowers (Boston: Jones and Bartlett Publishers, Inc.), p 453.
Wagoner, R. V., 1981, in Ap. J. (Letters), 250, L65
Wagoner, R. V., 1982, in Supernovae: A Survey of Current Research, ed. M. J. Rees and R. J. Stoneham (Dordrecht: D. Reidel Publishing Company), p 253.
Walker, A. R., and Suntzeff, N. B., 1990, in Pub. A.S.P., 102, 131
Wheeler, J. C., Harkness, R. P., and Barkat, Z., 1988, in Atmospheric Diagnostics of Stellar Evolution: Chemical Peculiarity, Mass Loss, and Explosion, ed. K. Nomoto (Berlin: Springer-Verlag), p 305.
Wheeler, J. C., Harkness, R. P., Barkat, Z., and Swartz, D. A., 1986, in Pub. A.S.P., 98, 1018
West, R. M., Lauberts, A., Jorgensen, H. E., and Schuster, H. E. 1987, in Astr. Ap., 177, L1
Wiese, W. L., and Fuhr, J. R., 1975, in J. Phys. Chem. Ref. Data, 4, 263
Wiese, W. L., Smith, M. W., and Glennon, B. M., 1966, in *NSRDS–NBS 4*, Vol. **1**, *Atomic Transition Probabilities—Hydrogen through Neon*, (Washington, DC: U.S. Government Printing Office).
Wiese, W. L., Smith, M. W., and Miles, B. M., 1969, in *NSRDS–NBS 22*, Vol. **2**, *Atomic Transition Probabilities—Sodium through Calcium*, (Washington, DC: U.S. Government Printing Office).
Woosley, S. E., 1988, in Ap. J., 330, 218
Woosley, S. E., Pinto, P. A., and Ensman, L., 1988, in Ap. J., 324, 466
Younger, S. M., Fuhr, J. R., Martin, G. A., and Wiese, W. L., 1978, in J. Phys. Chem. Ref. Data, 7, 495
Zoltowski, F., 1987, *IAU Circ.*, No. 4389.

FIGURE LEGENDS

Fig. 1: *Schematic representation of the ES model of a supernova.*

Fig. 2: *Typical P Cygni line profile.*

Fig. 3: *Line profiles for varied photospheric optical depth* $\tau_{\rm ph}$.

Fig. 4: *Line profiles for varied inverse power-law index* n.

Fig. 5: *Line profiles for various combinations of ES model parameters.*

Fig. 6: *Line profiles for a detached atmosphere.*

Fig. 7: *Line profiles for an atmosphere with a density peak.*

Fig. 8: *Line profiles for a geometrically thin atmosphere.*

Fig. 9: *Line profiles for an oblate axisymmetric ellipsoidal ES model with varied* (c/a)*: i.e., varied ratio of the symmetry semiaxis to the perpendicular semiaxis.*

Fig. 10: *Synthetic spectra with two lines both with photospheric optical depth 10 and with varied line center wavelength separation WS.*

Fig. 11: *Synthetic spectra with two lines with photospheric optical depths 10 and 3 and with varied line center wavelength separation WS.*

Fig. 12: *Synthetic spectra with five lines all with photospheric optical depth 10 and with varied line center wavelength separation WS.*

Fig. 13: *SAAO SN 1987A bolometric luminosity for days* 1.50–257.65.

Fig. 14a: *SAAO SN 1987A color temperature for days* 1.50–257.65.

Fig. 14b: *SAAO SN 1987A color temperature for days* 16.45–257.65.

Fig. 15: *SAAO SN 1987A photometric radius and a displaced power-law fit radius for days* 1.50–257.65.

Fig. 16: *SAAO SN 1987A photometric velocity for days* 1.50–257.65, *spectrum-fitted photospheric velocity for days* 1.85–131.07 *(merges with the photometric velocity after day 16), and various line velocities.*

Fig. 17: *Empirical opacity evolution for SN 1987A for days* 1.50–257.65.

Fig. 18a: *Unsmoothed and smoothed empirical density profiles for SN 1987A.*

Fig. 18b: *The empirical density profile for SN 1987A and a smoothed version of Woosley's model 10H density profile.*

Fig. 19: *SN 1987A photospheric outflow mass and photospheric outflow kinetic energy (i.e., mass and kinetic energy that have flowed out through the photosphere) plotted as functions of time since the explosion. These quantities were derived using simplifying assumptions and a fit of the day* 257.65 *photospheric outflow mass to the mass of model 10H.*

Fig. 20: *Photometric velocity and model 10H velocity plotted versus mass coordinate where mass is measured inward from the surface. The mass coordinate for the photometric velocity curve is just the derived photospheric outflow mass.*

Fig. 21: *The empirical and smoothed model 10H density profiles plotted as functions of mass coordinate where mass is measured inward from the surface. The mass coordinate for the empirical density profile curve is just the derived photospheric outflow mass.*

Figs. 22a–22c: *Solar-composition TE-predicted photospheric Sobolev optical depths for SN 1987A.*

Fig. 23: *Solar-composition TE-predicted and spectrum-fitted photospheric Sobolev optical depths, and upper limits on the Sobolev photospheric optical depths of the Li I 6708 line.*

Fig. 24: *Observed spectrum from CTIO and synthetic spectrum both for SN 1987A on 25.17 Feb. 1987 U.T.*

Fig. 25: *Observed and synthetic spectra for 27.03 Feb. 1987 U.T.*

Fig. 26: *Observed and synthetic spectra for 1.07 Mar. 1987 U.T.*
Fig. 27: *Observed and synthetic spectra for 4.02 Mar. 1987 U.T.*
Fig. 28: *Observed and synthetic spectra for 9.00 Mar. 1987 U.T.*
Fig. 29: *Observed and synthetic spectra for 15.03 Mar. 1987 U.T.*
Fig. 30: *Observed and synthetic spectra for 26.02 Mar. 1987 U.T.*
Fig. 31: *Observed and synthetic spectra for 3.99 Apr. 1987 U.T.*
Fig. 32: *Observed and synthetic spectra for 23.97 Apr. 1987 U.T.*
Fig. 33: *Observed and synthetic spectra for 13.97 May 1987 U.T.*
Fig. 34a: *Observed and synthetic spectra for 4.95 Jun. 1987 U.T.*
Fig. 34b: *Logarithmic plot of observed and synthetic spectra for 4.95 Jun. 1987 U.T.*
Fig. 35: *Observed and synthetic spectra for 18.95 Jun. 1987 U.T.*
Fig. 36: *Observed and synthetic spectra for 4.39 Jul. 1987 U.T.*